IMPROVEMENT OF A MULTISCALE FRAMEWORK FOR THE ANALYSIS OF COMPOSITE MATERIALS

A Thesis

by

MICHAEL KEITH BALLARD II

Submitted to the Office of Graduate and Professional Studies of
Texas A&M University
in partial fulfillment of the requirements for the degree of

MASTER OF SCIENCE

Chair of Committee,	John D. Whitcomb
Committee Members,	J. N. Reddy
	Amine Benzerga
Head of Department,	Rodney D. W. Bowersox

August 2014

Major Subject: Aerospace Engineering

ABSTRACT

Multiscale analyses have been extensively used to virtually test how a material will respond linearly and nonlinearly, due to the initiation and evolution of damage, to a variety of loads and environmental conditions. This work improved several components of a multiscale framework. At the microscale, elastic properties were determined for four types of graphite fibers, including AS4, IM7, T300, and T650, along with a type of glass fiber, E-glass 21xK43, using an inverse method. Homogenization methods used in the inverse analyses include: finite element analysis (FEA) with a hexagonal microstructure, FEA with a random microstructure, and Mori-Tanaka averaging scheme. Fiber properties determined using FEA with a hexagonal microstructure and the Mori-Tanaka averaging scheme were very similar, while using FEA with a random arrangement of fibers resulted in significantly different properties. The predicted longitudinal shear modulus, G_{12}, of the graphite fiber was observed to almost linearly depend on the minimum spacing between fibers, while the other engineering constants did not depend on the minimum space between fibers. The predicted properties for the glass fiber were shown to be insensitive to the homogenization method used. At the mesoscale, two types of continuum damage models, a cohesive zone model, and a combination of the two types were compared using a $[0/90]_s$ laminate under uniaxial tension and in-plane shear loads. The volume average stress-strain response, the crack density evolution, and a metric developed using two-point correlation functions were used to quantify the similarities and differences of the progressive damage models. For a laminate under uniaxial tension,

a continuum damage model that degrades the material on an element basis predicted a progression of damage similar to the cohesive zone model. A continuum damage model that degrades the material on a quadrature point basis predicted a lower applied strain for final failure and a higher crack density. Under in-plane shear, the continuum damage models predicted damage growth across fibers, which is unrealistic. Cohesive zone elements can be placed where damage is expected, but when placed in all directions, the cohesive zone model predicted the same unrealistic damage growth across fibers.

This thesis is dedicated to my family, who have always encouraged me to pursue what I am passionate about.

ACKNOWLEDGEMENTS

First, I thank God for the opportunity to study a very small part of His creation at such a great university.

I am deeply thankful for the inspiration and help from others, which has made this work possible. Dr. Whitcomb has been an integral part of this work, offering many tools developed by himself and other graduate students before me. He has guided the research topics when I didn't know what to pursue, given me inspiration when I encountered the difficult challenges, and imparted a great deal of knowledge through my undergraduate and graduate work. This work would not have been possible without him. In addition, my committee members, Dr. Benzerga and Dr. Reddy, have taught me in and out of the classroom. Their suggestions and guidance for this thesis has been invaluable. Apart from my committee, several graduate students have helped trendously in my work. Many of the topics explored within this thesis is either inspired or greatly influenced by the work of Dr. Ross McLendon, who tolerated my incessant questions my first year as a graduate student and gave me crucial advice. Other graduate students I have relied upon for help in this work include Dr. Kevin Maxwell, Brian Lester, Hieu Truong, Tunde Agboola, and Austin Cox. I am very grateful for the funding I have received from the Heep Fellowship and the Multidisciplinary University Research Initiative grant FA9550-09-1-0686 from the Air Force Office of Scientific Research to Texas A&M University with Dr. David Stargel as the program manager.

I am also very grateful to my family. They have encouraged and supported me

during the stress and difficulties that come at times during graduate school.

TABLE OF CONTENTS

CHAPTER Page

LIST OF FIGURES

FIGURE Page

FIGURE Page

LIST OF TABLES

CHAPTER I

INTRODUCTION

Over the past few decades, engineering disciplines have found a growing number of uses for composite materials, a material composed of several different materials called constituents. To effectively use composites, engineers must have tools to predict the material's relevant responses under the expected load. Depending on the application of the composite, various types of responses may be considered relevant, including mechanical, thermal, optical, and magnetic to list some.

The three categories of methods commonly used to predict a material's response include experiments, analytical methods, and numerical methods. With experiments, the material can simply be tested under the expected conditions and load, offering the most accurate characterization. However, experimentally characterizing a composite material system under a multitude of conditions is prohibitive due to the time and monetary cost required to perform the experiments. Analytical methods use material parameters obtained from experiments and constitutive relations to describe the material's behavior, but analytical approaches are not adequate for problems with high complexity. Numerical methods use material parameters obtained from experiments and analytical equations describing the behavior of a small piece of material to develop a system of equations, whose solution describes the response at a finite number of points within the material. Since the domain is discretized into smaller domains, solutions can be obtained for problems with complex geometries and loads. A few of the numerous numerical methods used in engineering are the finite element method

(FEM) and finite difference method. The finite element method in particular has been frequently applied to structural analyses and is the primary focus of this work. Finite element analyses allow the virtual testing of a composite under a variety of loads and conditions at a much lower monetary and time cost than a suite of experiments. There is always error associated with using numerical methods over direct experimentation, but with the careful choice of element formulations, meshing, and numerical tolerance, finite element analyses can predict a solution with acceptable accuracy.

When characterizing a complex material's behavior using finite element analyses, every scale cannot feasibly be discretely accounted for at once due to prohibitive mesh sizes and computational costs, so a multiscale approach is employed. In a multiscale analysis, a scale of the material is characterized and the information is used in an analysis involving a higher scale of the material. The scales typically considered for fiber reinforced composites include the microscale, the scale at which the fibers and matrix are accounted for discretely, mesoscale, an intermediate scale where laminae or tows are discretely modeled using information from the microscale, and the macroscale, where an engineering part is modeled. An example of these scales are shown in Figure I. The material considered within each scale can have varying constitutive relations and failure modes, causing the modeling of each scale to have its own challenges.

An analysis involving the microscale requires parameters that can be used to describe the behavior of the constituents. In fiber reinforced composites, the fibers are typically assumed to be transversely isotropic, and experiments can be used to

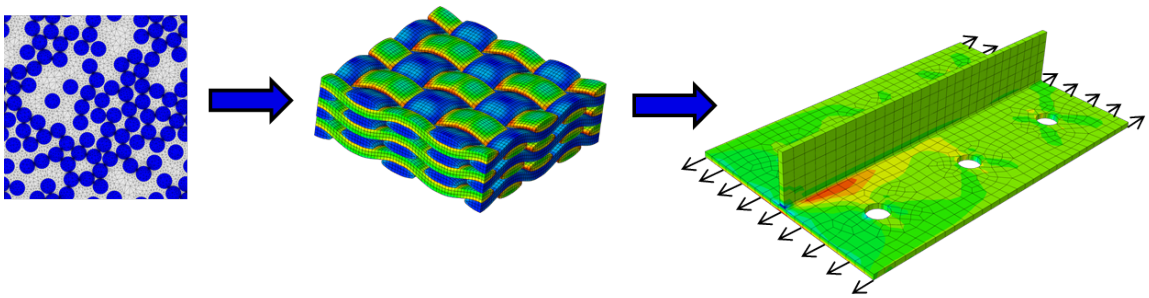

Figure I.1. Scales considered within a multiscale analysis of a fiber reinforced composite (microscale, mesoscale, and macroscale respectively)

obtain some of the material parameters, such as the longitudinal Young's modulus, but due to the small transverse dimensions of the fibers, other methods must be used to determine the remaining parameters. An inverse analysis uses the response of a higher scale measured by experiments to determine the parameters of the constituents by assuming some microstructure typography and homogenization method, varying the constituent properties until the predicted homogenized properties match those measured in experiments. Historically, homogenization methods based on micromechanics, relying on the Eshelby solution, or FEA, typically assuming a hexagonal arrangement of fibers within the matrix, has typically been used within an inverse analysis to determine the properties of the fibers. [1–4] Homogenization methods based on micromechanics generally lack a description of the microstructure and account for the interaction of fibers in close proximity by modifying the properties of the medium the fibers are assumed to lie within. However, in reality the microstructures of fiber reinforced composites can be quite random having fibers in extremely close proximity and others that are far apart from all other fibers, as shown in Figure I.2. This randomness within the microstructure has been

considered in previous microscale analyses [5–9], but has not been considered when executing an inverse analysis to determine apparent properties for graphite fibers. When accounting for randomness within the microstructure, the computational cost greatly increases compared to an analysis assuming a uniform microstructure, and an inverse analysis can require the solution of thousands of these problems, requiring a large amount of computational resources. The introduction of randomness leads to more realistic microstructure typographies and may affect the predicted material parameters.

Various mechanisms, such as mechanical load, thermal load, oxidation, or moisture, can cause damage within the material, which can dramatically affect the material's response. Therefore, engineers attempt to predict when damage will initiate and the material response as damage evolves, known as progressive damage analyses, allowing the prediction of how failure within a part will affect the whole structure as conditions change. In the context of this work, damage due to mechanical load will be considered and modeled using FEA. Many researchers have proposed various criteria to predict the initiation of damage for a piece of material and various ways of degrading the material once failure has initiated. These methods will be referred to as continuum damage approaches within this work. Continuum damage approaches using FEA have the benefit of no added degrees of freedom and simple implementation, when the failure criteria is calculated locally. However, most continuum damage approaches lack directionality of damage evolution resulting in some unexpected behavior. An example of this behavior was observed in the context of textile composites with damage growth across tows under shear load, as shown in

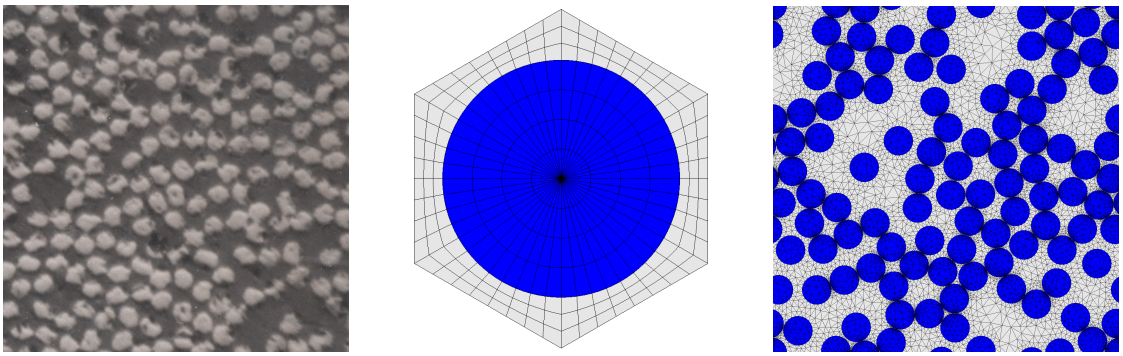

(a) Micrograph of an actual microstructure (b) Hexagonal RVE mesh (c) Random RVE mesh

Figure I.2. Comparison of microstructures

Figure I.3. [10]

Another approach that has gained popularity in recent years is known as the cohesive zone model. A cohesive zone element refers to an element designed to lie between faces of adjoining elements and open up according to a traction separation law. Several cohesive zone formulations have been proposed by Turon et al., who assumed a bilinear law to govern the separation, [11] Needleman, who assumed an exponential potential to govern the separation, [12] and Park et al., who suggested a polynomial potential to govern the separation, [13] to list some of the many formulations proposed by researchers. However, the cohesive zone approach has been known to have issues as well, such as numerical stability. [14] With the numerous approaches to model damage available, the choice of which ones to utilize in an analysis can be difficult. Unfortunately, these models are rarely compared to each other in an attempt to understand the strengths and weaknesses of each. This work will not consider every approach proposed as there are far too many to include in a single thesis, but it will compare several continuum damage approaches, a cohesive

zone model, and a combination of the two approaches in the context of laminated composites under several in-plane load configurations.

Since this work seeks to improve several aspects a multiscale framework, the objectives can easily be separated into two sections by the analysis scale they consider and are as follows:

- Objectives at the microscale
  - Determine appropriate guidelines for combinations of RVE sizes and numbers of realizations for inverse analyses of unidirectional laminae.
  - Study the affects of randomness in the microstructure on apparent fiber properties in an inverse analysis.
- Objectives at the mesoscale
  - Develop robust methods of comparison for comparing the damage states of laminated composites.
  - Compare a small set of continuum damage, cohesive zone, and hybrid models in the context of laminated composites, and offer insight into the advantages and disadvantages of each.
  - Discuss issues and possible solutions in the numerical implementation of the damage models.

[1]Figure generated by Ross McLendon

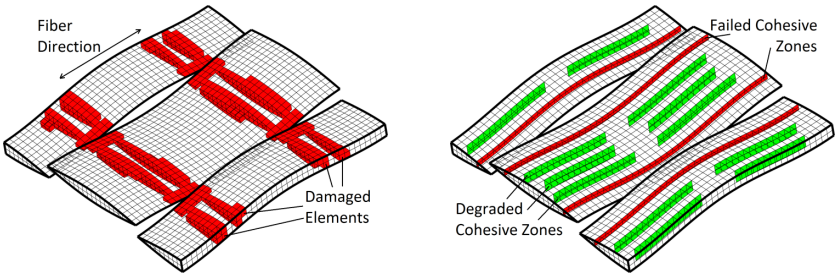

(a) Continuum damage approach[1] (b) Cohesive zone model [10]

Figure I.3. Damaged elements due to pure shear load during a progressive damage analysis

This thesis provides a review of relevant literature pertaining to the different aspects of the multiscale framework considered. It begins with a review of the salient work in micromechanics leading to the development of the homogenization methods considered, followed by a summary of the work in the area of determining the properties of graphite fibers through an inverse problem. Next, a review of continuum damage, with a focus on the application to laminate composites, and cohesive zone models. Following the literature review, a theory section describes the derivation of the FEM for both linear and nonlinear (progressive damage) problems, the algorithm employed to inversely determine constituent properties, the formulation of the continuum damage approaches considered in this work, and the formulation of the considered cohesive zone models. The results of this work are then presented for the two areas of interest. First, the affect of the RVE size and number of realizations used in the inverse analysis on the resulting properties is presented, followed by several resulting properties using different fiber reinforced composite material systems. Second, a comparison of progressive damage models applied to laminated composites is given, including results using continuum damage approaches, cohesive zone models,

and combinations of the two. An investigation of the numerical behavior of cohesive zones is also included in this section, as numerical stability seems to be one of the primary draw backs of the approach and has been of interest to the field for about a decade now. Finally, this paper will end with a summary of the results, insights into the successes attained in this work, and a list of any areas that should require further research.

Within a multiscale framework that predicts the response of fiber reinforced composites, many tools and methods are required. This work contributes to established methods by offering a method for determining more accurate properties for graphite fibers through an inverse problem, comparing some progressive damage models applied to laminated composites, and discussing difficulties faced in the numerical implementation of the damage models. Each of these contributions goes to enhance the multiscale framework used for fiber-reinforced composites across several scales.

CHAPTER II

LITERATURE SURVEY

With the enormity of a multiscale framework used in composites, there has been contributions from many authors. This chapter offers a review of previous literature pertaining to the determination of graphite fiber properties and progressive damage models relevant to laminate composites. First, a cursory description of the history of micromechanics is given, followed by a review of the homogenization methods applied to the determination of graphite fiber properties. Continuum damage models are then discussed with an emphasis on methods applied to laminated composites. Finally, the work in cohesive zone models are reviewed, including numerical issues faced.

II.A. Micromechanics

Since composites involve multiple constituent phases, information across multiple scales becomes important when analyzing a composite material. Which scales are important depends on the material and application, but generally a microscale, mesoscale, and macroscale are of interest. Homogenization of scales allows much less information to be passed to an analysis involving higher scales through the use of effective properties, where one scale of the material can represented by a set of effective properties and give the same response as the discrete properties in some average sense.

The first prediction of effective properties of a heterogeneous material dates

back to the 19th century by Voigt with the rule of mixtures. [15] In linear elasticity, this model is equivalent to assuming iso-strain throughout the composite material. Voigt's model provides an upper bound for effective properties. Early in the 20th century, Ruess proposed the inverse rule of mixtures, which provides a lower bound for effective properties. [16] In linear elasticity, this is equivalent to assuming iso-stress throughout the composite.

The Hashin-Shrikman bounds were developed using variational methods and offered a tighter bounds on the effective elastic moduli of transversely isotropic composites. [17] The methodology was also used to develop the bounds for many other effective properties, such as the conductivity of polycrystals. [18] Several other methods were proposed based on elasticity, such as the composite cylinder [19] and vanishing fiber diameter methods [20].

A series of large developments stemmed from what came to be known as Eshelby's solution. For the problem of an isotropic ellipsoidal inclusion that undergoes some strain inducing transformation placed in an infinite homogeneous isotropic medium, Eshelby proposed the closed form solution for the strain field both inside the inclusion and in the infinite medium using what is now known as the Eshelby tensor. [21, 22] The Eshleby tensor was generalized for a transversely isotropic inclusion by Mura [23] and later extended further for an anisotropic inclusion by Gavazzi and Lagoudas through the use of numerical evaluation [24].

Many different mean-field homogenization techniques proposed in the following years relied upon this solution. Mori-Tanaka proposed the evaluation of effective properties by assuming ellipsoidal inclusions placed within an infinite matrix mate-

rial and accounted for the approximate interaction of inclusions through averaging in the strain field. [25] The self-consistent method was proposed by Hill and assumed ellipsoidal inclusions placed within an infinite medium, which has the effective properties of the composite. [26] Several other methods were proposed based on Eshelby's solution, such as the differential method. [27, 28]

The concept of representing the composite as a collection of repeating unit cells was leveraged by the work of Aboudi, which led to the generalized method of cells. The method divided the unit cell into an arbitrary number of sub-cells, each representing a constituent material of the composite. A 1^{st} order displacement field is assumed within the sub-cells. [29] The concept of a unit cell naturally led to the numerical computation of effective properties of a representative volume element (RVE).

Incorporating more information about the local geometry of the RVE's into the prediction of effective properties for random media has been of interest and considered by many researchers today, such as Torquato, Milton, Quintanilla, and Sigmund, to name only a few. Torquato offers a very extensive review of this field in Ref. [30].

Mean-field homogenization methods were extended for non-linear materials. Secant methods have been proposed by Berveiller and Zaoui [31], Tandon and Weng [32], and Suquet [33]. Hashin-Skrikam bounds were extended for nonlinear material by Castaneda. [34] Castaneda extended homogenization theory for nonlinear materials through linear comparison methods, which proposes that the effective response of a nonlinear composite can be expressed in terms of a linear comparison compos-

ite following from variational principals and has been incrementally improving the second-order estimates. [35–38] Homogenization techniques based on continuum micromechanics have formed a mature field within micromechanics, but recent work has aimed at understanding the limits of these methods for increasingly complex composites. [39, 40] More recently, researchers have resorted to numerically computing the approximate solution of the equivalent inclusion problem in order to solve for the mean-field response of nonlinear composites. [41]

Some of the homogenization techniques discussed in this section have been applied to the inverse problem of solving for constituent properties.

II.B. Determination of Graphite Fiber Properties

ASTM standard D 4018-11 delineates the methodology how to measure graphite fiber properties, such as density and extensional Young's modulus, but does not include the measurement of transverse or shear properties of the fiber. The difficulty in measuring these properties experimentally is due to the very small transverse dimension of the fibers, so inverse analyses have typically been used to predict the properties of the fiber given the response of a larger composite. This methodology has been used to determine graphite fiber properties as early as 1979 by Kriz and Stinchomb using mean-field theories. [42] King et al. predicted the shear strength of the graphite fibers through an inverse approach. [1] Pagano predicted the transversely isotropic elastic and thermal properties of graphite fibers through the solution of a linear elastic boundary value problem. [3, 4] Rupnowski more recently evaluated the elastic and thermal properties of graphite fibers using the Mori-Tanaka averag-

ing scheme. [2] Unfortunately, the higher order homogenization methods have not been used in the inverse problem to determine the apparent properties for graphite fibers, and this topic has had little work that attempted to consider the location and interaction of graphite fibers in the inverse problem.

II.C. Continuum Damage

The concept of a damage parameter was first proposed by Murzewski. [43] Soon afterwards, Kachanov had the first paper devoted to a continuous damage variable and suggested a theory for creep in metals under uniaxial loads. [44, 45] Rabotnov followed with another theory for creep in metals under uniaxial loads. [46, 47]

A damage theory relies on the definition of a damage parameter, which often cannot be directly measured. Many researchers have proposed various measures of damage, such as remaining life or changes in physical properties. [48] Due to the extensive volume of literature on the subject, a review of the history of continuum damage will be excluded here but can be found in Chaboche [48], Ambroziak and Klosowski [49], Fatemi and Yang [50], and Zaoui [51].

In the field of laminated composites, Varna et al. applied continuum damage mechanics to a laminated composite. [52] Damage across multiple scales was considered by Allen, who applied the theories to laminated composites. [53] Methods have been proposed to accounted for various damage mechanisms in laminated composites, such as sub-laminate damage growth by the work of Williams et al. [54], delamination by the work of Zou et al. [55], matrix cracking by the work of Nguyen and Khaleel [56], and interfacial debonding by the work of Rangavan and Ghosh [57]. A model for

damage due to a distribution of transverse matrix cracks within linear viscoelastic composites was proposed by Kumar and Talreja, which used second-order tensors to describe the damage within the material instead of a single damage parameter. [58]

In the early 21st century, a worldwide attempt to evaluate the current failure theories for laminated composites began, known as the World-Wide Failure Exercise (WWFE). The exercise stemmed from two issues in the field: a lack of validation for currently used theories and a lack of a universal definition for failure in a laminated composite. [59] A comparison of different failure theories was by no means new, and had been attempted by Greenwood [60], Owen and Rice [61], and Swanson and Christoforou [62].

Participants of the WWFE were chosen to represent many of the popular failure theories used at the time and given high quality experimental data for validation cases. Hashin was invited to participate in the exercise but gave the response:

> "My only work in this subject relates to failure criteria of unidirectional fibre composites, not to laminates. I do not believe that even the most complete information about failure of single plies is sufficient to predict the failure of a laminate, consisting of such plies. A laminate is a structure which undergoes a complex damage process (mostly of cracking) until it finally fails. The analysis of such a process is a prequisite for failure analysis. While significant advances have been made in this direction we have not yet arrived at the practical goal of failure prediction. I must say to you that I personally do not know how to predict the failure of a laminate (and furthermore, that I do not believe that anybody else

does)." [59]

His response goes to underline the skepticism of current failure theories applied to laminated composites.

Many theories were represented, including: a maximum strain criterion, Tsai-Wu criterion, a maximum stress criterion, and a generalized Tresca model to name some. [59] Theories that performed well for the variety of test cases include: Zinoviev's modified maximum stress criterion to account for changes in fiber orientation, Bogetti's maximum strain criterion with the addition of nonlinear shear behavior, the Tsai-Wu criterion, and Puck's and Cuntze's models, which are more involved than most of the others. [63–66] The WWFE resulted in very helpful observations concerning many of the current failure theories discovering many strengths and weaknesses of each.

Only a few years later, a second WWFE was initiated to investigate the performance of the failure theories for a wider range of laminated composites, triaxial load conditions, and through thickness behavior.

Where the first two WWFE's have looked at primarily the final failure of laminated composites under many load configurations, the third WWFE, which very recently started, seeks to give insight into the predictions of the theories during the initiation and progression of damage.

Though the first two of the WWFE were successful (the third is ongoing), it has become apparent that close correlation to experimental data by all the damage models available is very difficult. The criteria for a successful theory is currently a correlation within $\pm 50\%$ of the experimental data for at least 75% of the test

cases. [67]

For the maturity of continuum damage mechanics, the progression of damage within laminated composites is still a very important topic to research with many questions to be answered.

II.D. Cohesive Zone Models

Cohesive zone models rely on the concept of interfacial elements, which are governed by a traction-separation curve. The thought of using attractive forces per unit area between two elements was first conceived by Elliot in the study of Griffth cracks, adding a model for the nonlinear damage of the material. [68] It wasn't until Barenblatt that a cohesive zone model was proposed. Barenblatt used a traction-separation law to model fracture in brittle materials. [69,70] The use of cohesive zone models continued as researchers attempted to model cracks, including the work of Dugdale, Willis, Cribb, Hillerborg, etc.. [71–75]

As cohesive zone models were developed, two categories of cohesive zone formulations appeared: intrinsic and extrinsic. Intrinsic cohesive zones have a linear regime in the traction-separation law, during which the cohesive zone acts as a linear elastic interface, and once a critical traction is reached, the cohesive zone begins to undergo irreversible softening. Intrinsic cohesive zones are placed within the mesh before the analysis and easier to implement than the other type, but they introduce some artificial compliance in the structure. Extrinsic cohesive zones are inserted dynamically into the mesh once a critical traction is reached, requiring more effort in implementation, but does not introduce any artificial softening of the structure

before the cohesive zones reach the critical traction. Furthermore, intrinsic cohesive zones can create convergence issues under some conditions, such as a large group of cohesive zones experiencing opening at once. [76]

Cohesive zone models have been applied to a multitude of problems ranging from polymer crazing [77] to failure in functionally graded materials [78]. Park and Paulino offer a thorough review of the applications and developments of cohesive zones in Ref. [79]. More recently, cohesive zones have been applied to multi-scale problems to model plasticity and damage. [80–83]

Many traction-separation laws have been proposed, some based on a potential function and others not. A few of the prominent potential based traction-separations laws include Xu and Needleman's proposed exponential function [84] and Park, Paulino, and Roesler's polynomial functions [13]. Other potential based laws have been proposed by Needleman, Beltz and Rice, and Freed and Banks-Sills. [12, 85–87] One of the more prominent traction-separation laws not based on a potential was proposed by Turon, who originally aimed at modeling delamination with cohesive zones in a thermodynamically consistent manner. [11] Some of the benefits of this model is the simplicity, minimal need for material parameters compared to other formulations, and ease of implementation into a finite element framework.

Two primary challenges have surfaced in the implementation of cohesive zone models. First the oscillatory tractions along interfaces have been observed by many researchers. Schellekens and de Borst observed that oscillatory tractions occurred when using Gauss integration for interfacial elements experiencing high gradients of stress. [88] They also showed that in some situations, this problem can be circum-

vented by the use of Newton-Cotes integration. However, the Newton-Cotes scheme requires a larger number of quadrature points than the Gauss scheme to exactly integrate the same polynomial function. Another solution is to refine the mesh as to remove the high stress gradients. [89, 90] Turon proposed lowering the critical traction for the interfacial elements as yet another solution to the spurious traction behavior. [90] However, this solution does introduce errors into the predicted response.

The second important difficulty in the implementation of cohesive zone elements is the convergence behavior. Roy and Dodds showed that the convergence instabilities can be introduced through the use of Newton-Cotes integration schemes, while Gauss integration schemes resulted in superior convergence behavior. Unfortunately, the solution to the traction oscillation problem is in direct competition to the solution of the numerical convergence in this aspect. [91] Han et al. used the Lobatto numerical integration scheme to avoid convergence issues, but the effects of the scheme on the traction oscillation problem has not been studied. [92] Alternatively, several researches have employed an arc-length method to circumvent convergence issues, but even this method faced convergence issues in some situations. [93–95] Further investigation into the effects of mesh refinement and choice of nonlinear solver on numerical convergence issues is presented by Paulino in Ref. [96].

From the relevant literature, it becomes clear that there is no universal solution for the numerical difficulties faced in the implementation of cohesive zone models, but given their utility, further investigations and consideration is warranted to improved current methodologies.

CHAPTER III

THEORY*

In this chapter, the relevant theory for the multiscale analysis is presented. The development of finite elements for infinitesimal strain is developed. Next, the microstructure models, algorithm, and composite systems considered in the inverse problem of determining fiber properties. Finally, the theory for the damage models used within this work is given. This includes describing the relevant continuum damage and cohesive zone models, numerical methods for solving nonlinear damage problems, and the methods used for comparing damage models.

Within this paper, repeated indices will imply the summation from 1 to 3. This convention is also known as indicial notation.

*Parts of this material, originally appeared in the ASC Proceedings, Volume 2013 (2014), published by DEStech Publications, Inc., Lancaster, PA, USA, and is reprinted here with permission of the publisher.

III.A. Finite Element Method

This section describes the finite element formulation used within this work. First, the basic kinematics are derived resulting in the infinitesimal strain tensor, followed by the development of the the Cauchy stress tensor. The conservation of mass, linear momentum, and angular momentum are derived resulting in the equilibrium equation and symmetry of the Cauchy stress tensor. Some of the various material symmetries are developed, using Hooke's law. With the constitutive relation and equilibrium equation, the weak form and finite element model is derived. Finally, the numerical integration techniques are discussed, including two methods of quadrature.

III.A.1. Kinematics

III.A.1.a. Eulerian and Lagrangian Descriptions

Mathematically, the deformation can be described in terms of the Eulerian description, which is in terms of the deformed configuration and is known as the spatial description, or the Lagrangian, which is in terms of the undeformed configuration and is known as the material description. Both configurations are shown in Figure III.1. In the reference configuration where no deformation has occurred, a point in the material is denoted by X_i. In the deformed configuration, the same point is denoted by x_i, such that a function exists relating two configuration as shown in Equation (3.1).

$$x_i = \chi(X_i, t) \tag{3.1}$$

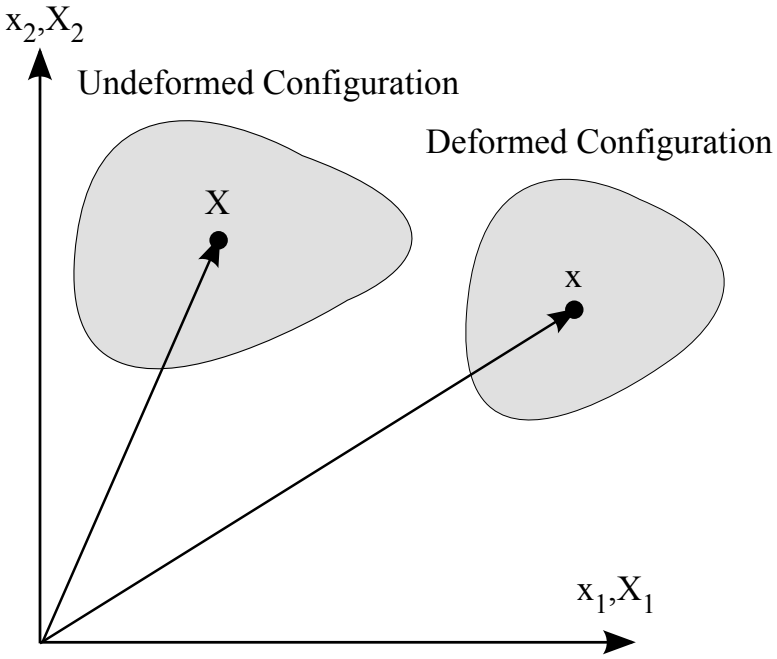

Figure III.1. Illustration of configurations

III.A.1.b. Displacements

The displacement is defined as the change in position from the reference configuration to the deformed configuration. It can be written in terms of the Lagrangian description by Equation (3.2).

$$u_i(X,t) = x_i(X,t) - X_i \tag{3.2}$$

III.A.1.c. Infinitesimal Strain

A useful quantity in this formulation is the deformation gradient, F, defined in Equation (3.3), where δ_{ij} is the Kronecker delta.

$$F_{ij} = \frac{\partial x_i}{\partial X_j} = \frac{\partial u_i}{\partial X_j} + \delta_{ij} \tag{3.3}$$

The tensor known as the right Cauchy-Green deformation tensor, C, is then

defined by Equation (3.4).

$$C_{ij} = F_{ki}F_{kj} \tag{3.4}$$

The Green-Lagrange strain tensor is then defined by Equation (3.5) and can be rewritten as Equation (3.6).

$$E_{ij} = \frac{1}{2}(C_{ij} - \delta_{ij}) \tag{3.5}$$

$$E_{ij} = \frac{1}{2}(\frac{\partial u_i}{\partial X_j} + \frac{\partial u_j}{\partial X_i} + \frac{\partial u_k}{\partial X_i}\frac{\partial u_k}{\partial X_j}) \tag{3.6}$$

Assuming the second order term, $\frac{\partial u_k}{\partial X_i}\frac{\partial u_k}{\partial X_j}$, is negligible and $\frac{\partial u_i}{\partial X_j} \approx \frac{\partial u_i}{\partial x_j}$ leads to the linearized infinitesimal strain tensor, $\boldsymbol{\varepsilon}$, is given by Equation (3.7).

$$\varepsilon_{ij} = \frac{1}{2}(\frac{\partial u_i}{\partial X_j} + \frac{\partial u_j}{\partial X_i}) \tag{3.7}$$

With the assumptions necessary for the linearized infinitesimal strain tensor, the Eulerian and Lagrangian descriptions become equivalent.

III.A.2. Cauchy Stress

Traction, also known as the stress vector, is defined by the force, f, divided by area, A, for an infinitesimal area of material, as shown in Equation (3.8).

$$t_i = \frac{f_i}{A} \tag{3.8}$$

Cauchy's law relates the traction to a quantity known as the Cauchy stress tensor, $\boldsymbol{\sigma}$, as shown in Equation (3.9), where n is the unit normal vector that defines the traction vector. The Cauchy stress tensor is defined in the deformed configuration, the force in the deformed configuration divided by the deformed area at a point, but in the case of infinitesimal strain, the need to distinguish between the deformed

and undeformed configuration is alleviated. This work only considers infinitesimal strains, so the Cauchy stress tensor is equivalent to other stress measures and will be referred to as simply the stress tensor.

$$t_i = \sigma_{ij} n_j \tag{3.9}$$

III.A.3. Conservation Equations

The general form for the conservation of mass is expressed in Equation (3.10). Since the principle must hold for an arbitrary volume element the integrand must equal zero, and since this work assumes the density of the material is constant with time, the conservation of mass results in the expression Equation (3.11).

$$\frac{d}{dt} \int \rho(\boldsymbol{x}) dV = 0 \tag{3.10}$$

$$\frac{\partial \rho v_i}{\partial x_i} = 0 \tag{3.11}$$

The balance of linear momentum assuming tractions, t, and body forces, b, acting on the material is shown in Equation (3.12). Using Cauchy's law, shown in Equation (3.9), and the divergence theorem, the equation can be expressed as shown in Equation (3.13). Finally, since the equation must hold for any arbitrary volume and leveraging the Reynold's transport theorem, the balance of linear momentum can be written in the useful form shown in Equation (3.14).

$$\int t_i dA + \int \rho b_i dV = \frac{d}{dt} \int \rho v_i dV \tag{3.12}$$

$$\int \frac{\partial \sigma_{ji}}{\partial x_j} + \rho b_i dV = \frac{d}{dt} \int \rho v_i dV \tag{3.13}$$

$$\frac{\partial \sigma_{ji}}{\partial x_j} + \rho b_i = \rho a_i \tag{3.14}$$

The balance of angular momentum, assuming applied tractions and body forces acting on the volume element, is shown in Equation (3.15).

$$\int \boldsymbol{x} \times \boldsymbol{t} dS + \int \boldsymbol{x} \times \rho \boldsymbol{b} dV = \frac{d}{dt} \int \boldsymbol{x} \times \rho \boldsymbol{v} dV \tag{3.15}$$

The equation can be written in indicial notation as Equation (3.16), and using Cauchy's law, the product rule, and the Reynold's transport theorem, the equation becomes Equation (3.17).

$$\int \epsilon_{ijk} x_j t_k dS + \int \rho \epsilon_{ijk} x_j b_k dV = \frac{d}{dt} \int \rho \epsilon_{ijk} x_j v_k dV \tag{3.16}$$

$$\int \epsilon_{ijk} \left(\delta_{jm} \sigma_{mk} + x_j \frac{\partial \sigma_{mk}}{\partial x_m} \right) + \rho \epsilon_{ijk} x_j b_k dV = \int \rho \epsilon_{ijk} x_j a_k dV \tag{3.17}$$

Rearranging the equation as shown in Equation (3.18), it becomes clear that the right hand side is zero by the balance of linear of momentum, see Equation (3.14).

$$\int \epsilon_{ijk} \delta_{jm} \sigma_{mk} dV = \int \epsilon_{ijk} x_j \left(\rho a_k - \frac{\partial \sigma_{mk}}{\partial x_m} - \rho b_k \right) dV \tag{3.18}$$

Manipulating the resulting equation shown in Equation (3.19) and using the same argument of localization used in the balance of linear momentum, the balance of angular momentum results in the local form shown in Equation (3.20), which states that the Cauchy stress tensor is symmetric.

$$\int \epsilon_{ijk} \delta_{jm} \sigma_{mk} dV = \int \epsilon_{ijk} \sigma_{jk} dV = 0 \tag{3.19}$$

$$\sigma_{jk} - \sigma_{kj} = 0 \tag{3.20}$$

III.A.4. Constitutive Relations

Hooke proposed that in a continuous media stress is linearly related to strain. The relationship can be described by a 4th order tensor, C_{ijkl}, known as the stiffness

matrix, as shown in Equation (3.21). The relationship can be inverted, and the matrix relating strain to stress, S_{ijkl}, is known as the compliance matrix, leading to Equation (3.21).

$$\sigma_{ij} = C_{ijkl}\varepsilon_{kl} \tag{3.21}$$

$$\varepsilon_{ij} = S_{ijkl}\sigma_{kl} \tag{3.22}$$

Since the stress and strain tensors are symmetric, many of the terms in the constitutive matrix can be reduced by $C_{jikl} = C_{ijkl}$ and $C_{ijlk} = C_{ijkl}$, respectively, resulting in a reduction from 81 unique constants to only 36 unique constants. Finally, the stress can be expressed as a partial derivative of the strain energy density, U, with respect to the strain, as shown in Equation (3.23). This leads to a symmetry of the stiffness matrix as shown in Equation (3.24), further reducing the number of unique constants from 36 to 21.

$$\sigma_{ij} = \frac{\partial U}{\partial \varepsilon_{ij}} \tag{3.23}$$

$$C_{ijkl} = \frac{\partial^2 U}{\partial \varepsilon_{ij} \partial \varepsilon_{kl}} = C_{klij} \tag{3.24}$$

Because of the symmetries, Hooke's law can be written in a contracted notation, as shown in Equation (3.25), where the strains are engineering strain for which the shear strains are twice the tensorial values. In indicial notation, the equation simply becomes $\sigma_i = C_{ij}\varepsilon_j$. Note that the stiffness matrix is still symmetric even in the

contracted notation, $C_{ij} = C_{ji}$.

$$\begin{bmatrix} \sigma_1 \\ \sigma_2 \\ \sigma_3 \\ \sigma_4 \\ \sigma_5 \\ \sigma_6 \end{bmatrix} = \begin{bmatrix} C_{11} & C_{12} & C_{13} & C_{14} & C_{15} & C_{16} \\ C_{12} & C_{22} & C_{23} & C_{24} & c_{25} & C_{26} \\ C_{13} & C_{23} & C_{33} & C_{34} & C_{35} & C_{36} \\ C_{14} & C_{24} & C_{34} & C_{44} & C_{45} & C_{46} \\ C_{15} & C_{25} & C_{35} & C_{45} & C_{55} & C_{56} \\ C_{16} & C_{26} & C_{36} & C_{46} & C_{56} & C_{66} \end{bmatrix} \cdot \begin{bmatrix} \varepsilon_1 \\ \varepsilon_2 \\ \varepsilon_3 \\ \varepsilon_4 \\ \varepsilon_5 \\ \varepsilon_6 \end{bmatrix} \tag{3.25}$$

The compliance matrix for material with at least two planes of symmetry can conveniently be expressed in terms of engineering constants: Young's moduli, which relates the extensional deformation to the normal stress and denoted by E, shear moduli, which relates the shear deformation to the shear stresses and is denoted by G, and Poisson's ratios, which relates the transverse deformation and to the normal deformation and is denoted by ν. For anisotropic media, the subscripts for E, G, and ν indicate the direction and plane in which the respective property is measured. The order of stresses and strains in the contracted notation is arbitrary so long as the notation is consistent. The finite element code used for this work uses the order of (11, 22, 33, 12, 23, 13), which is not as common as Voigt's notation of (11, 22, 33, 23, 13, 12).

For a material with three orthogonal planes of symmetry in the x-y, y-z, and x-z planes, known as an orthotropic material, the compliance matrix can be expressed

in terms of the engineering constants as shown in Equation (3.26).

$$\begin{bmatrix} \varepsilon_{11} \\ \varepsilon_{22} \\ \varepsilon_{33} \\ 2\varepsilon_{12} \\ 2\varepsilon_{23} \\ 2\varepsilon_{13} \end{bmatrix} = \begin{bmatrix} \frac{1}{E_{11}} & -\frac{\nu_{21}}{E_{22}} & -\frac{\nu_{31}}{E_{33}} & 0 & 0 & 0 \\ -\frac{\nu_{12}}{E_{11}} & \frac{1}{E_{22}} & -\frac{\nu_{32}}{E_{33}} & 0 & 0 & 0 \\ -\frac{\nu_{13}}{E_{11}} & -\frac{\nu_{23}}{E_{22}} & \frac{1}{E_{33}} & 0 & 0 & 0 \\ 0 & 0 & 0 & \frac{1}{G_{12}} & 0 & 0 \\ 0 & 0 & 0 & 0 & \frac{1}{G_{23}} & 0 \\ 0 & 0 & 0 & 0 & 0 & \frac{1}{G_{13}} \end{bmatrix} \cdot \begin{bmatrix} \sigma_{11} \\ \sigma_{22} \\ \sigma_{33} \\ \sigma_{12} \\ \sigma_{23} \\ \sigma_{13} \end{bmatrix} \tag{3.26}$$

For a material with the orthotropic symmetries and rotational symmetry in the y-z plane, known as a transversely isotropic material, the compliance matrix can be expressed in terms of the engineering constants as shown in Equation (3.27). In this case, $\nu_{23} = \nu_{32}$, $E_{22} = E_{33}$, and $G_{12} = G_{13}$.

$$\begin{bmatrix} \varepsilon_{11} \\ \varepsilon_{22} \\ \varepsilon_{33} \\ 2\varepsilon_{12} \\ 2\varepsilon_{23} \\ 2\varepsilon_{13} \end{bmatrix} = \begin{bmatrix} \frac{1}{E_{11}} & -\frac{\nu_{21}}{E_{22}} & -\frac{\nu_{21}}{E_{22}} & 0 & 0 & 0 \\ -\frac{\nu_{12}}{E_{11}} & \frac{1}{E_{22}} & -\frac{\nu_{23}}{E_{22}} & 0 & 0 & 0 \\ -\frac{\nu_{12}}{E_{11}} & -\frac{\nu_{23}}{E_{22}} & \frac{1}{E_{22}} & 0 & 0 & 0 \\ 0 & 0 & 0 & \frac{1}{G_{12}} & 0 & 0 \\ 0 & 0 & 0 & 0 & \frac{2(1+\nu_{23})}{E_{22}} & 0 \\ 0 & 0 & 0 & 0 & 0 & \frac{1}{G_{12}} \end{bmatrix} \cdot \begin{bmatrix} \sigma_{11} \\ \sigma_{22} \\ \sigma_{33} \\ \sigma_{12} \\ \sigma_{23} \\ \sigma_{13} \end{bmatrix} \tag{3.27}$$

For a material with transversely isotropic symmetries and rotational symmetry in the x-y and x-z plane, known as an isotropic material, the compliance matrix can

be expressed in terms of the engineering constants as shown in Equation (3.28).

$$\begin{bmatrix} \varepsilon_{11} \\ \varepsilon_{22} \\ \varepsilon_{33} \\ 2\varepsilon_{12} \\ 2\varepsilon_{23} \\ 2\varepsilon_{13} \end{bmatrix} = \frac{1}{E} \begin{bmatrix} 1 & -\nu & -\nu & 0 & 0 & 0 \\ -\nu & 1 & -\nu & 0 & 0 & 0 \\ -\nu & -\nu & 1 & 0 & 0 & 0 \\ 0 & 0 & 0 & 2(1+\nu) & 0 & 0 \\ 0 & 0 & 0 & 0 & 2(1+\nu) & 0 \\ 0 & 0 & 0 & 0 & 0 & 2(1+\nu) \end{bmatrix} \cdot \begin{bmatrix} \sigma_{11} \\ \sigma_{22} \\ \sigma_{33} \\ \sigma_{12} \\ \sigma_{23} \\ \sigma_{13} \end{bmatrix} \tag{3.28}$$

III.A.5. Weak Form Derivation

Deriving the weak form to be used in numerical methods begins with the balance of linear momentum. For a body in static equilibrium, the balance of linear momentum is given by Equation (3.29). Using the principle of virtual work, the equation is multiplied by a variation of the displacement and integrated over the volume, as shown in Equation (3.30).

$$\frac{\partial \sigma_{ji}}{\partial x_i} + f_i = 0 \tag{3.29}$$

$$\int \delta u_i \left(\frac{\partial \sigma_{ji}}{\partial x_i} + f_i \right) dV = 0 \tag{3.30}$$

Integrating the first term of Equation (3.30) by parts results in Equation (3.31).

$$\int \frac{\partial \delta u_i \sigma_{ji}}{\partial x_i} - \sigma_{ji} \delta \frac{\partial u_i}{\partial x_i} + \delta u_i f_i dV = 0 \tag{3.31}$$

Using the divergence theorem, the equation can be expressed as given in Equation (3.32).

$$\int \delta u_i \sigma_{ji} n_j dA + \int \delta u_i f_i - \sigma_{ji} \delta \frac{\partial u_i}{\partial x_i} dV = 0 \tag{3.32}$$

Finally, the weak form given in Equation (3.33) can be obtained by leveraging the definition of the infinitesimal strain tensor and the symmetry of the stress tensor.

$$\int t_i \delta u_i dA + \int f_i \delta u_i - \sigma_{ij} \delta \varepsilon_{ij} dV = 0 \tag{3.33}$$

III.A.6. Finite Element Model

The displacements within a finite element, governed by Equation (3.33), are approximated using interpolation functions, ψ, such that the function has the value of 1 at the corresponding position of the i^{th} node, $\boldsymbol{x}^i$, and 0 at all other nodal locations, as expressed in Equation (3.34), where superscripts indicate the corresponding node.

$$\psi^i(\boldsymbol{x}^j) = \delta_{ij} \tag{3.34}$$

In addition, the interpolation functions at any location within the element sum to 1, as expressed in Equation (3.35).

$$\sum_i^n \psi^i(x) = 1 \tag{3.35}$$

The variational displacement, δu in Equation (3.33), at any point, $\boldsymbol{x}$, within an element is then given approximated by Equation (3.36), where subscripts indicate the direction of the displacement and superscripts indicate the corresponding node.

$$\delta u_i(\boldsymbol{x}) \approx \sum_k^n \psi^k(\boldsymbol{x}) \delta u_i^j \tag{3.36}$$

Using Equation (3.36), the form for strain can be derived and results in Equation (3.37).

$$\delta \varepsilon_{ij}(\boldsymbol{x}) \approx \frac{1}{2} \left(\sum_k^n \frac{\partial \psi^k(\boldsymbol{x})}{\partial x_j} \delta u_i^k + \sum_k^n \frac{\partial \psi^k(\boldsymbol{x})}{\partial x_i} \delta u_j^k \right) \tag{3.37}$$

Applying the weak form equation to the element, substituting the approximation for the displacements and strains, and using the symmetry of the stress tensor results in Equation (3.38).

$$\sum_{k}^{n}\left(\left[\int t_i(\boldsymbol{x})\psi^k(\boldsymbol{x})dA_e+\int f_i(\boldsymbol{x})\psi^k(\boldsymbol{x})-\sigma_{ij}(\boldsymbol{x})\frac{\partial\psi^k(\boldsymbol{x})}{\partial x_j}dV_e\right]\delta u_i^k\right)=0 \tag{3.38}$$

Since the variation of the displacement, δu, is arbitrary, the first term in Equation (3.38) must equal zero. Setting the term equal to zero and rearranging the equation results in Equation (3.39).

$$\int\sigma_{ij}\frac{\partial\psi^k(\boldsymbol{x})}{\partial x_j}dV_e u_m^k=\int t_i(\boldsymbol{x})\psi^k(\boldsymbol{x})dA_e+\int f_i(\boldsymbol{x})\psi^k(\boldsymbol{x})dV_e \tag{3.39}$$

At this point it is convenient to take the right hand side of Equation (3.39) and create a single force vector, $\boldsymbol{F}^e$, which includes forces due to applied tractions on the boundaries and body forces acting on the volume, where the indices are ordered by nodes then by the components, as shown in Equation (3.40).

$$\boldsymbol{F}^e=\begin{bmatrix}\int t_1(\boldsymbol{x})\psi^1(\boldsymbol{x})dA_e+\int f_1(\boldsymbol{x})\psi^1(\boldsymbol{x})dV_e\\ \int t_2(\boldsymbol{x})\psi^1(\boldsymbol{x})dA_e+\int f_2(\boldsymbol{x})\psi^1(\boldsymbol{x})dV_e\\ \int t_3(\boldsymbol{x})\psi^1(\boldsymbol{x})dA_e+\int f_3(\boldsymbol{x})\psi^1(\boldsymbol{x})dV_e\\ \vdots\\ \int t_1(\boldsymbol{x})\psi^n(\boldsymbol{x})dA_e+\int f_1(\boldsymbol{x})\psi^n(\boldsymbol{x})dV_e\\ \int t_2(\boldsymbol{x})\psi^n(\boldsymbol{x})dA_e+\int f_2(\boldsymbol{x})\psi^n(\boldsymbol{x})dV_e\\ \int t_3(\boldsymbol{x})\psi^n(\boldsymbol{x})dA_e+\int f_3(\boldsymbol{x})\psi^n(\boldsymbol{x})dV_e\end{bmatrix} \tag{3.40}$$

In order to change the left hand side of Equation (3.39) to a similar form, the stress, strains, and constitutive matrix will be expressed in contracted notation. As mentioned in an earlier section, the order of the stresses and strains in the contracted

notation is arbitrary as long as the order is consistent, and the code used for this work orders the stress and strains as shown in Equation (3.41).

$$\varepsilon_i = \begin{bmatrix} \varepsilon_{11} \\ \varepsilon_{22} \\ \varepsilon_{33} \\ 2\varepsilon_{12} \\ 2\varepsilon_{23} \\ 2\varepsilon_{13} \end{bmatrix} \qquad \sigma_i = \begin{bmatrix} \sigma_{11} \\ \sigma_{22} \\ \sigma_{33} \\ \sigma_{12} \\ \sigma_{23} \\ \sigma_{13} \end{bmatrix} \tag{3.41}$$

For convenience, the $\boldsymbol{B}$ matrix is defined by Equation (3.42) and relates the approximation of strain at any point within the element, $\boldsymbol{X}$, to the nodal displacements such that $\varepsilon_i \approx \sum_k^n B_{ij} u_j^k$.

$$\boldsymbol{B} = \begin{bmatrix} \frac{\partial \psi^1(\boldsymbol{x})}{\partial x_1} & 0 & 0 & \dots & \frac{\partial \psi^n(\boldsymbol{x})}{\partial x_1} & 0 & 0 \\ 0 & \frac{\partial \psi^1(\boldsymbol{x})}{\partial x_2} & 0 & \dots & 0 & \frac{\partial \psi^n(\boldsymbol{x})}{\partial x_2} & 0 \\ 0 & 0 & \frac{\partial \psi^1(\boldsymbol{x})}{\partial x_3} & \dots & 0 & 0 & \frac{\partial \psi^n(\boldsymbol{x})}{\partial x_3} \\ \frac{\partial \psi^1(\boldsymbol{x})}{\partial x_1} & \frac{\partial \psi^1(\boldsymbol{x})}{\partial x_2} & 0 & \dots & \frac{\partial \psi^n(\boldsymbol{x})}{\partial x_1} & \frac{\partial \psi^n(\boldsymbol{x})}{\partial x_2} & 0 \\ 0 & \frac{\partial \psi^1(\boldsymbol{x})}{\partial x_2} & \frac{\partial \psi^1(\boldsymbol{x})}{\partial x_3} & \dots & 0 & \frac{\partial \psi^n(\boldsymbol{x})}{\partial x_2} & \frac{\partial \psi^n(\boldsymbol{x})}{\partial x_3} \\ \frac{\partial \psi^1(\boldsymbol{x})}{\partial x_1} & 0 & \frac{\partial \psi^1(\boldsymbol{x})}{\partial x_3} & \dots & \frac{\partial \psi^n(\boldsymbol{x})}{\partial x_1} & 0 & \frac{\partial \psi^n(\boldsymbol{x})}{\partial x_3} \end{bmatrix} \tag{3.42}$$

Similar to the order of the force vector in Equation (3.40), the nodal displacements can be written in the form of a single vector ordered by node then by dis-

placement component, as shown in Equation (3.43).

$$\boldsymbol{q}^e = \begin{bmatrix} u_1^1 \\ u_2^1 \\ u_3^1 \\ \vdots \\ u_1^n \\ u_2^n \\ u_3^n \end{bmatrix} \tag{3.43}$$

Finally, substituting Equation (3.40), Equation (3.42), and Equation (3.43) into Equation (3.39), the final form of the finite element formulation can be written as Equation (3.44).

$$\int B_{ki} C_{kl} B_{lj} dV_e q_j^e = K_{ij}^e q_j^e = F_i^e \tag{3.44}$$

III.A.7. Numerical Integration

The closed form integration of these expressions over the element's volume and area are prohibitively complex for high order element types or complex geometries. As a result, numerical integration techniques are often employed. To simplify the integration, the coordinate system of the element is mapped to the coordinates of what is called the "master" element, which is the element in a simple configuration with the domain going from -1 to 1 along the axes.

After the mapping has been done, quadrature is used to approximate the integral over the master element domain. There are many types of quadrature schemes, but this work only uses Gauss quadrature and Newton-Cotes quadrature.

Instead of the coordinates being given by $\boldsymbol{x}$, the coordinates in this new coordinate system of the master element will be denoted by $\boldsymbol{\xi}$. The relation between the coordinate systems can be approximated by Equation (3.45).

$$x_i(\boldsymbol{\xi}) \approx \sum_{k}^{n} x_i^k \psi^k(\boldsymbol{\xi}) \tag{3.45}$$

the derivatives of the interpolation functions are needed for the calculation of the $\boldsymbol{B}$ matrix, so the derivatives transformed to the $\boldsymbol{\xi}$ coordinate system will be needed and are given by Equation (3.46).

$$\frac{\partial \psi^k(\boldsymbol{\xi})}{\partial \xi_i} = \frac{\partial x_j}{\partial \xi_i} \frac{\partial \psi^k(\boldsymbol{x})}{\partial x_j} = J_{ij} \frac{\partial \psi^k(\boldsymbol{x})}{\partial x_j} \tag{3.46}$$

In the transformation of the derivatives, the transformation matrix, $\boldsymbol{J}$, is known as the Jacobian and can be approximated by Equation (3.47).

$$J_{ij} = \frac{\partial x_j}{\partial \xi_i} \approx \sum_{k}^{n} x_j^k \frac{\partial \psi^k(\boldsymbol{\xi})}{\partial \xi_i} \tag{3.47}$$

The $\boldsymbol{B}$ matrix developed in Equation (3.42) contains derivatives of the interpolation functions in terms of $\boldsymbol{x}$, so the inverse of Equation (3.46) is needed as given in Equation (3.48).

$$\frac{\partial \psi^k(\boldsymbol{x})}{\partial x_i} = J_{ij}^{-1} \frac{\partial \psi^k(\boldsymbol{\xi})}{\partial \xi_j} \tag{3.48}$$

The integration over the volume of the element, V_e, can be transformed to the master element, $\hat{V}_e$, domain using Equation (3.49).

$$dV_e = |\boldsymbol{J}^{-1}| d\hat{V}_e \tag{3.49}$$

The stiffness matrix, $\boldsymbol{K}$, can then be written as an integration over the master element domain as given in Equation (3.50), where the $\boldsymbol{B}$ matrix now contains the

derivatives of the interpolation function in terms of $\boldsymbol{\xi}$ using Equation (3.48).

$$\boldsymbol{K} = \int \boldsymbol{B}(\boldsymbol{x})^T \boldsymbol{C}\boldsymbol{B}(\boldsymbol{x}) dV_e = \int \boldsymbol{B}(\boldsymbol{\xi})^T \boldsymbol{C}\boldsymbol{B}(\boldsymbol{\xi}) |\boldsymbol{J}^{-1}| d\hat{V}_e \tag{3.50}$$

A very similar transformation can be made for the force vector derived in Equation (3.40). With the integrals in terms of the master element domain, quadrature is used to numerically approximate the integration. The integral over a function, $f(\boldsymbol{\xi})$, can be approximated by a summation of the function evaluated at specific points, called quadrature points, times the weight of those points, W, as shown in Equation (3.51), where L, M, and N is the number of quadrature points in the ξ_1, ξ_2, and ξ_3 directions respectively.

$$\int_{-1}^{1}\int_{-1}^{1}\int_{-1}^{1} f(\boldsymbol{\xi}) d\xi_1 d\xi_2 d\xi_3 \approx \sum_{i=1}^{L}\sum_{j=1}^{M}\sum_{k=1}^{N} f(\xi_1^i, \xi_2^j, \xi_3^k) W_i W_j W_k \tag{3.51}$$

In this work, the same number of quadrature points is used in each direction, since the solution is assumed to vary with the same polynomial order in each direction.

III.A.7.a. Gauss Quadrature

Gauss quadrature chooses the points and weights such that the numerical integration is exact for polynomials of $2M - 1$, where M is the number of quad points in each direction. For example, to exactly integrate a fourth order polynomial, only three quadrature points are needed in each direction. The quadrature point locations and weights are given in Table III.1.

Table III.1. Gauss quadrature point locations and weights for 1-4 number of quadrature points along the axis

Number of Points, M	Quad Point Locations	Weights
1	0	2
2	$\pm\sqrt{\frac{1}{3}}$	1
3	0	$\frac{8}{9}$
	$\pm\sqrt{\frac{3}{5}}$	$\frac{5}{9}$
4	$\pm\sqrt{\left(3-\frac{2\sqrt{6/5}}{7}\right)}$	$\frac{18+\sqrt{30}}{30}$
	$\pm\sqrt{\left(3+\frac{2\sqrt{6/5}}{7}\right)}$	$\frac{18-\sqrt{30}}{30}$

III.A.7.b. Newton-Cotes Quadrature

Newton-Cotes quadrature evenly spaces the points, unlike Gaussian quadrauture, and exactly integrates a polynomial of order $M-1$. While Gauss quadrature only takes three points in each direction to exactly integrate a fourth order polynomial, Newton-Cotes quadrature requires five. For most cases Gauss quadrature is preferred, but in very specific cases, such as cohesive zone elements, Newton-Cotes quadrature might be preferred for numerical reasons. The quadrature point locations and weights are given in Table III.2.

III.B. Models and Approach for Determining Constituent Properties

This section describes the models used to represent the hexagonal and random RVE's, the Mori-Tanaka averaging scheme, the algorithm developed to determine fiber properties, and the assumptions associated with the material properties.

Table III.2. Newton-Cotes quadrature point locations and weights for 1-5 number of quadrature points along the axis

Number of Points, M	Quad Point Locations	Weights
1	0	2
2	± 1	1
3	0	$\frac{4}{3}$
	± 1	$\frac{1}{3}$
4	$\pm \frac{1}{3}$	$\frac{3}{4}$
	± 1	$\frac{1}{4}$
5	0	$\frac{4}{15}$
	$\pm \frac{1}{2}$	$\frac{32}{45}$
	± 1	$\frac{7}{45}$

III.B.1. Microstructure Models

Two types of microstructures were examined using finite element analyses: hexagonal and random fiber arrays. Quasi-3D assumptions were utilized to reduce the analysis domain to two dimensions, reducing the number of degrees of freedom and the bandwidth of the stiffness matrix. These assumptions, given in Ref. [97], are exactly satisfied by the configuration currently being studied, so they do not introduce any inaccuracy as compared to a traditional three-dimensional analysis. In addition to FEA-based microstructural models, the Mori-Tanaka averaging scheme was utilized.

III.B.1.a. Hexagonal Array

A single unit-cell of a hexagonal array was generated for the fiber volume fraction examined. An example of this is shown in Figure I.2b. Periodic boundary conditions are applied to the unit cell by imposing the following relationship for the displacements at the unit cell boundary

$$u_i\left(x_j + d_j\right) = u_i\left(x_j\right) + \left\langle \frac{\partial u_i}{\partial x_k} \right\rangle d_k \tag{3.52}$$

Repeated indices imply summation, and d_k is a vector of periodicity that starts at some coordinate x_j in one unit cell and ends at the equivalent point in another unit cell. Angle brackets imply the volume-averaged value of a field variable. A more in-depth description of the imposition of periodic boundary conditions is given by the Appendix A and Ref. [98].

III.B.1.b. Random Fiber Arrangement

Figure I.2a shows a micrograph of an actual lamina, illustrating that physical laminae do not exhibit a uniform distribution of fibers but rather have some random distribution. As a result, this work aims to model the lamina microstructure more accurately by introducing randomness into the arrangement of fibers, as Figure I.2c shows. This work made use of a procedure to create a periodic RVE that contains randomly positioned fibers developed by Ross Mclendon, see Ref. [99]. Random positioning of fibers is accomplished by iteratively adjusting fiber positions to resolve spatial interference. This approach results in some fibers being in extremely close proximity to one another.

Periodicity in the mesh is obtained by periodic mesh seeding along the edges.

Periodic boundary conditions are imposed in the same manner as for the hexagonal array. A more detailed description of the boundary conditions are shown in the Appendix A.

A minimum spacing between fibers can be enforced by creating a random microstructure using a larger volume fraction and fiber diameter than desired (see Figure III.2a), then shrinking each fiber's diameter (see Figure III.2b).

For this work, the minimum spacing fraction is defined to be the minimum distance, s, between any two fibers divided by the radius of the fiber, r, as illustrated in Figure III.3. The relationship between the minimum spacing fraction, , the artificially large volume fraction, $V_f^{'}$, and the final volume fraction, V_f, is given by

$$\xi = 2\left(\sqrt{\frac{V'_f}{V_f}} - 1\right) \tag{3.53}$$

The largest value of fiber spacing for a given volume fraction is limited by the largest possible value of $V_f^{'}$, which in theory can be about 90.7%, corresponding to hexagonal close packing arrangement for circles. In practice, the algorithm for generating the random RVE's cannot achieve the theoretical limit due in part to the fact that a periodic hexagonal arrangement cannot be represented by a square RVE. As the size of the RVE increases, the square shape has less of an effect on the maximum volume fraction. The larger the RVE, the closer the algorithm can get to the theoretical volume fraction limit.

III.B.1.c. Mori-Tanaka Averaging Scheme

The Mori-Tanaka averaging scheme considers inhomogeneities placed into an infinite medium of the matrix material. It accounts for interactions between phases

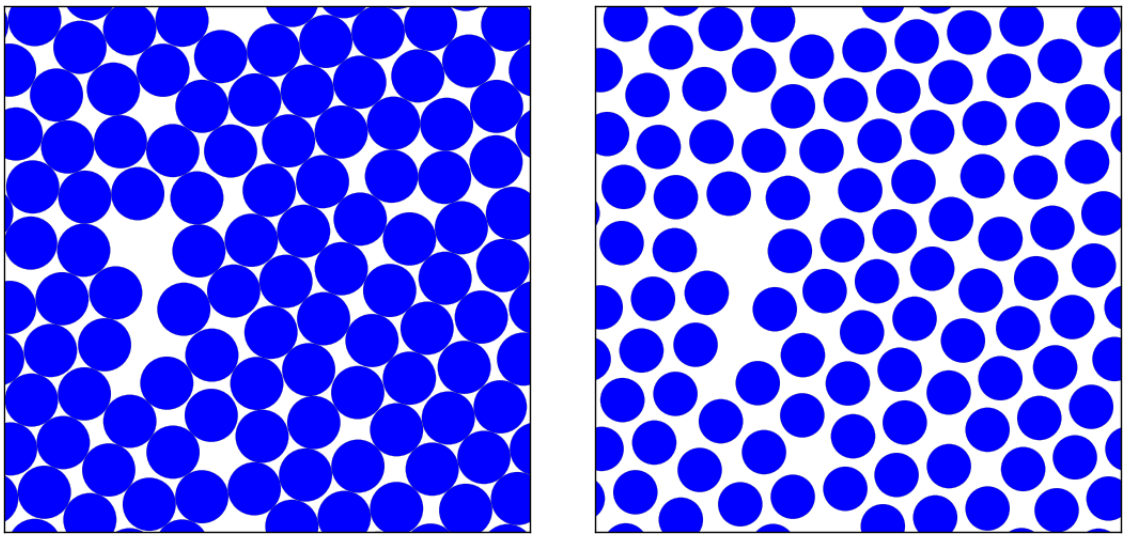

(a) Initial configuration with artificially higher fiber volume fraction and fiber diameter

(b) Final configuration after shrinking fiber

Figure III.2. Microstructure with specified minimum spacing between fibers

through averaging and the geometry of the inhomogeneities (cylinders in this case) through the Eshelby tensor. However, the Mori-Tanaka averaging scheme does not account for the size and locations of the inhomogeneities [100].

An implementation of the Mori-Tanaka averaging was developed and used to inversely determine fiber properties. The implementation used in this work exactly matched the predicted properties for T650-35 in Ref. [2], who used the same method.

III.B.2. Inverse Method for Fiber Property Determination

The procedure for determining the fiber properties involves the solution of an inverse problem. A micromechanics model uses the fiber and matrix properties to determine the homogenized composite's properties. In the case of the Mori-Tanaka averaging scheme with an isotropic matrix material, the relationship can be inverted,

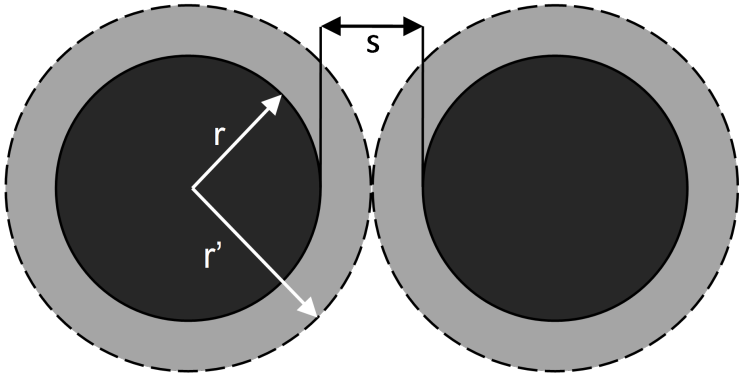

Figure III.3. Definition of minimum spacing fraction

and the fiber properties can be solved for directly. However, it is not possible to invert this input-output relationship for finite element models. In these cases, the problem is solved by iteratively identifying fiber properties which cause the model to yield lamina properties that match the expected values. For convenience, the unique engineering constants of the fiber and lamina properties are expressed as vectors. The ordering of the properties within the vector is not important, but if the fibers and lamina have a different number of independent engineering constants, the problem becomes a minimization problem rather than a root finding problem, which is addressed at the end of this section. For the case of transverse isotropy of the fiber and lamina properties, the constants are expressed as vectors in the following manner for the lamina, ^{L}, and fiber, ^{f}.

$$\Gamma^L = \left[E_1^L, E_2^L, G_{12}^L, G_{23}^L, \nu_{12}^L\right] \Gamma^f = \left[E_1^f, E_2^f, G_{12}^f, G_{23}^f, \nu_{12}^f\right] \tag{3.54}$$

The micromechanics model serves as a function which operates as follows

$$\Gamma^L = f\left(\Gamma^f\right) \tag{3.55}$$

In the case of a hexagonal unit cell, this function represents a single finite element model. For a random RVE, this function represents the average of multiple realizations of the microstructure. The goal is to find a collection of fiber properties such that the residual of the lamina properties decreases to within a given tolerance, ϵ.

$$\epsilon_i = \Gamma_i^L - \bar{\Gamma}_i^L \cong 0 \tag{3.56}$$

The overbar signifies the lamina properties from experiments. Because of the large differences in the magnitudes of the properties, the residuals are defined in terms of normalized properties, which are the properties divided by the initial guess of the fiber properties.

$$\hat{\epsilon}_i = \frac{\epsilon_i}{\Gamma_i^{f^0}} = \frac{\Gamma_i^L - \bar{\Gamma}_i^L}{\Gamma_i^{f^0}} \quad \text{(no summation on i)} \tag{3.57}$$

$$\hat{\Gamma}_i^f = \frac{\Gamma_i^f}{\Gamma_i^{f^0}} \quad \text{(no summation on i)} \tag{3.58}$$

The Newton-Raphson method is used to find the value of the fiber properties that result in the correct lamina properties. To avoid numerical problems, the Jacobian matrix is in terms of the normalized fiber and lamina properties.

$$J_{ij} = \frac{\partial \hat{\epsilon}_i}{\partial \hat{\Gamma}_j^f} \cong \frac{\Delta \hat{\epsilon}_i}{\Delta \hat{\Gamma}_j^f} \tag{3.59}$$

The initial guess is obtained from the literature, similar material systems, or intuition, if no better source is available. It is only necessary that each engineering constant in the guess have a realistic order of magnitude, but accurate guesses can significantly help the time to convergence. For each Newton-Raphson iteration, a better approximation for the fiber properties is obtained by calculating the correction

term, $\Delta\hat{\epsilon}_i$, as shown in Equation (3.60).

$$J_{ij} = \frac{\partial \hat{\epsilon}_i}{\partial \hat{\Gamma}_j^f} \cong \frac{\Delta \hat{\epsilon}_i}{\Delta \hat{\Gamma}_j^f} \tag{3.60}$$

The correction term $\Delta\hat{\epsilon}_i$ must be calculated for each iteration. When the number of fiber constants, Γ^f, match the number of lamina constants, Γ^L, the calculation of the correction term in Equation (3.60) requires the solution of a set of linear equations. However, when the number of fiber constants does not match the number of lamina constants, Equation (3.60) requires a least squares solve for the correction term that minimizes the residual of the system of equations. Iteration on the fiber properties continue until either the L-2 norm of the normalized residual decreases to a value less than or equal to 1.0e-6 or stops decreasing and reaches an asymptotic value, at which point the fiber properties have been determined.

Several steps are taken to help expedite the solution process. The first is the use of the modified Newton's method. The calculation of the gradient matrix is computationally expensive, requiring lamina properties to be determined for multiple different sets of fiber properties. One set corresponds to the current approximation of the fiber properties, while the other sets of properties perturb one of the fiber properties by 1% to obtain gradients. Due to this high cost, the gradient matrix is not recalculated for every iteration. Instead, it is reused as long as an acceptable rate of convergence is obtained (50% reduction in residual on each iteration). Also, it should be noted that some iterations lead to fiber properties that are not physically realistic. Therefore, the allowable fiber properties are bounded such that moduli remain positive and Poisson's ratios remain between 0.01 and 1.0. If an increment results in a fiber property that lies outside these bounds, the property is set to

the respective limit for that iteration. Figure III.4 illustrates the described inverse method. As the figure shows, the step to calculate the lamina properties differs depending on the microstructure, which is shown to the right in Figure III.4. For the random RVE's, many realizations are used, so averaging is required. For the hexagonal RVE, only one solution is needed.

Each iteration involves the solution of one homogenization problem for each realization when the gradient matrix does not need to be updated or multiple homogenization problems for each realization when the gradient matrix does need to be updated. Consequently, it is common that more than a thousand FEA problems must be solved to obtain a single set of converged fiber properties. Due to this expense for the random case, the solution is expedited by initially calculating the effective properties for a small RVE size (2 fibers for this work). This result is then used as the initial guess for larger RVE sizes, since the small RVE tends to give a fair prediction for the fiber properties and is much faster to run.

Investigations showed that this approach yields the same solution for a variety of initial fiber property guesses. Furthermore, consistency was tested in the following manner. Lamina properties were obtained for an arbitrary set of fiber properties. Then, the inverse method was applied using those lamina properties, and the process converged to the original fiber properties as expected.

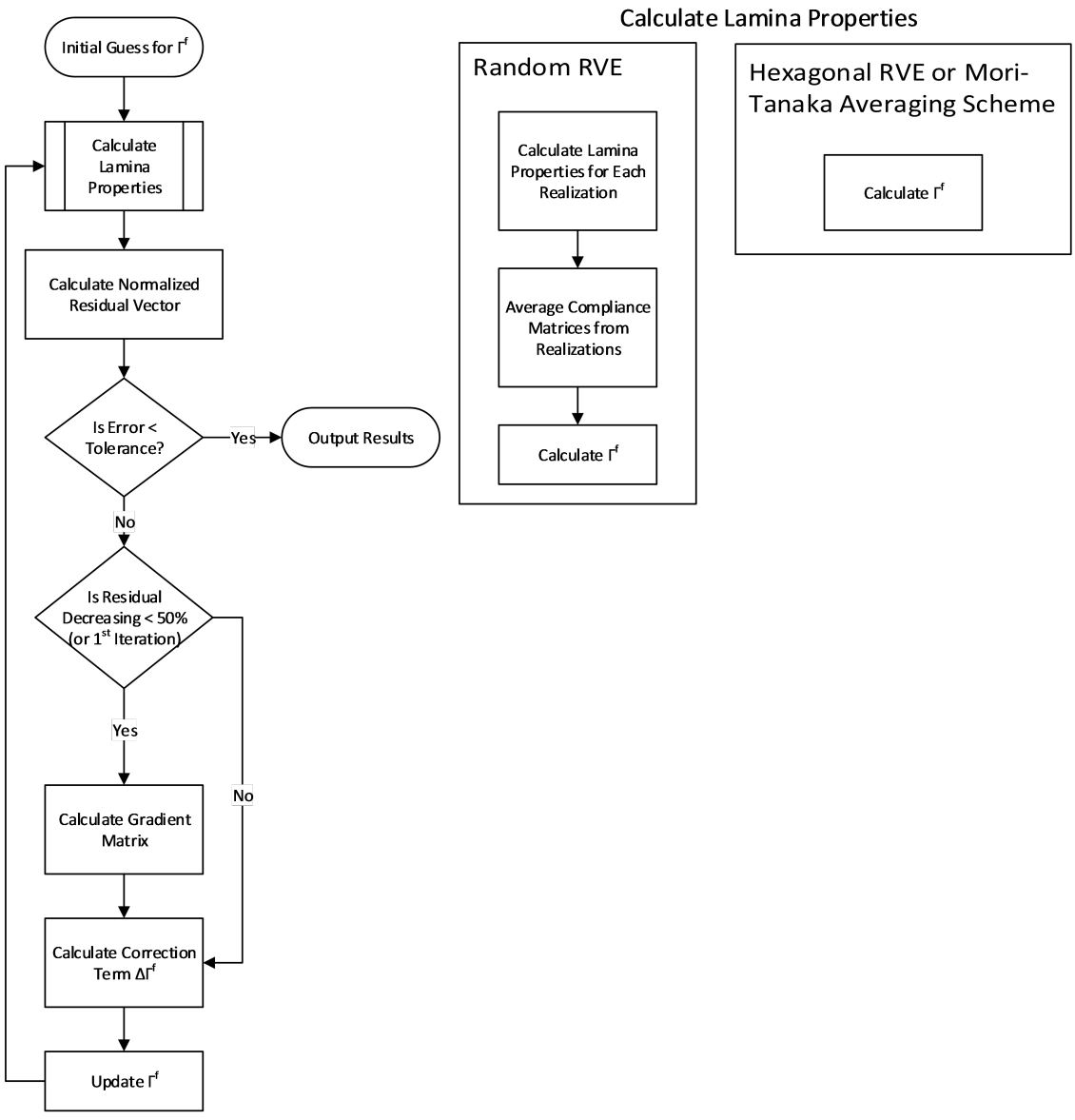

Figure III.4. Flow of algorithm used to determine fiber properties solving inverse problem

III.B.3. Material Properties

In this work, the properties of the unidirectional composites are assumed to be transversely isotropic. For the graphite fiber material systems, the fiber properties are assumed to be transversely isotropic, and for the glass fiber material system, the fiber properties are assumed to be isotropic.

For random microstructures with the RVE sizes currently being examined, a single realization is not expected to exhibit transverse isotropy or even orthotropy. In general, the anisotropic compliance matrix will follow the form as given in Equation (3.61). For fully anisotropic materials, there are 21 unique constants that characterize the constitutive law.

$$S = \begin{bmatrix} S_{11} & S_{12} & S_{13} & S_{14} & S_{15} & S_{16} \\ S_{12} & S_{22} & S_{23} & S_{24} & S_{25} & S_{26} \\ S_{13} & S_{23} & S_{33} & S_{34} & S_{35} & S_{36} \\ S_{14} & S_{24} & S_{34} & S_{44} & S_{45} & S_{46} \\ S_{15} & S_{25} & S_{35} & S_{45} & S_{55} & S_{56} \\ S_{16} & S_{26} & S_{36} & S_{46} & S_{56} & S_{66} \end{bmatrix} \tag{3.61}$$

For orthotropic properties, the compliance matrix will follow the form as given in Equation (3.62), for which there are 9 unique engineering constants. To enforce the assumption of orthotropy, the non-orthotropic terms must be eliminated, and there are two methods to accomplish this. The effects of the two methods on the

results will be compared.

$$S = \begin{bmatrix} S_{11} & S_{12} & S_{13} & 0 & 0 & 0 \\ S_{12} & S_{22} & S_{23} & 0 & 0 & 0 \\ S_{13} & S_{23} & S_{33} & 0 & 0 & 0 \\ 0 & 0 & 0 & S_{44} & 0 & 0 \\ 0 & 0 & 0 & 0 & S_{55} & 0 \\ 0 & 0 & 0 & 0 & 0 & S_{66} \end{bmatrix} \tag{3.62}$$

One method to eliminate non-orthotropic terms (the non-zero terms in Equation (3.61) that are zero in Equation (3.62)) , assumes that for an applied normal strain, the shear stresses are assumed to be zero, and for an applied shear strain, all stresses are assumed to be zero except the respective shear stress. This corresponds to setting the non-orthotropic terms in the compliance matrix of Equation (3.61) to zero.

The other method to eliminate non-orthotropic terms assumes that for an applied normal stress, the shear strains are assumed to be zero, and for an applied shear stress, all strains are assumed to be zero except the respective shear strain. This corresponds to eliminating the terms in the stiffness matrix rather than the compliance matrix.

For transversely isotropic properties, there are 5 unique engineering constants. Though the homogenized properties for a single realization are not expected to match the form for transversely isotropic materials, the unidirectional fiber matrix material properties are assumed to be transversely isotropic in this study. Therefore, in the random RVE case, the following average predicted lamina properties from all the

realizations are averaged to enforce transverse isotropy: E_2 and E_3, G_{12} and G_{13}, and ν_{12} and ν_{13}. The percent differences between these properties that should be equal are used to measure how transversely isotropic the predicted lamina properties are and choose the RVE size and number of realizations.

III.B.4. Composite Systems

This section describes the fiber types to be analyzed and the material systems used in the determination of fiber properties. It also discusses the inconsistencies in the properties reported by the literature for the material systems and fibers.

III.B.4.a. Systems Considered

This study considers the graphite fibers of IM7, T650-35, T300, and AS4. Each of these are common graphite fibers used in fiber matrix composites for which measured lamina properties are given in the literature. The material systems used to predict the properties of the graphite fibers are IM7/8552, IM7/5250-4, T650-35/PMR-15, T300/BSL914C, and AS4/3501-6, shown in Table III.3. In addition, a study of E-glass 21xK43/LY556 will be used to explore the fiber property prediction for isotropic fibers.

III.B.4.b. Inconsistencies in Literature

For unidirectional composites, it is widely held that a rule of mixtures approximation using the longitudinal Young's modulus of the lamina and matrix and the volume fractions of the constituents provides a very good approximation for the fiber longitudinal Young's modulus. Less than 0.1% difference was measured between the

Table III.3. Lamina and matrix elastic properties taken from literature

	IM7/ 5250-4 [4]	**IM7/ 8552 [101]**	**T650-35/ PMR-15 [2]**	**T300/ BSL914C [102]**	**AS4/ 3501-6 [102]**	**E-glass 21xK43/ LY556 [102]**
Rep. V_f			55.60%	60.00%	60.00%	62.00%
Calc. V_f	59.45%	59.09%	51.34%	59.29%	53.70%	65.40%
Lamina						
E_1 (GPa)	165.5	165	126.7	138	126	53.48
E_2 (GPa)	10.34	11.38	8.255	11	11	17.7
G_{12} (GPa)	5.792	5.12	4.2	5.5	6.6	5.83
G_{23} (GPa)	3.315*	3.826*	2.81	3.929*	3.929*	6.321*
ν_{12}	0.31	0.3	0.41	0.28	0.28	0.278
ν_{23}	0.56	0.487	0.4689*	0.4	0.4	0.4
Matrix						
E (GPa)	3.45	4.67	4	4	4.2	3.35
G (GPa)	1.278*	1.730*	1.46	1.481	1.567	1.241
ν	0.35	0.35	0.3699*	0.35	0.34	0.35

* Calculated using isotropic or transversely isotropic relation

rule of mixtures and finite element analysis for the material systems considered. Using a rule of mixtures approximation, the fiber volume fractions reported by some literature sources are inconsistent with the longitudinal Young's modulus of the fibers used as reported by the manufacturers. This inconsistency leads to a dilemma with two possible approaches. One option is to take the reported fiber volume fraction, lamina properties, and matrix properties as consistent and allow the longitudinal Young's modulus of the fiber to differ from the manufacturer's reported value. The other is to take the lamina properties, matrix properties, and manufacture's longitudinal Young's modulus of the fiber as consistent and calculate the fiber volume fraction of the composite, allowing it to differ from the reported values in literature. Both fiber volume fractions will be considered in the paper allowing insight into the

influence of these inconsistencies on the resulting fiber properties.

III.C. Damage Models

This section describes the damage models compared in the context of laminated composites and the numerical methods used to solve the problems. The continuum damage methods used in this work are described, followed by the derivation of the cohesive zone formulation considered. After an explanation of the methods for modeling damage, the numerical methods for solving the systems of nonlinear equations are given, including the direct method and Newton-Raphson method.

III.C.1. Continuum Damage Formulation

A progressive continuum damage model consists of two important parts: the criteria for failure, which predicts if failure has occurred, and the degradation scheme, which modifies the material response depending on the type of failure once a failure criterion is exceeded. Many continuum damage models have been developed, and some account for the interaction of stresses to cause damage, such as the Tsai-Wu criterion. However, the continuum damage models considered in this work rely on a maximum stress-based failure criterion, which evaluates each component of stress independently. The maximum stress criteria will evaluate compressive and tensile normal stresses separately, and as a result, there are nine potential modes of failure with three modes for tensile normal stress states, three modes for compressive normal stress states, and three modes for shear stress states, with each mode requiring a given maximum stress value to evaluate the failure criterion.

After a stress component exceeds the failure criteria, the properties are degraded according to the mode corresponding to the component of stress. This allows the material degradations to model the responses expected in damaged laminated composites under various modes, such as breaking of fibers or matrix cracking parallel to the fibers. Different degradation schemes have been proposed to approximate a laminated composite's response after a mode of failure, but this work will only consider a scheme very similar to the one developed by Blackketter [103], where each engineering constant of the material is divided by a respective degradation factor depending on the component of stress that initiated the failure. Unlike the failure criteria, which differentiate between tensile and compressive failure due to normal stresses, the degradation scheme degrades the material in the same manner for tensile and compressive failure modes. The degradation factors used are shown in Table III.4. If multiple failure modes occur, the engineering constants are degraded by the factor that is most severe.

Using the aforementioned failure criterion and degradation scheme, several options still exist concerning where to evaluate the failure criteria and degrade the material properties, and this work will consider two options. The first option will evaluate the failure criteria at each quadrature point, and for each quadrature that experiences a stress state exceeding the failure criteria, the properties of that quadrature point will be degraded. This method will be referred to as the quadrature point degradation method. The second option will evaluate the failure criteria at each quadrature point within an element, and once all the quadrature points within the element experience a common mode of failure, the material properties at all the

Table III.4. Degradation factors for the engineering constants to be divided by for each component of stress that causes failure

	E_1	E_2	E_3	G_{23}	G_{13}	G_{12}	ν_{23}	ν_{13}	ν_{12}
σ_{11}	100	100	100	100	100	100	100	100	100
σ_{22}	1	100	1	5	5	1	1	100	1
σ_{33}	1	1	100	1	5	5	1	1	1
σ_{23}	1	100	100	100	100	100	100	1	1
σ_{13}	1	1	100	1	100	1	1	1	1
σ_{12}	1	100	1	1	1	100	100	1	1

quadrature points within the element are degraded according to the degradation scheme for the respective mode. This method will be referred to as the element degradation method, since all quadrature points within the element are degraded at the same time.

III.C.2. Cohesive Zone Formulation

Many cohesive zone formulations have been proposed using a variety of traction-separation laws that govern the opening of the interfacial elements, but this work only uses Turon's model. [11] Turon proposed a piecewise linear traction-separation law that results in a very stiff linear behavior before the critical traction, t_c, or critical displacement, Δ_0, is exceeded, at which point damage begins, as illustrated in Figure III.5.

In the damage regime of traction-separation curve, the traction across the interface decreases linearly with the separation, until the traction is reduced to zero, which occurs at Δ_f, and a further increase in separation still results in zero traction. This formulation assumes a three dimensional element, but it can very easily be reduced to one or two dimensions by ignoring irrelevant terms. Since the traction separation law depends on the separation between the two faces of the element, it is useful to define an orthogonal coordinate system with an axis normal to the face and two axes tangential to the faces, as illustrated in Figure III.6.

The separation in the normal and tangential directions will be denoted by Δ_n, Δ_{t1}, and Δ_{t2} respectively. The traction along these axes are then given by Equation (3.63), where d is a damage parameter that prevents healing of the cohesive element.

$$\begin{aligned} t_n &= \begin{cases} (1-d)K_{penalty}\Delta_n & \text{if } \Delta_n > 0 \\ K_{penalty}\Delta_n & \text{if } \Delta_n <= 0 \end{cases} \\ t_{t1} &= (1-d)K_{penalty}\Delta_{t1} \\ t_{t2} &= (1-d)K_{penalty}\Delta_{t2} \end{aligned} \tag{3.63}$$

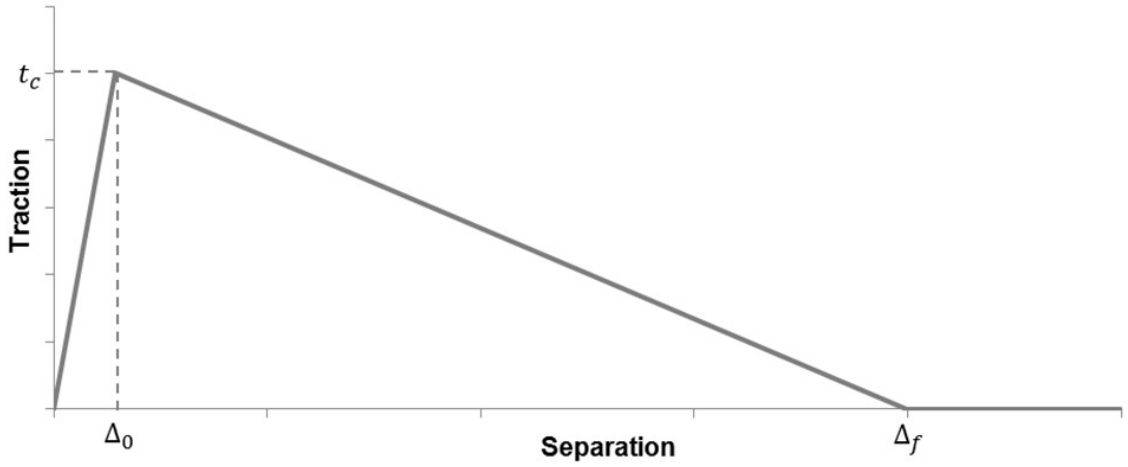

Figure III.5. Piecewise linear traction separation curve used in Turon's cohesive zone formulation

This formulation does not distinguish between the two shear modes and assumes the same critical strain energy release rates, $G_{II} = G_{III}$, and critical tractions, $t_{t1c} = t_{t2c}$, so it becomes convenient to define a single tangential separation, Δ_t, as given in Equation (3.64).

$$\Delta_t = \sqrt{(\Delta_{t1})^2 + (\Delta_{t2})^2} \tag{3.64}$$

The mode mixity, β, is defined as the ratio of the tangential separation to the sum of the normal and tangential separation, as is given in Equation (3.65).

$$\beta = \begin{cases} \frac{\Delta_t}{\Delta_t + \Delta_n} & \text{if } \Delta_n > 0 \\ 1 & \text{if } \Delta_n <= 0 \end{cases} \tag{3.65}$$

For convenience, B is defined as the ratio of the shear strain energy release rate to the total strain energy release rate and can be expressed in terms of the mode mixity, as written in Equation (3.66).

$$B = \frac{G_{II} + G_{III}}{G_I + G_{II} + G_{III}} = \frac{\beta^2}{1 + 2\beta^2 - 2\beta} \tag{3.66}$$

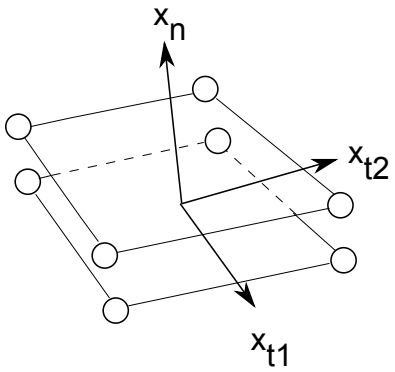

Figure III.6. Illustration of a linear 3D cohesive element with normal and tangential axes

In order to define a single damage parameter for normal and tangential separation, a mixed mode traction separation relation is needed. The mixed mode critical traction, t_c, is a function of the normal and tangential critical tractions, ratio of the shear strain energy release rate to the total strain energy release rate, and a parameter η that comes from fitting experimental data; t_c. The mixed mode critical traction is given by Equation (3.67).

$$t_c = \sqrt{t_{nc}^2 + (t_{nc}^2 - t_{tc}^2)B^\eta} \tag{3.67}$$

The separation that initiates damage in the normal and tangential directions, Δ_{n0} and Δ_{t0} respectively, are clearly defined by the critical traction and penalty stiffness as shown in Equation (3.68).

$$\begin{aligned} \Delta_{n0} &= \frac{t_{nc}}{K_{penalty}} \\ \Delta_{t0} &= \frac{t_{tc}}{K_{penalty}} \end{aligned} \tag{3.68}$$

The mixed mode separation that initiates damage can be expressed in a form similar to the mixed mode critical traction and is given in Equation (3.69).

$$\Delta_0 = \sqrt{\Delta_{n0}^2 + (\Delta_{n0}^2 - \Delta_{t0}^2)B^\eta} \tag{3.69}$$

In the traction-separation curve for normal opening, the area under the curve is G_I. Similarly, the area under the tangential traction-separation curve is G_{II} respectively. Using this relationship, the separation in the normal and tangential directions that result in the final damage state, $d = 1$, can be written as Equation (3.70).

$$\begin{aligned} \Delta_{nf} &= \frac{2G_{Ic}}{K_{penalty}\Delta_{n0}} \\ \Delta_{tf} &= \frac{2G_{IIc}}{K_{penalty}\Delta_{t0}} \end{aligned} \tag{3.70}$$

The mixed mode separation that results in the final damage state, $d = 1$, is then given by Equation (3.71).

$$\Delta_f = \frac{\Delta_{n0}\Delta_{nf} + (\Delta_{t0}\Delta_{tf} - \Delta_{n0}\Delta_{nf})B^{\eta}}{\Delta_0} \tag{3.71}$$

The effective separation, Δ_{eff} can be defined as a function of the normal and tangential separations, but to prevent overlapping faces from contributing to damage, Δ_{eff} can be expressed as Equation (3.72).

$$\Delta_{eff} = \begin{cases} \sqrt{(\Delta_n)^2 + (\Delta_{t1})^2 + (\Delta_{t2})^2} & \text{if } \Delta_n > 0 \\ \sqrt{(\Delta_{t1})^2 + (\Delta_{t2})^2} & \text{if } \Delta_n <= 0 \end{cases} \tag{3.72}$$

Finally the mixed mode damage parameter is defined as Equation (3.73).

$$d = \frac{\Delta_f(\Delta_{eff} - \Delta_0)}{\Delta_{eff}(\Delta_f - \Delta_0)} \tag{3.73}$$

To formulate the cohesive element's stiffness matrix, it is convenient to define a constitutive matrix, $\boldsymbol{D}$, that relates the tractions to the separations, see Equation (3.74).

$$t_i = D_{ij}\Delta_j \tag{3.74}$$

Using Equation (3.63), $\boldsymbol{D}$ can be written as Equation (3.75).

$$D_{ij} = \begin{cases} \begin{bmatrix} (1-d)K_{penalty} & 0 & 0 \\ 0 & (1-d)K_{penalty} & 0 \\ 0 & 0 & (1-d)K_{penalty} \end{bmatrix} & \text{if } \Delta_n > 0 \\ \begin{bmatrix} K_{penalty} & 0 & 0 \\ 0 & (1-d)K_{penalty} & 0 \\ 0 & 0 & (1-d)K_{penalty} \end{bmatrix} & \text{if } \Delta_n <= 0 \end{cases} \tag{3.75}$$

When using the Newton-Raphson scheme to solve the system of equations, the derivative of $\boldsymbol{D}$ with respect to the opening displacements, denoted by $\boldsymbol{D^{tan}}$, is useful and given by Equation (3.76), where Δ_d is the separation that if exceeded will cause the damage parameter to increase.

$$D_{ij}^{tan} = \begin{cases} \begin{cases} D_{ij} + \frac{\Delta_f \Delta_0 \Delta_i \Delta_j}{(\Delta_f - \Delta_0)(\Delta_{eff})^3} K_{penalty} & \text{if } \Delta_n > 0 \\ D_{ij} + (1 - \delta_{i1}\delta_{1j}) \frac{\Delta_f \Delta_0 \Delta_i \Delta_j}{(\Delta_f - \Delta_0)(\Delta_{eff})^3} K_{penalty} & \text{if } \Delta_n <= 0 \end{cases} & \text{if } \begin{array}{l} \Delta_{eff} < \Delta_f \\ \text{and } \Delta_{eff} > \Delta_d \end{array} \\ D_{ij} & \text{if } \begin{array}{l} \Delta_{eff} < \Delta_d \\ \text{or } \Delta_{eff} > \Delta_f \end{array} \end{cases} \tag{3.76}$$

An issue with this tangent matrix lies in the ambiguity at the location Δ_d, but this work will use the tangent constitutive relation as if $\Delta_{eff} > \Delta_d$.

In general, the cohesive zone can have an arbitrary orientation in 3D space, so there exists a transformation matrix, $\boldsymbol{Q}$, that transforms the displacements at a point from the global $\boldsymbol{x}$ coordinate system to the local coordinate system, see

Equation (3.77).

$$\begin{bmatrix} u_n \\ u_{t1} \\ u_{t2} \end{bmatrix} = \begin{bmatrix} Q_{11} & Q_{12} & Q_{13} \\ Q_{21} & Q_{22} & Q_{23} \\ Q_{31} & Q_{32} & Q_{33} \end{bmatrix} \begin{bmatrix} u_1 \\ u_2 \\ u_3 \end{bmatrix} \tag{3.77}$$

Unlike the $\boldsymbol{B}$ matrix derived in Equation (3.42), the $\boldsymbol{B}$ matrix for cohesive elements transforms the displacements, $\boldsymbol{q}$, from Equation (3.43) into the local separations, Δ_n, Δ_{t1}, and Δ_{t2} and is given by Equation (3.78).

$$B_{ij} = \begin{bmatrix} \boldsymbol{Q}\psi^1 & ... & \boldsymbol{Q}\psi^n & -\boldsymbol{Q}\psi^1 & ... & -\boldsymbol{Q}\psi^n \end{bmatrix} \quad \text{for } i = 1..3 \text{ and } j = 1..3 \cdot (2n) \tag{3.78}$$

Finally, the elemental stiffness matrix, $\boldsymbol{K}$, can be written as expressed in Equation (3.79).

$$K_{ij} = \int B_{im}^T D_{mn} B_{nj} dA \tag{3.79}$$

When using a numerical integration techniques, the coordinates must be transformed into the master element domain so quadrature can be used. First, the area of the cohesive zone face, A_e, in the undeformed configuration is given by Equation (3.80), where $\boldsymbol{S_{t1}}$ and $\boldsymbol{S_{t2}}$ are illustrated in Figure III.7.

$$A = ||\boldsymbol{S_{t1}} \times \boldsymbol{S_{t2}}|| \tag{3.80}$$

If ξ_1 and ξ_2 follow the tangential axes in the master element domain, then dA_e can be written as Equation (3.81).

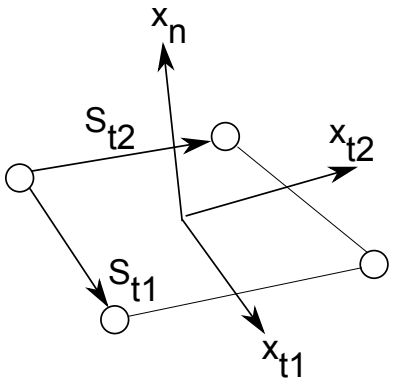

Figure III.7. Illustration of the tangential edge vectors S_{t1} and S_{t2} of a linear 3D cohesive element

$$dA_e = \sqrt{\begin{array}{l}\left(\frac{\partial x_1}{\partial \xi_1}\frac{\partial x_2}{\partial \xi_2} - \frac{\partial x_2}{\partial \xi_1}\frac{\partial x_1}{\partial \xi_2}\right)^2 \\ + \left(\frac{\partial x_2}{\partial \xi_1}\frac{\partial x_3}{\partial \xi_2} - \frac{\partial x_3}{\partial \xi_1}\frac{\partial x_2}{\partial \xi_2}\right)^2 \\ + \left(\frac{\partial x_1}{\partial \xi_1}\frac{\partial x_3}{\partial \xi_2} - \frac{\partial x_3}{\partial \xi_1}\frac{\partial x_1}{\partial \xi_2}\right)^2\end{array}} \, d\xi_1 d\xi_2 \tag{3.81}$$

With Equation (3.79) and Equation (3.81), the cohesive zone stiffness contribution can be calculated via quadrature as described in Section III.A.7.

III.C.3. Numerical Methods for Solving Nonlinear Damage Problems

When introducing damage into a finite element analysis, a nonlinearity is introduced. To solve a nonlinear problem with finite elements, some iterative algorithm is needed to find the solution that satisfies the equilibrium equation. Two iterative methods will be discussed and used in this work, the direct and Newton-Raphson method.

III.C.3.a. Direct Method

For nonlinearities due to damage, the stiffness matrix and/or force vector are functions of the solution. Let the superscript indicate the respective iteration, and let r be the current iteration, which is unknown and to be solved. The stiffness matrix, $\boldsymbol{K}$, and force vector, $\boldsymbol{F}$, is calculated using the previous known solution, $\boldsymbol{q}^{r-1}$. The new solution, $\boldsymbol{q}^r$, is then calculated by solving the linear set of equations in Equation (3.82).

$$K_{ij}(\boldsymbol{q}^{r-1})q_j^r = F_i(\boldsymbol{q}^{r-1}) \tag{3.82}$$

Iteration continues until a convergence criteria has been met, and this work uses a residual based convergence criteria. The residual is defined as written in Equation (3.83), which requires the stiffness matrix and force vector to be updated with the new solution, $\boldsymbol{q}^r$.

$$R_i^r = K_{ij}(\boldsymbol{q}^r)q_j^r - F_i^r \tag{3.83}$$

An absolute tolerance can be used such that convergence is considered to be reached when the L-2 norm of the residual is less than the tolerance as shown in Equation (3.84).

$$||\boldsymbol{R}^r|| \leq \epsilon_{abs} \tag{3.84}$$

One issue with using an absolute tolerance for the residual is the high dependence on the problem and mesh, so the tolerance must be chosen carefully. A way to decrease the problem dependence is to use a normalized convergence criterion, as shown in Equation (3.85), where ϵ_{rel} is the relative tolerance.

$$\frac{||\boldsymbol{R}^r||}{||\boldsymbol{F}^r||} \leq \epsilon_{rel} \tag{3.85}$$

III.C.3.b. Newton-Raphson Method

Consider an increment in the solution, $\boldsymbol{\Delta q}$, such that Equation (3.86).

$$\Delta q_i = q_i^r - q_i^{r-1} \tag{3.86}$$

The Taylor series expansion for the residual vector can then be written as Equation (3.87).

$$R_i^r = R_i^{r-1} + \left(\frac{\partial R_i}{\partial q_j}\right)^{r-1} \Delta q_j + \frac{1}{2!}\left(\frac{\partial^2 R_i}{\partial q_j \partial q_k}\right)^{r-1} \Delta q_j \Delta q_k + ... \tag{3.87}$$

Neglecting the higher order terms and setting $\boldsymbol{R}^r$ equal to zero, the equation can be arranged as Equation (3.88).

$$\left(\frac{\partial R_i}{\partial q_j}\right)^{r-1} \Delta q_j = -R_i^r \tag{3.88}$$

It is useful to then define a tangent stiffness matrix, $\boldsymbol{T}$, as shown in Equation (3.89).

$$T_{ij} = \frac{\partial R_i}{\partial q_j} = K_{ij} + \frac{\partial K_{ik}}{\partial q_j} q_k - \frac{\partial F_i}{\partial q_j} \tag{3.89}$$

The final form of the system of equations for solving the incremental displacement is given by Equation (3.90).

$$T_{ij}^{r-1} \Delta q_j = -R_i^{r-1} \tag{3.90}$$

III.C.4. Method for Comparing Damage Models

Several methods will be used to compare the damage models, including volume average stress-strain, crack density evolution, and two-point correlation functions.

III.C.4.a. Volume Average Stress-Strain

The most obvious method of comparison uses the volume average stress and strain of the laminated composite throughout the evolution of damage. The equations for the volume average stress and strain are shown in Equation (3.91) and Equation (3.92).

$$\sigma_{ij} = \frac{1}{V} \int \sigma_{ij} dV \tag{3.91}$$

$$\varepsilon_{ij} = \frac{1}{V} \int \varepsilon_{ij} dV \tag{3.92}$$

In the finite element analyses used in this work, the volume average stress is calculated by computing the stress within each element, but it should be noted that the cohesive zones result in no contribution to the volume average stress. The volume average strain can be computed by summing the contributions over the 3D elements and integrating over the surfaces of the interfacial elements. However, this work will use multi-point constraints to specify the volume average strain in the load direction, so no integration is needed.

III.C.4.b. Crack Density

The second method of comparison will use the evolution of crack density within the laminates. This method is useful for uniaxial load cases, since many ply cracks are expected to form in the plies not aligned with the load direction. For continuum damage models, a discrete ply crack can be difficult to define in some cases, since damage often forms wide bands, but this work will consider a ply crack as a continuous damage zone that extends completely through the height of the ply. For

cohesive zone models, a discrete crack is more easily defined and will be considered to be a line of damaged cohesive zone elements through the ply.

III.C.4.c. Two-Point Correlation Functions

Often the damage state of a finite element mesh is measured using a one-point correlation such as the fraction of damaged elements. Two-point correlation functions have been used in other applications, such as characterizing the typology of microstructures. [104, 105] The two-point correlation function, $f(h, h'|\boldsymbol{r})$, represents the probability that a point A and a point B separated by vector r will be in the damage state h and h' respectively; hence there is an infinite number of correlation functions, one for every $\boldsymbol{r}$. This work will use them to characterize the damage state of the laminated composite at applied volume average strain values of interest.

The various continuum damage models consider the degradation at individual quadrature points or an entire element, but for the comparison of the methods, any element will be considered damaged if a quadrature point within that element is damaged. Furthermore, the different modes of failure will not be distinguished between, resulting in a binary damage state for the element, with one state representing undamaged material and another representing damaged material. Though the two-point correlation functions do not require these assumptions in general, the implementation in this work will use these assumptions for the simplicity provided.

Consider a laminate with local state space, H, describing the damage state in the material, the spatial location within the laminate, denoted by $\boldsymbol{x}$, and the state of interest, denoted by h. A function, which will be referred to as the damage state

function and denoted by $d(\boldsymbol{x}, h)$, describing the volume fraction in state h at location $\boldsymbol{x}$ for an infinitesimal volume can be written as given in Equation (3.93), where V^h is the portion of the volume in state h and V is the total volume.

$$d(\boldsymbol{x}, h) = \left. \frac{V^h}{V} \right|_{\boldsymbol{x}} \tag{3.93}$$

The function, $d(\boldsymbol{x}, h)$, can be considered directly analogous to the microstructure function in literature, which describes the volume fraction of the respective constituent phase h instead of the damage state. [106] The microstructure function has the important property as described in Equation (3.94).

$$\int_H d(\boldsymbol{x}, h) dh = 1 \tag{3.94}$$

Discretely dividing the values of the local state space, H, into N values and discretely dividing the volume into a structured grid of S volume elements results in Equation (3.95), where $\boldsymbol{s}$ denotes the location of the volume element in the discretized domain.

$$\sum_{N}^{n=1} d_{\boldsymbol{s}}^n = 1 \tag{3.95}$$

The two-point correlation function, $f(h, h'|\boldsymbol{r})$, is defined by Equation (3.96), where $\boldsymbol{r}$ denotes an admissible vector in the domain Ω and $vol(\Omega|_{\boldsymbol{r}})$ denotes the admissible volume where both $\boldsymbol{x}$ and $\boldsymbol{x} + \boldsymbol{r}$ lie inside the domain.

$$f(h, h'|\boldsymbol{r}) = \frac{1}{vol(\Omega|_{\boldsymbol{r}})} \int_{\Omega|_{\boldsymbol{r}}} d(\boldsymbol{x}, h) d(\boldsymbol{x} + \boldsymbol{r}, h') d\boldsymbol{x} \tag{3.96}$$

To calculate this function exactly, integration over the domain is necessary, but an approximation was made by discretizing the continuous domain into a finite

number of points, with each point representing a discrete volume of the domain, as illustrated in Figure III.8. With this discretization, there is a finite number of points to evaluate.

As $\boldsymbol{r}$ represented a vector in the continuous domain, let $\boldsymbol{t}$ represent a vector in the discretized domain. There is now a discrete number of vectors $\boldsymbol{t}$ to be considered for the two point correlation function, all of which can be found by picking a single starting point and drawing a vector to all other discrete points.

Let $\boldsymbol{R}$ denote a subset of the discretized domain such that both $\boldsymbol{s}$ and $\boldsymbol{s}+\boldsymbol{t}$ are admissible, where $N_{\boldsymbol{R}}$ is the number of volume elements in domain $\boldsymbol{R}$. Though this work uses the FEA mesh to discretize the positions and vectors, in general, the division can be arbitrary.

With the discretization made in both the state and spatial spaces, the two point correlation function can be approximated by Equation (3.97) for a given $\boldsymbol{t}$, discrete state n, and discrete state p.

$$f_{\boldsymbol{t}}^{np} \approx \frac{1}{N(\boldsymbol{R})} \sum_{\boldsymbol{s}=\boldsymbol{0}}^{\boldsymbol{R}} d_{\boldsymbol{s}}^{n} d_{\boldsymbol{s}+\boldsymbol{t}}^{p} \tag{3.97}$$

Since the states considered in this work only includes the binary states of undamaged or damaged and a whole element takes on these states, $d_{\boldsymbol{s}}^{n}$ is simply 1 if the element at location $\boldsymbol{s}$ is of the state n and 0 otherwise, similarly for $d_{\boldsymbol{s}+\boldsymbol{t}}^{p}$.

In literature, fast Fourier transforms are used to compute the value of the two point correlation for domains of significant size [106], but since the domains considered in this work is relatively small, a simple summation will be used to evaluate the two-point correlation functions.

A three dimensional matrix, F_{ijk}^{np}, will be constructed from the values of two-

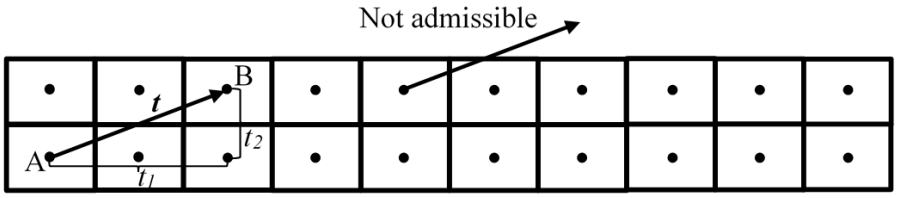

Figure III.8. Discretized domain used to evaluate the two-point correlation functions

point correlation functions, with the indices i, j, and k corresponding to the values of (t_1, t_2, t_3) respectively. For the case of uniaxial load, there will only be a single element in one of the dimensions, making $\boldsymbol{F}$ to be a two-dimensional matrix. The states n and p considered will only be the damaged state resulting the in $\boldsymbol{F}$ representing the damaged autocorrelation.

To quantify the difference between a damage state resulting from using method β and a damage state resulting from using method γ, let $\kappa_{\beta\gamma}$ represent a measure of the difference between the damage states. It is calculated by taking the L-2 norm of the difference between the damage autocorrelation matrices, $\boldsymbol{F}$, as shown in Equation (3.98).

$$\kappa_{\beta\gamma} = ||\boldsymbol{F}_\beta - \boldsymbol{F}_\gamma|| \tag{3.98}$$

Since some damage methods will use a higher refined mesh to evaluate the impact of mesh refinement on the predicted damage progression, an averaged autocorrelation matrix will be used, such that all the autocorrelation matrices have the same size, allowing methods using higher mesh refinement to be compared with methods using lower mesh refinement.

To illustrate the utility of two-point correlations, consider the example damage

states 1 and 2 as illustrated in Figure III.9, where the darker grey represents a 90° ply, the lighter grey represents a 0° ply aligned with the load direction, and the black elements represent damaged elements in the 90° ply.

For these two illustrative damage states, the two-point correlations offer a measure that differentiates between the two states by taking into account the location of damage. Using the two-point correlation methods described, $\boldsymbol{F}_1 - \boldsymbol{F}_2$ is plotted in Figure III.10 for the damage states 1 and 2, shown in Figure III.9. For all $\boldsymbol{t}$ vectors with a value of t_1 larger than the distance between cracks or a value of t_2 larger than the height of the lower ply, the autocorrelation functions are exactly zero since there is no chance to find damage. For the $\boldsymbol{t}$ vectors resulting in some points A and B near a crack, the probability to find damage is different between the two damage states, since the damage has different arrangements. The incorporation of the location and amount of damage in the laminate into the measure of the damage state offers the ability to differentiate between two damage states that measures not based on the location of damage fail to distinguish between.

(a) Damage state 1

(b) Damage state 2

Figure III.9. Example damage states

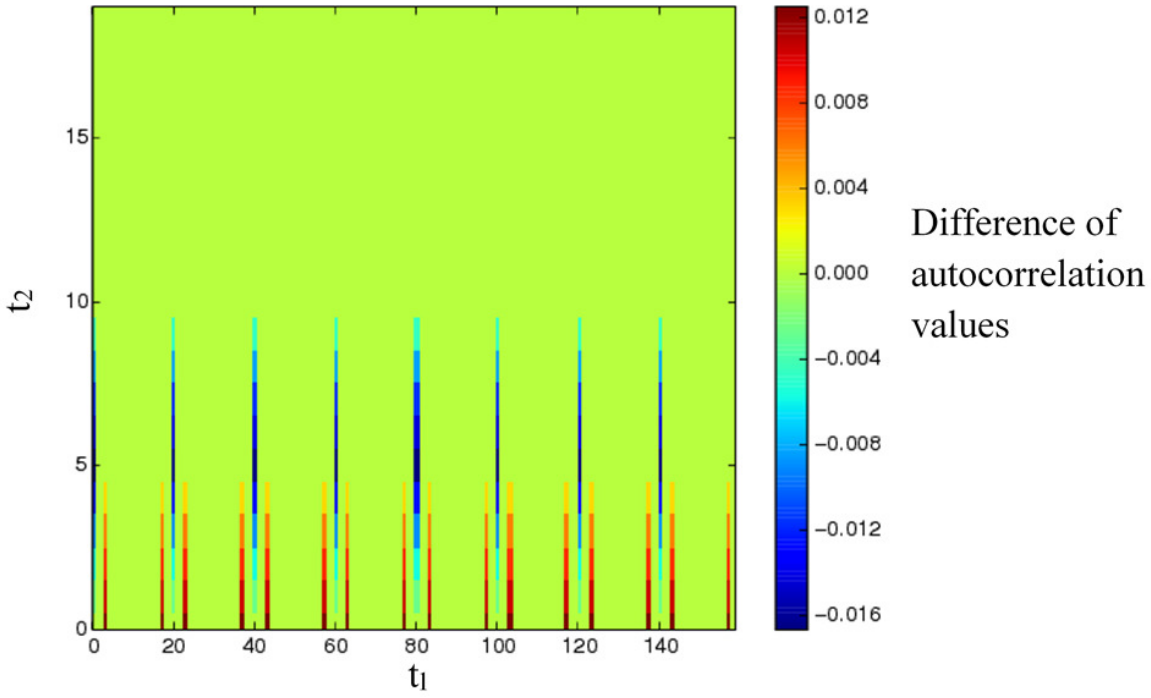

Figure III.10. Contour plot of the difference of F matrices for illustrative damage states 1 and 2

CHAPTER IV

RESULTS*

In this chapter, the results for the fiber property determination and damage model comparison are given. The chapter begins with the determination of graphite fiber properties. Before the comparison of the damage models, a convergence study is given using a cohesive zone model. Finally, the chapter ends with the comparison of damage models for a laminate under uniaxial tension and in-plane shear loads.

IV.A. Determination of Graphite Fiber Properties

The results for determining graphite fiber properties are presented in four parts. The effect of assuming the non-orthotropic terms to be zero in the compliance matrix is explored. Next, the choice of an RVE size and number of realizations is made based on the variation of the averaged lamina properties, the transverse isotropy of the average compliance matrix, and the standard deviation of the predicted lamina properties. The predicted properties for the graphite fibers are then presented. Finally, the results for a glass fiber material system are presented.

*Parts of this material, originally appeared in the ASC Proceedings, Volume 2013 (2014), published by DEStech Publications, Inc., Lancaster, PA, USA, and is reprinted here with permission of the publisher.

IV.A.1. Effect of Non-Orthotropic Terms

For the case of the random RVE, both methods of eliminating the non-orthotropic terms of the averaged compliance matrices result in approximately the same properties with every term in the resulting compliance matrices varying by less than 0.9%. Furthermore, the non-orthotropic terms of the averaged compliance matrices have little influence on the strain states. This was shown by multiplying the full compliance matrix with a stress state to obtain the strain and by multiplying the orthotropic compliance matrix with the same stress state to obtain the approximate strain. The strains differed by less than 0.2% for the compliance matrices determined in this study. Since the method has little effect on the results, either method is valid for the RVE sizes considered. However, it is possible that very small RVE sizes (e.g. less than 5 fibers) may result in significant differences. For this work, the non-orthotropic terms will be eliminated from the averaged compliance matrix due to the convenience of implementation.

IV.A.2. Determination of RVE Size and Realization Count

The distribution of each predicted lamina property depends on the RVE size and number of realizations. Consequently, before solving for the predicted fiber properties, an appropriate size for the randomly arranged RVE's and the number of realizations were determined. The choice of an appropriate size and number of realizations was based on the average lamina properties, a measure of the transverse isotropy, and the standard deviation of the lamina properties. The T650-35/PMR-15 material system was used in the study to determine the RVE size and realization

count.

IV.A.2.a. Average Lamina Properties

To accurately characterize the fiber properties, the average of the predicted lamina properties from all the realizations must be determined within an acceptable tolerance. For various RVE sizes, the average lamina properties were determined as a function of the number of realizations. Figure IV.1 shows a typical graph of the average predicted lamina properties as a function of the number of realizations for a 30 fiber RVE. The 60 and 100 fiber RVE's demonstrated similar behavior and are not shown. The average lamina properties were calculated using up to about 900 realizations for the 30 fiber RVE, 600 for the 60 fiber RVE, and 450 for the 100 fiber RVE. Fewer realizations are used for larger RVE sizes since it is expected that as the RVE size is increased, a smaller number of realizations will be required to accurately characterize the average value. The value predicted by the maximum realization count for a given RVE size is known as the reference value for this work. Comparing the reference values for different RVE sizes shows that the average predicted properties vary by less than 0.5% for the RVE sizes considered when many realizations are used. This indicates that the average lamina properties are not sensitive to RVE size for RVEs with at least 30 fibers. However, this may not be the case for very small RVE sizes (such as RVEs containing 2 or 3 fibers).

The particular realizations depend on the seed used for the random number generator that determined the initial placement of the fibers. To check whether the predicted average properties were overly sensitive to the particular seeding, the

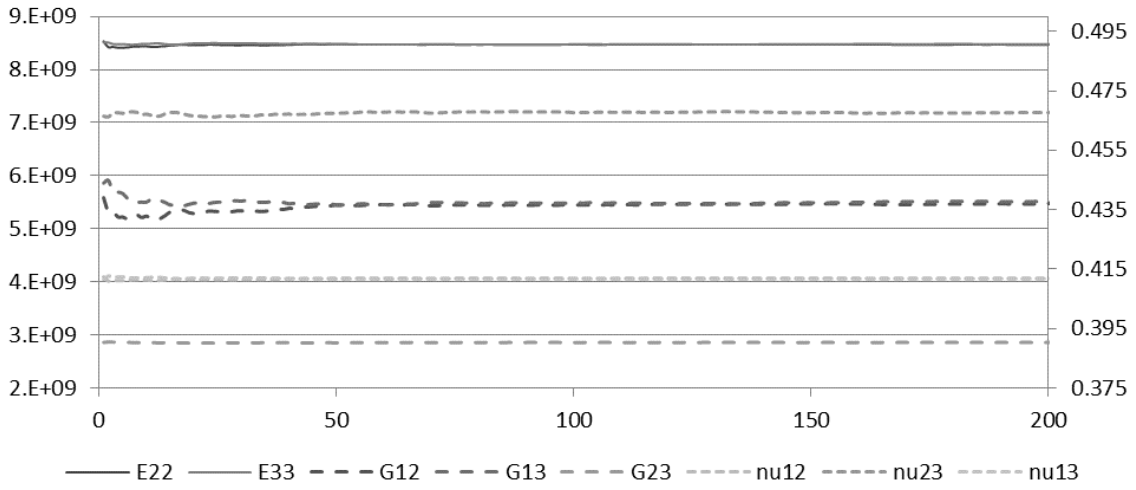

Figure IV.1. Average lamina properties for a given number of realizations (30 fiber RVE)

process was repeated for the 30 fiber case with a different seed for the random number generator, and the results did not change significantly. Figure IV.2 quantifies the variation of the average lamina properties for the 30 fiber RVE case shown in Figure IV.1. The averages shown in Figure IV.1 do not converge monotonically, which complicates the quantification of error in terms of the realization count. Instead of stating an error for a given realization count, it is better to identify the maximum error that occurs between N realizations and the maximum number of realizations. The error in this context was defined as the percent difference between the value predicted using a given number of realizations and the reference value. For an RVE size of 30 fibers, the average lamina properties do not vary more than 2% when at least 50 realizations are used. For an RVE size of 60 and 100 fibers, the variation was less than 2% for smaller realization counts (e.g. 30-50 realizations).

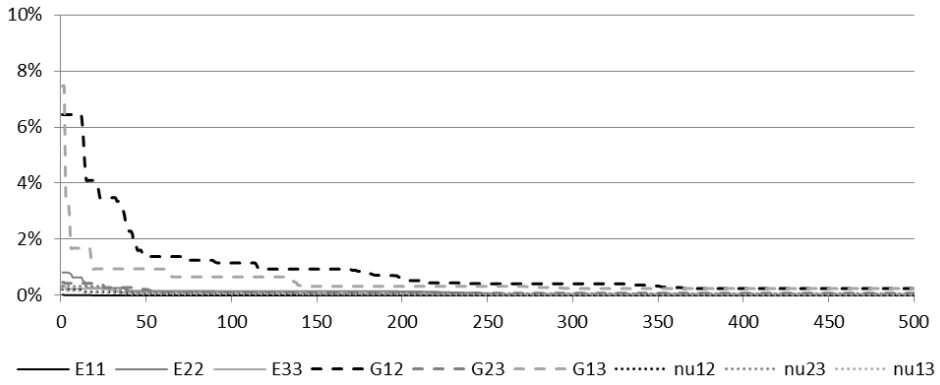

Figure IV.2. Maximum percent difference of average predicted lamina properties from reference (30 fiber RVE)

IV.A.2.b. Transverse Isotropy of Lamina Properties

The predicted lamina properties are assumed to be transversely isotropic. For a material to be considered transversely isotropic, the properties must not change when the compliance matrix is rotated about a single axis. In this case, the assumption means that transverse Young's moduli (E_2 and E_3) should be equal, the longitudinal shear moduli (G_{12} and G_{13}) should be equal, and the longitudinal Poisson ratios ($_{12}$ and $_{13}$) should be equal. In addition, G_{23} should follow the relation given in Eq. 4.1.

$$G_{23} = \frac{E_{22}}{2(1+\nu_{23})} \tag{4.1}$$

Figure IV.3 quantifies the percent difference between properties which should be equal if transverse isotropy holds. The difference is examined versus the number of realizations used to calculate the properties. The longitudinal shear moduli showed a much larger difference than the transverse shear moduli and longitudinal Poisson ratios. Interestingly, the percent difference between the transverse shear modulus

and the value calculated using the isotropic relation (see Eq. 4.1) did not converge towards zero as the number of realizations increased, but rather converged towards a non-zero value. However, the converged value decreased as the RVE size increased. This implies that transverse isotropy cannot be assured just by averaging many realizations but also requires a sufficiently large RVE size. The most likely reason for this is the square shape of the periodic RVE. Square arrays are fundamentally unable to yield transversely isotropic properties. The impact of the RVE's shape can be reduced to the point of being negligible by increasing its size, but it cannot be eliminated entirely. It should be possible to obtain transversely isotropic properties with different RVE shapes (e.g. hexagons), but the development of such a model is beyond the scope of this work. For the examined RVE sizes, the deviation of G_{23} from transverse isotropy is adequately small for the current investigation into fiber properties.

In order to obtain lamina properties that comply with the assumption of transverse isotropy within 1% (excluding G_{23}), about 200 realizations are required for 30 and 60 fiber RVE's, and about 50 realizations are required for 100 fiber RVE's.

IV.A.2.c. Standard Deviation of Lamina Properties

Accurately representing the distribution of lamina properties requires a sufficient number of realizations to determine both the average values of the properties as well as characterize the scatter in the properties. In the current study, the scatter is described using the standard deviation. The number of realizations to achieve an approximately constant standard deviation was shown to depend on the RVE

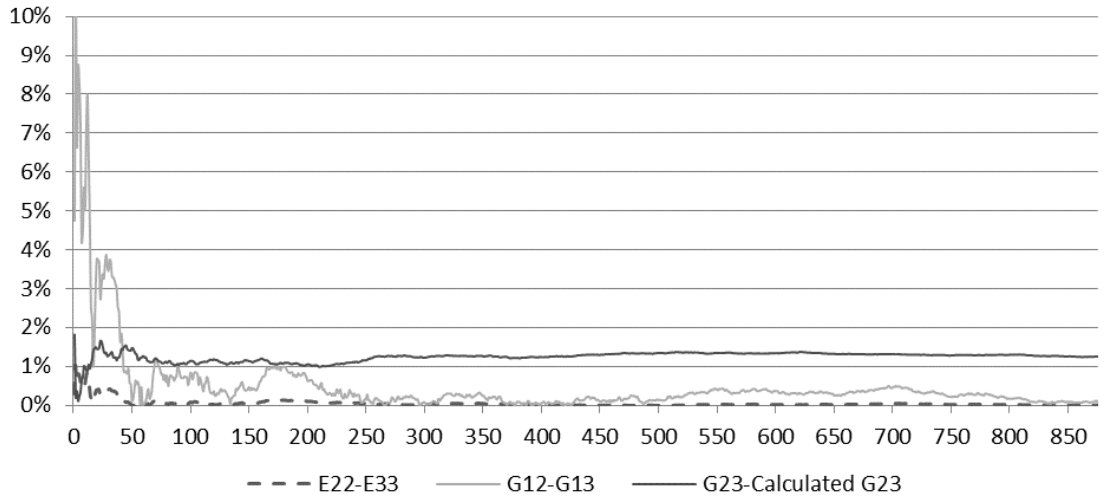

Figure IV.3. Percent difference of properties relevant to transverse isotropy (30 fiber RVE)

size, with more realizations needed for the smaller RVE sizes. Similar to Figure IV.2, Figure IV.4 quantifies the maximum difference of coefficient of variation (the standard deviation normalized by the mean) that occurs between N realizations and the maximum number of realizations for the 30 fiber RVE. Comparing the data for the RVE sizes, it was shown that the standard deviation decreases as the RVE size increases.

IV.A.2.d. Choice of RVE Size and Number of Realizations

For this work, it was chosen that 200 realizations for a RVE size of 30 fibers, 100 realizations for a RVE size of 60 fibers, and 50 realizations for a RVE size of 100 fibers would be an appropriate RVE size and realization count. Since the degrees of freedom in the FEA mesh increases with the fiber count, the lower fiber counts take less time to solve. Each RVE size was timed for many realizations.

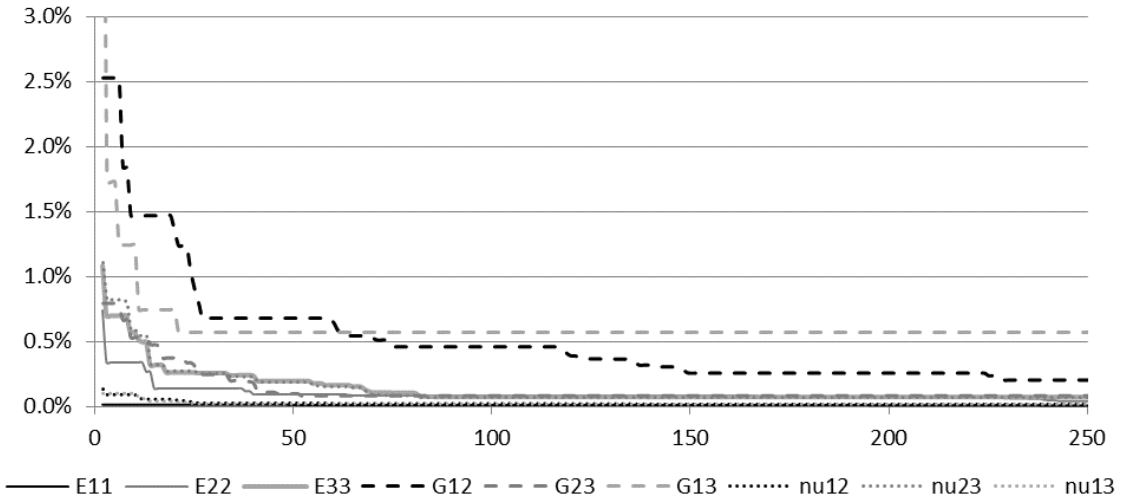

Figure IV.4. Maximum difference of coefficient of variation from reference value (30 fiber RVE)

The average time multiplied with the number of realizations for the respective size showed that all three combinations of RVE sizes and number of realizations require similar computation time. However, timings of FEA solutions are very dependent on the system and software used, so this behavior is only valid for this work. With the similar computation cost, the larger RVE size was chosen, since it exhibits more transversely isotropic behavior.

IV.A.3. Predicted Graphite Fiber Properties

Tables IV.1 to IV.3 show the predicted fiber properties for the graphite fiber material systems using a hexagonal fiber arrangement, random fiber arrangement, and the Mori-Tanaka averaging scheme. As previously discussed, reported lamina properties generally present a dilemma in choosing whether to use the reported volume fraction or the volume fraction calculated from lamina properties and the manu-

facturer's longitudinal fiber properties. As a result, the properties were calculated for both volume fractions when available. Some sources did not report a volume fraction, requiring its calculation using rule of mixtures.. It was found that most properties are similar between the methods with the exception of the longitudinal shear modulus. The longitudinal shear modulus showed a higher sensitivity to the volume fraction for the Mori-Tanaka averaging scheme and hexagonal RVE than the random RVE, as seen in Table IV.2 and Table IV.3.

During this study, some material systems resulted in negative or infinite longitudinal shear moduli for the hexagonal unit cell and Mori-Tanaka averaging scheme. For these models, even rigid fibers will not yield a sufficient lamina shear modulus. This is due to the reduced interaction between fibers for the hexagonal array and Mori-Tanaka averaging scheme as compared to the random fiber model.

The IM7 properties obtained using the two different material systems showed significant differences, especially with the longitudinal shear modulus. The difference in resulting properties could be due to error in the material system properties reported by the literature or due to differences in the actual fiber properties between the composite systems.

Table IV.4 shows the values reported by literature for the fiber properties. These numbers are based on the reported volume fraction, if one was reported. It appears that the method used to predict the fiber properties for IM7 using the IM7/5250-3 material system had the same issue with the longitudinal shear modulus that FEA with a hexagonal RVE and the Mori-Tanaka averaging scheme encountered. With the exception of the longitudinal shear modulus, the values predicted using FEA with a

Table IV.1. Predicted fiber properties for IM7 and AS4 graphite fibers

	IM7 (5250-4)	**IM7 (8552)**			**AS4**	
	Calc. Vf	**Calc. Vf**			**Calc. Vf**	**Rep. Vf**
	Random	*Mori-Tanaka*	*Hex*	*Random*	*Random*	*Random*
E_1 (GPa)	276	276	276	276	231	207
E_2 (GPa)	26	26.5	24.9	22.4	29.9	22.6
G_{12} (GPa)	20.7	19.6	19.3	12	32.2	20.6
G_{23} (GPa)	7.55	9.07	8.33	7.53	12.13	8.96
ν_{12}	0.292	0.272	0.303	0.274	0.244	0.251

Table IV.2. Predicted fiber properties for T300 graphite fibers

	T300					
	Calculated Vf			**Reported Vf**		
	Mori-Tanaka	*Hex*	*Random*	*Mori-Tanaka*	*Hex*	*Random*
E_1 (GPa)	230	230	230	227	227	227
E_2 (GPa)	33.5	29.4	24.3	31.8	28.2	23.4
G_{12} (GPa)	99.9	91.5	16	71.4	66.7	15.2
G_{23} (GPa)	15.14	12.12	9.9	14.13	11.5	9.6
ν_{12}	0.24	0.24	0.244	0.241	0.241	0.246

Table IV.3. Predicted fiber properties for T650-35 graphite fibers

	T650-35					
	Calculated Vf			**Reported Vf**		
	Mori-Tanaka	*Hex*	*Random*	*Mori-Tanaka*	*Hex*	*Random*
E_1 (GPa)	243	243	243	225	225	225
E_2 (GPa)	18	17.2	16	15.4	14.9	14.2
G_{12} (GPa)	49.7	48.8	13.7	21.1	20.9	11
G_{23} (GPa)	7.04	6.59	6.07	5.84	5.55	5.28
ν_{12}	0.444	0.443	0.442	0.439	0.438	0.437

random RVE were less than 6% different from the values in Ref. [11]. The properties for the AS4 and T300 fibers in literature were said to be assumed without an explanation of the method used to obtain them (fiber property determination was not the aim of the paper that reports these properties). The AS4 and T300 properties predicted using FEA with a random RVE differed from the reported values by 8-45%. The T650-35 properties from Ref. [10] were determined using the Mori-Tanaka averaging scheme, which matches the properties calculated in this work using the same method. The properties for T650-35 predicted using FEA with a random RVE differed from the reported values by less than 10% for all properties except the longitudinal shear modulus, which was 62% smaller for the random RVE. These comparisons to between models and results published in literature indicate that the predictions of the fiber's Young's moduli, Poisson's ratios, and transverse shear modulus are somewhat insensitive to the assumed microstructure, but the predicted longitudinal shear modulus exhibits large differences between microstructures. This highlights the importance of consistently using the same microstructure to predict fiber properties and model the microstructural behavior of composite systems.

Due to the large differences in the predicted longitudinal shear modulus for the microstructural models, the effect of spacing between fibers was investigated to understand the cause of the difference. For the material system of T650-35/PMR-15 with a volume fraction of 0.556, the minimum spacing fraction can theoretically vary from 0, which allows fibers to touch, to 0.554, which corresponds to hexagonal packing. For RVE's with 100 fibers, the algorithm used to generate the random RVE's cannot achieve volume fractions higher than about 83%. Consequently, the

Table IV.4. Fiber properties reported by the literature

	IM7 (5250-4) [4]	**AS4 [102]**	**T300 [102]**	**T650-35 [2]**
E_1 (GPa)	276	225	230	225
E_2 (GPa)	27.6	15	15	15.4
G_{12} (GPa)	138	15	15	21.1
G_{23} (GPa)	7.67	7	7	5.8
ν_{12}	0.3	0.2	0.2	0.44

random RVE generation can only achieve a minimum spacing fraction between 0 and about 0.4 (See Eq. 3.53 with $V_f = 0.556$ and $V_f^{'} = 0.83$).

Figure IV.5 shows the variation of the predicted fiber properties as a function of the minimum spacing fraction. The longitudinal Young's modulus, E_1, and longitudinal Poisson's ratio, $_{12}$, were omitted since they varied by less than 0.3%. For all minimum spacing fractions considered, the transverse Young's modulus, E_2, and transverse shear modulus, G_{23}, varied by less than 5%. The longitudinal shear modulus, G_{12}, was significantly affected by the spacing, increasing by 90%.

As the minimum spacing fraction is increased, the random microstructure becomes more uniform and forms fewer networks of fibers. As a result, the resulting lamina properties decrease with the spacing, causing the fiber properties needed to match the experimental lamina properties to increase with the spacing. This relationship helps to explain the significant difference between the properties predicted using a hexagonal microstructure and the random microstructure.

IV.A.4. Predicted Isotropic Fiber Properties

To validate the developed method, an epoxy matrix, glass fiber material system was analyzed. The fiber properties of glass was expected to be isotropic with

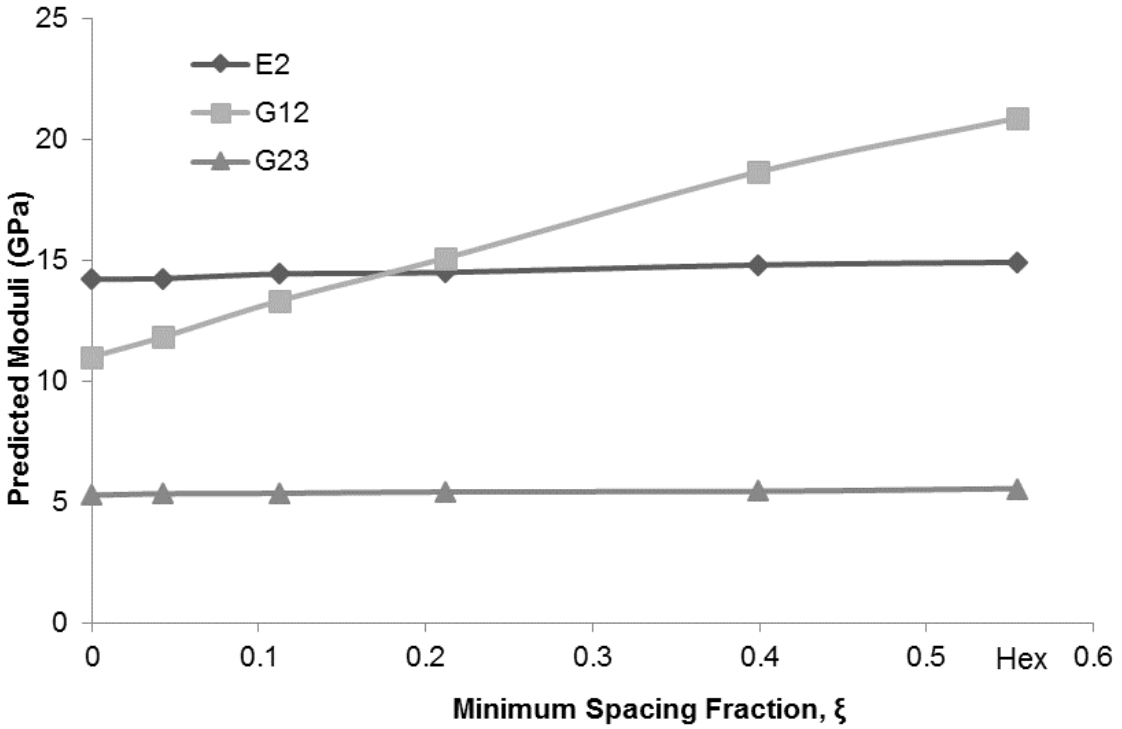

Figure IV.5. Predicted transverse Young's modulus and both shear moduli for fiber as a function of the minimum spacing fraction of the microstructure for T650-35 fibers

a Young's modulus 80 GPa for the Young's modulus and 0.2 for the Poisson ratio [102]. Only enforcing transverse isotropy for the fibers using the procedure previously described with a random microstructure does not result in isotropic predicted properties, as seen in Table IV.5. Similar to the problem found for some graphite fibers, the properties predicted using a hexagonal RVE and the Mori-Tanaka averaging scheme resulted in negative or infinite transverse Young's and shear moduli. For these models, even rigid fibers will not yield sufficient lamina transverse moduli.

Enforcing isotropy of the fibers modifies the algorithm to have more outputs (5 lamina properties) than inputs (2 fiber properties). As a result, solving for the

Table IV.5. E-Glass 21xK43 predicted fiber properties using random RVE's

E_1 (GPa)	80
E_2 (GPa)	63
G_{12} (GPa)	15.4
G_{23} (GPa)	25.8
ν_{12}	0.258

correction term for the next iterative guess for fiber properties requires a least squares solution, making the method a modified Gauss-Newton algorithm. It is assumed that in general there is no guarantee that there exists a solution within tolerance when isotropy is enforced. The iterations are stopped when the residual fails to decrease. Effectively, this method finds the local minimum of the function space for the norm of the residual vector.

Again, several homogenization methods were used when forcing the glass fibers to be isotropic, including the Mori-Tanaka averaging scheme, FEA with the hex microstructure, and FEA with the random RVE microstructure. Table IV.6 shows the resulting properties. The Mori-Tanaka averaging scheme predicted the closest values to the literature reported values of the Young's modulus and Poisson's ratio, and the hexagonal RVE was the closest to the reported value for the shear modulus. However, no two methods varied by no more than 7%. The predicted Poisson's ratio for all three methods was quite a bit larger than the value reported by the literature. Compared to the properties predicted for transversely isotropic fiber material systems, the properties predicted for the isotropic fiber material system showed much less sensitivity to the model used.

Table IV.6. E Glass 21xK43 fiber predicted properties forcing isotropy

	Mori-Tanaka	Hex	Random	Literature [102]
E (GPa)	79.7	81.5	79	80
G (GPa)	32.1	32.6	31.4	33.3
ν	0.242	0.251	0.26	0.2

IV.B. Cohesive Zone Convergence Investigation

During the validation of the cohesive zone model, a double cantilevered beam (DCB) was considered without a precrack along the interface. Unexpectedly, the analysis failed to converge on the first load step. As a result, the convergence behavior of the cohesive zones under normal opening was investigated. Fortunately, since the elements at the end are undergoing a purely normal displacement, the problem can be reduced to only one dimension. As a results, the 1D problem considered consists of a single cohesive zone element between two continuum elasticity elements, as illustrated in Figure IV.6. Note that this investigation is valid for both 2D and 3D for elements undergoing only mode I opening.

A specified displacement is applied, since a specifying a force only leads to a solution in the linear regime of the cohesive zone opening or an unstable problem that will never reduce the residual to zero. For this 1D study, the relevant parameters are given in Table IV.7.

For an applied displacement, U, on the upper face, the opening of the cohesive zone can vary from 0 to U, where U would result in complete opening of the cohesive zone and undeformed continuum elements. For every Δ_n, the traction required to satisfy equilibrium can be directly solved for this simple problem. Similarly, the traction provided by the cohesive zone can be plotted for a separation of 0 to U. The

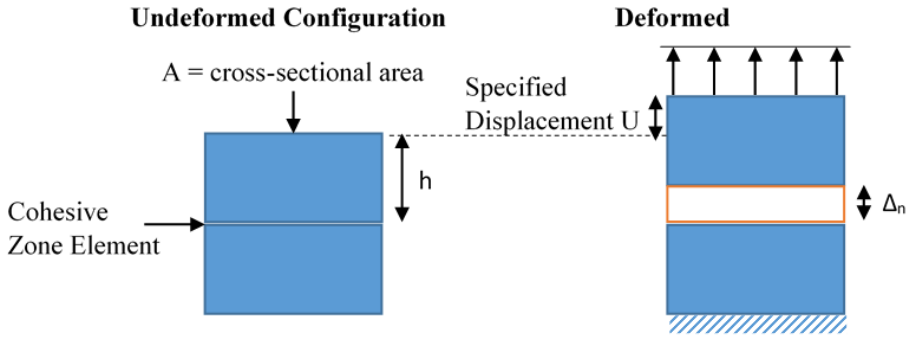

Figure IV.6. Problem description for 1D cohesive zone investigation

residual created by the mismatch between the traction provided by the cohesive zone and the traction required to satisfy equilibrium can be calculated as the difference between the two traction plots and will be useful to gain some insight into the behavior of the various numerical methods.

Three cases will be considered for this study: unstable opening, opening resulting in damage, and opening right at the critical traction. These cases represent many of the situations that will occur in an analysis using a cohesive zone model.

IV.B.1. Case 1: $U = 2e\text{-}5 > \Delta_f$ and $h = 1e\text{-}2$

This case is representative of a cohesive zone undergoing sudden complete opening, which can occur if cohesive zone with a high strength opens next to a cohesive zone with a lower strength, a high load is applied near the cohesive zone, or a unstable damage growth.

It is important to note that the very small height of the continuum elements results in a large stiffness contribution. For small values of Δ_n, the continuum

Table IV.7. Parameters used for convergence investigation

Continuum Element Properties	
E	70e9 Pa
Cohesive Zone Properties	
$K_{penalty}$	7e13 Pa
G_{Icrit}	100 J/m^2
t_{Ncrit}	50e6 Pa
$delta_{n0}$	7.143e-7 m
$delta_{nf}$	4e-6 m
Geometric Parameters	
A	1 m^2

elements are picking up a larger portion of the deformation, and since the continuum elements are very stiff, a high traction is needed by the cohesive zone to satisfy equilibrium. However, the traction is too high for all values of Δ_n except $\Delta_n = U$, where the traction is zero to satisfy equilibrium and the cohesive zones pick up all of the deformation imposed by the boundary condition, as shown in Figure IV.7.

The only solution to this problem is the cohesive zone is fully damaged, $d = 1$. The residual is plotted in Figure IV.8, which shows a local minimum at the separation corresponding to the initiation of damage in the cohesive zone, $\Delta_n = \Delta 0$.

The progression of solutions using the direct method are shown in Figure IV.9. The direct method required five iterations, most of which were iterating along the damage regime of the cohesive zone traction separation curve, but once the cohesive

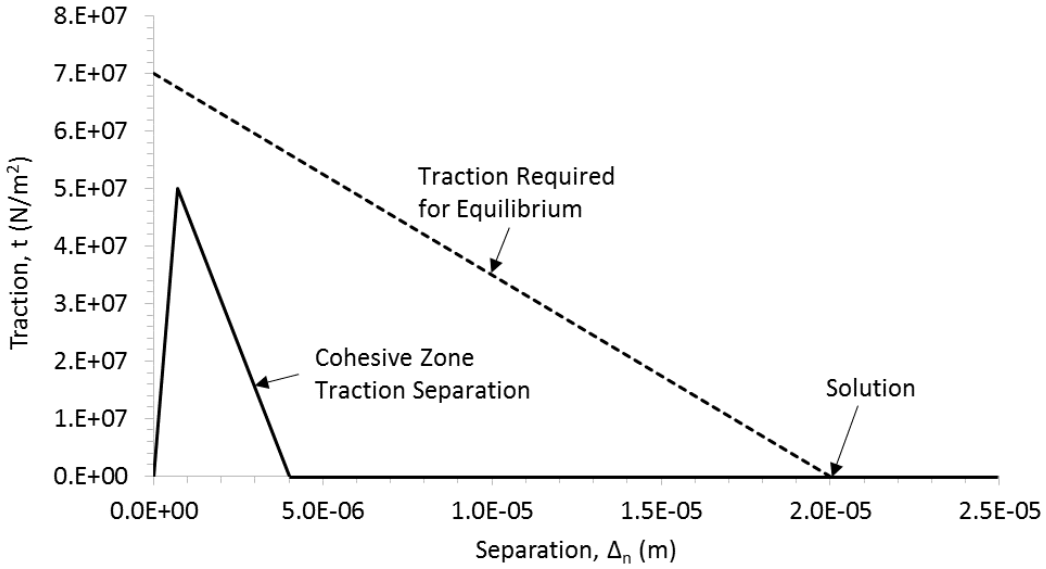

Figure IV.7. Traction separation curve for case 1

zone was opened, the solution was found in a single successive iteration. It is also interesting to note that the residual for this method increased with each iteration until the last iteration, whcih resulted in the residual being zero. This increasing behavior in the residual can pose some difficulties since the change in residual cannot easily be used to know if the iterations are going in the correct direction.

The progression of solutions obtained using the Newton-Raphson method are shown in Figure IV.10. The local minimum in the residual curve, see Figure IV.8, poses a significant issue for the tangent method since the solution will follow the tangent of the residual curve as it tries to find the root of the function. Using the tangent of the residual curve, the predicted opening for the linear regime of the cohesive zone traction separation curve ($\Delta_n < \Delta_0$) is 9.52e-7 m.

The next iteration then starts in the damage regime of the cohesive zone ($\Delta_0 < \Delta_n < \Delta_f$) and predicts the opening should be -7.79e-7 m. The negative opening puts

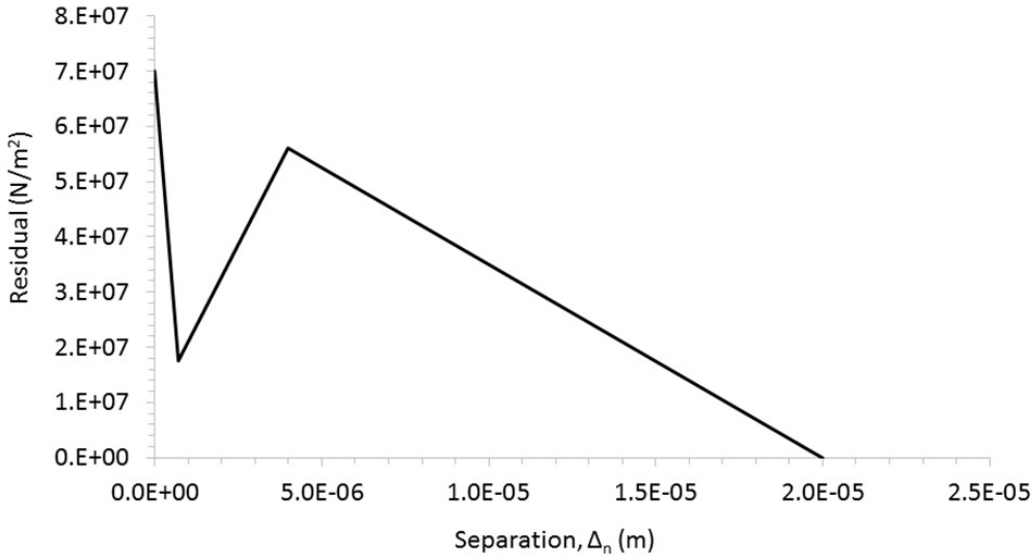

Figure IV.8. Residual for case 1

the solution back into the linear regime of the cohesive zone and the cycle continues. The progression of solutions enters an oscillation between two values as it oscillates between the two side of the local minimum. If the solution could get out of the local minimum region, $\Delta_n > \Delta_f$, the correct solution would be obtained in a single successive iteration.

A mix between the tangent and secant stiffness matrix can be used to approximate the tangent matrix to circumvent the oscillation issue faced by the Newton-Raphson method. Effectively, a mix of stiffness matrices attempts to give enough secant stiffness to get out of the local minimum region, while not too much to significantly reduce the convergence rate of the tangent stiffness. Unfortunately, a small number of mix ratios successfully resulted in the correct converged solution. Let the mix ratio, α, be the percent tangent stiffness, $\boldsymbol{T}$, used, with the remaining percentage being the secant stiffness, $\boldsymbol{K}$, as given in Equation (4.2).

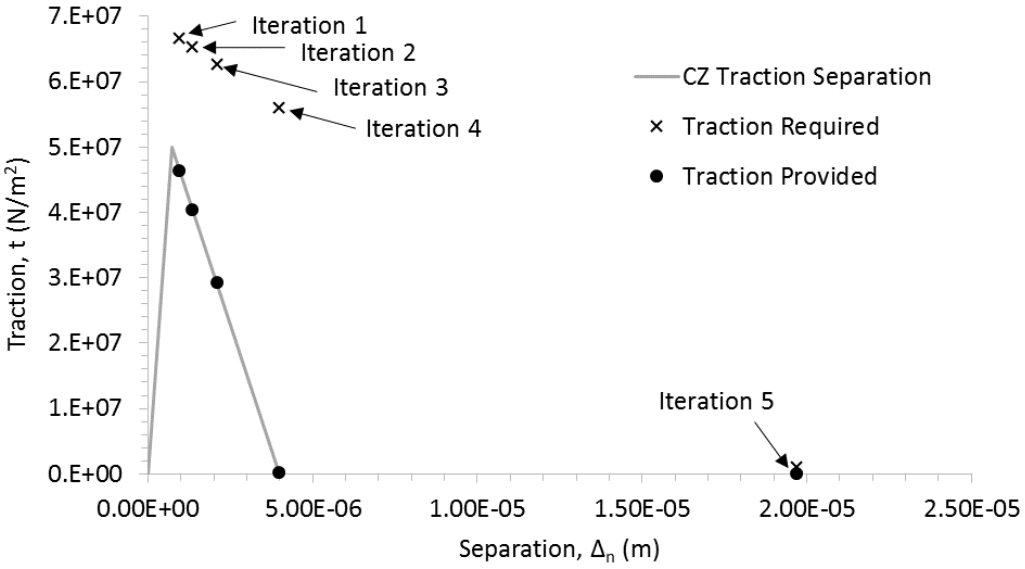

Figure IV.9. Solution progression using the direct method for case 1

$$\hat{T}_{ij} = \alpha T_{ij} + (1 - \alpha) K_{ij} \tag{4.2}$$

Mix ratios of 0.6, 0.7, and 0.9 did not converge and resulted in the same oscillatory behavior of the pure tangent method. However, a mix ratio of 0.8 was found to guide the solution out of the local minimum region, and the converged solution required only a single successive iteration, as shown in Figure IV.11.

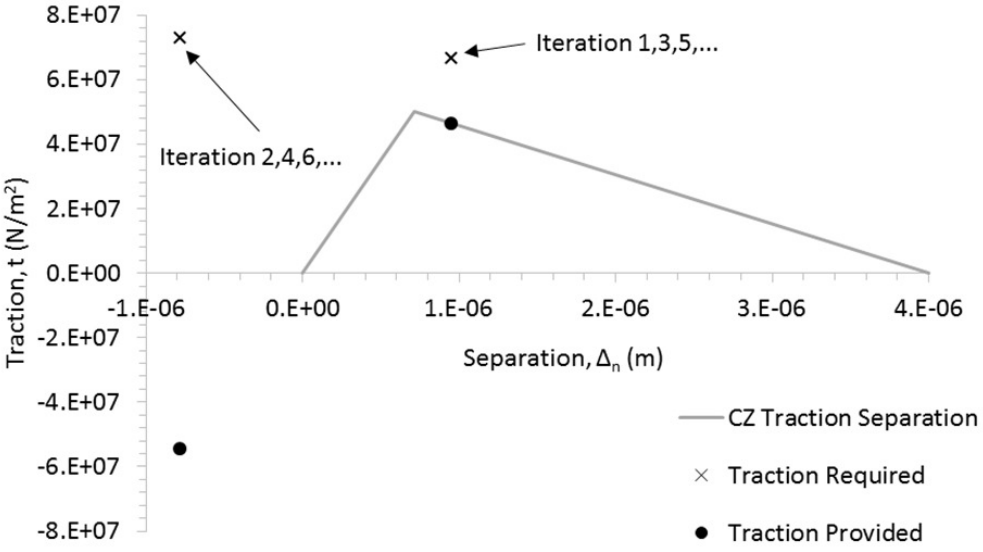

Figure IV.10. Solution progression using the Newton-Raphson method for case 1

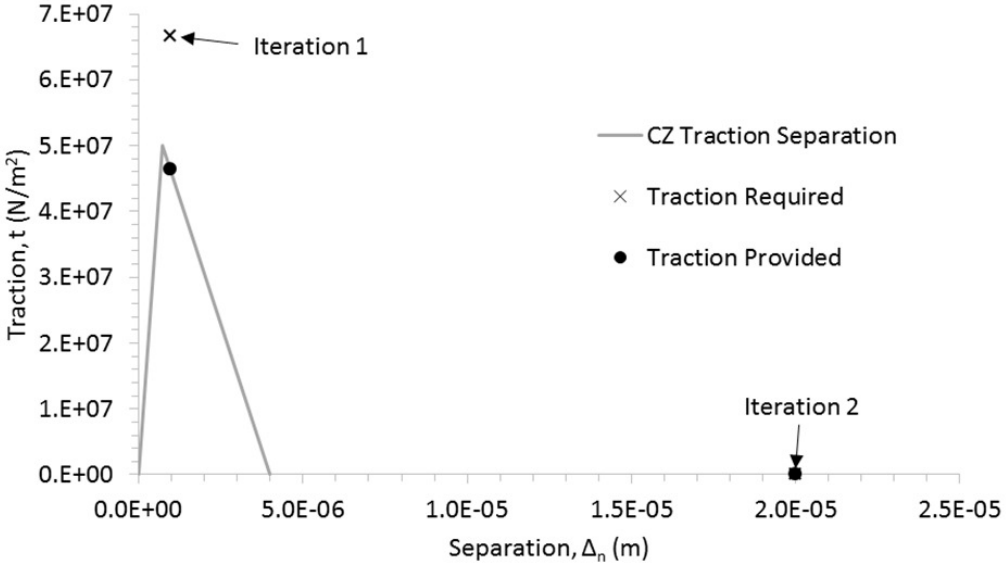

Figure IV.11. Solution progression using the mixed tangent-secant method for case 1

IV.B.2. Case 2: $\Delta_0 < U = 2.5e\text{-}6 < \Delta_f$ *and* $h = 1e\text{-}3$

This case is representative of cohesive zone undergoing partial damage, which occurs frequently throughout an analysis with a cohesive zone model.

The very high stiffness of the continuum elements, due to the very small value of h, and the specified displacement being in the damage regime of the of cohesive zone traction-separation curve leads the only solution to exist in the damage regime, as shown in Figure IV.12. The residual for this problem changes slope at $\Delta_n = \Delta_0$, but decreases monotonically as a function of the separation, which is shown in Figure IV.13.

The direct method showed a lower convergence rate than in Case 1, requiring a much higher number of iterations and approached the correct solution asymptotically, as shown in Figure IV.14.

The Newton-Raphson method using the pure tangent matrix showed a very fast convergence behavior, as seen in Figure IV.15. Using the residual in Figure IV.13, the first solution is predicted using the slope of the first section, $\Delta_n < \Delta_0$, and the converged solution is then obtained using the slope of the second section, $\Delta_n > \Delta_0$. Using the Newton-Raphson method but approximating the tangent matrix with a mix of the tangent and secant resulted in a convergence behavior somewhere between the direct and tangent method as a function of the mix ratio, α.

All mix ratios converged successfully, and the solution progression using a mix ratio of 0.8 is shown in Figure IV.16. Unlike Case 1, the residual for all methods decreases monotonically to zero as the solution progresses.

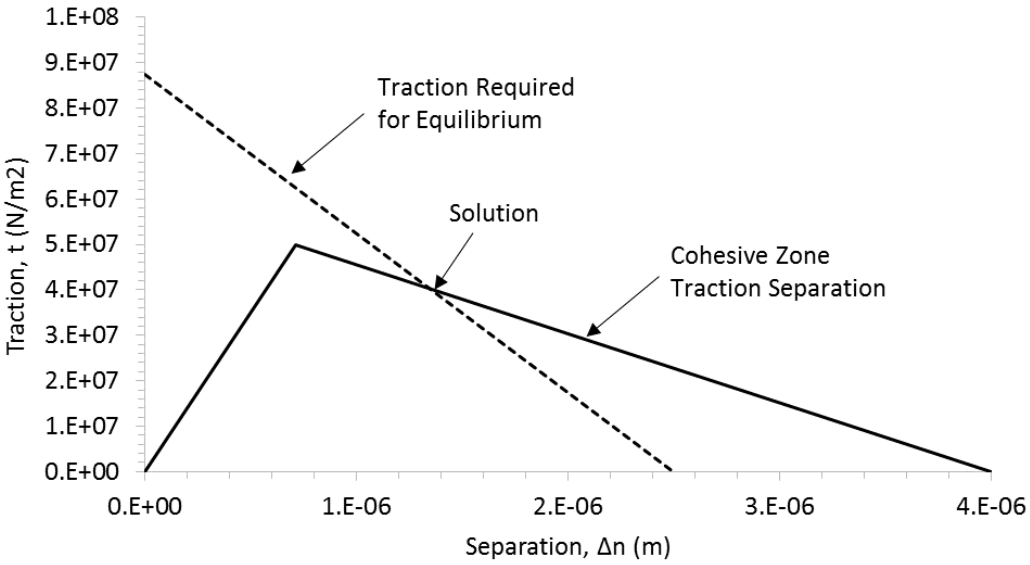

Figure IV.12. Traction separation curve for case 2

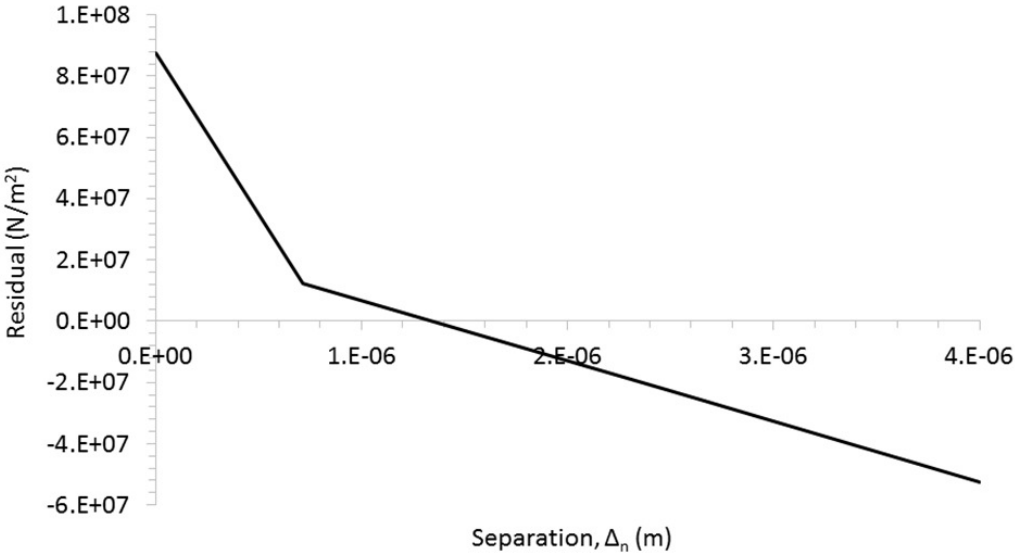

Figure IV.13. Residual for case 2

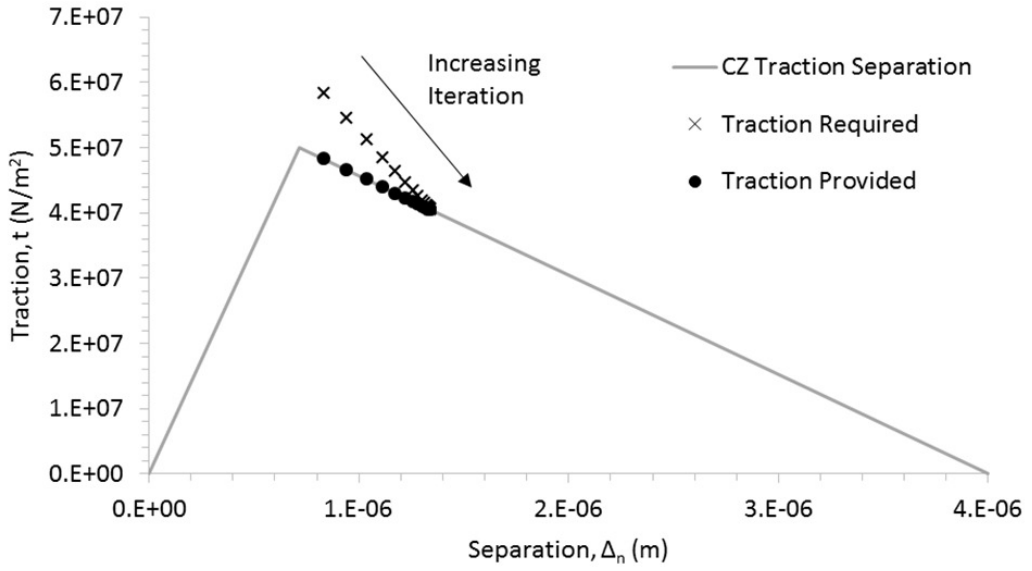

Figure IV.14. Solution progression using the direct method for case 2

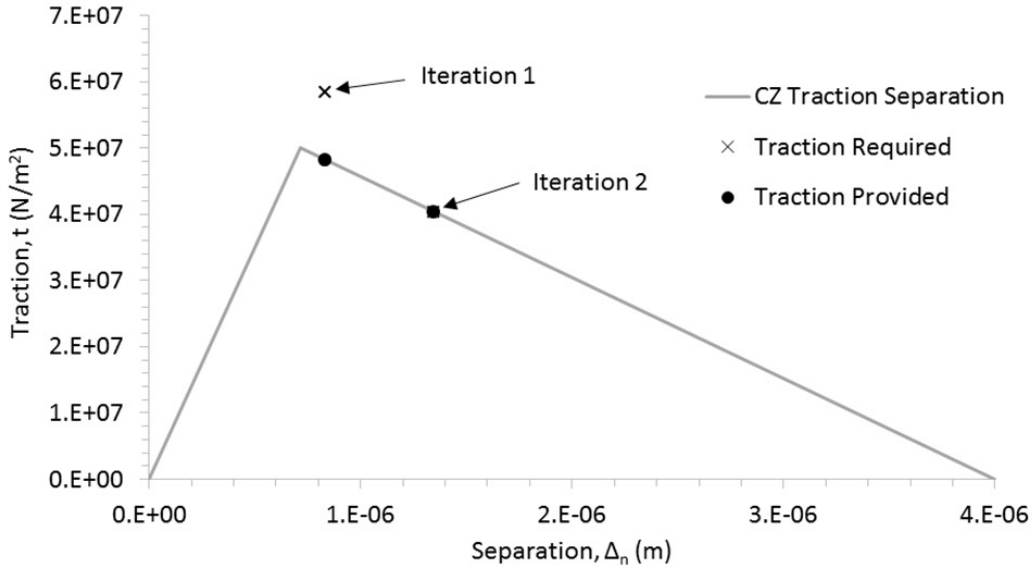

Figure IV.15. Solution progression using the Newton-Raphson method for case 2

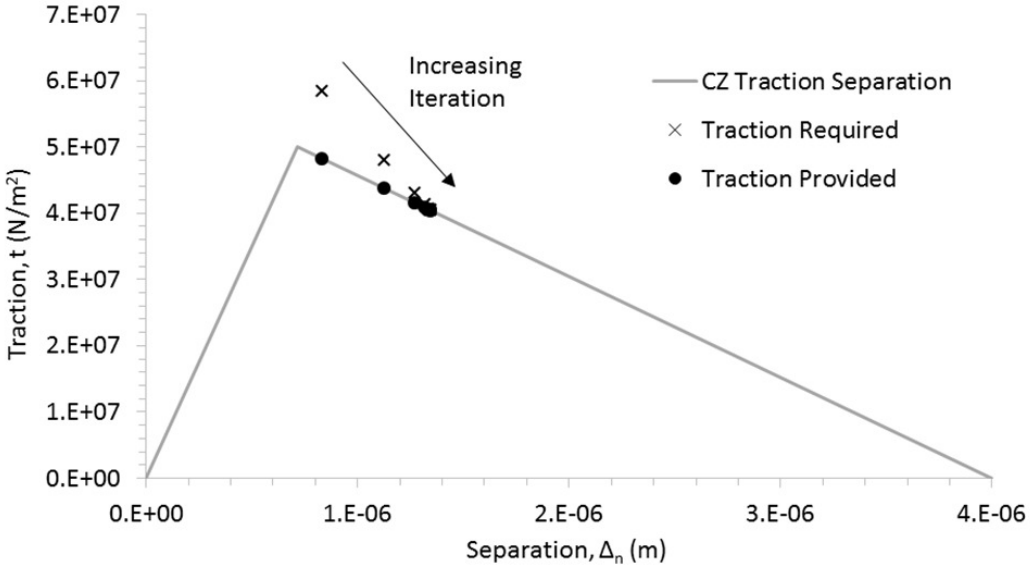

Figure IV.16. Solution progression using the mixed tangent-secant method for case 2

IV.B.3. Case 3: Solution is at Δ_0 ($U = 7e\text{-}6$ and $h = 4.4e\text{-}3$)

This case is representative of a cohesive opening right up to the critical limit where any further opening results in damage.

The applied displacement and thickness of continuum elements were chosen such that a solution exists at $\Delta_n = \Delta_0$, see Figure IV.17. The residual is plotted in Figure IV.18, which shows a zero at the separation corresponding to the initiation of damage in the cohesive zone, $\Delta_n = \Delta 0$, and another zero at $\Delta_n = U$.

As expected, all methods converged in only one iteration since the problem is linear for the first solution. However, this case shows that multiple solutions can exist for cohesive zone problems due to the negative slope of the damage regime. In problems with many cohesive zones interacting, the residual can be become quite complex and numerical techniques can overshoot a solution and find a different solution rather than converging back to the expected first solution.

IV.B.4. Penalty Stiffness Numerical Limits

During the investigation, the penalty stiffness was varied, leading to some unexpected results. The Newton-Raphson method with the exact tangent matrix always converges in a low number of iterations when the penalty stiffness is too low, which can be misleading since the converged solution will always require the cohesive zone to be either in the linear regime or completely damaged. This behavior was observed because if the penalty stiffness is too low, the traction separation curve can become skewed such that the opening to initiate damage is greater than the final opening, $\Delta_0 > \Delta_f$, refer to Figure III.5. This results in a non-physical traction separation

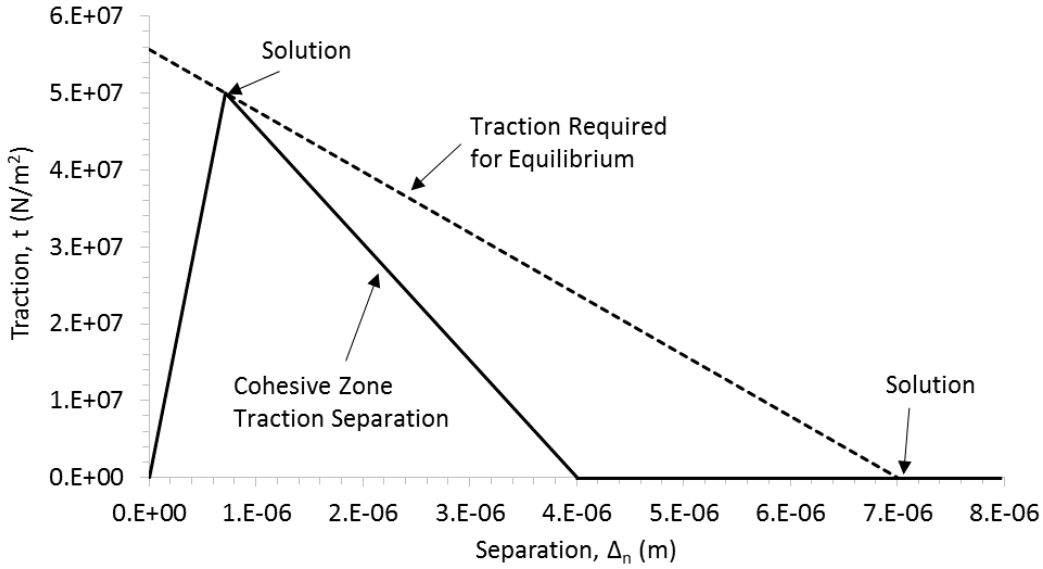

Figure IV.17. Traction separation curve for case 3

law.

Using the formulation of the cohesive zone, lower bounds for the penalty stiffness can be found as a function of the critical traction in each mode and critical strain energy release rates, which shown in Equation (4.3).

$$\begin{aligned} K_{penalty} &> \frac{t_{nc}^2}{2G_{Ic}} \\ K_{penalty} &> \frac{t_{tc}^2}{2G_{IIc}} \end{aligned} \tag{4.3}$$

Concerning the upper numerical bound, the numerical precision of the code is the limit on the penalty stiffness. For the double precision used in this work, a value of 1e23 was found to be the value for the penalty stiffness for which the methods began to suffer convergence issues due to round off error. For penalty stiffnesses higher than 1e23, the methods would sometimes no longer converge to any solution even if the solution lies in the linear regime of the cohesive zone traction separation

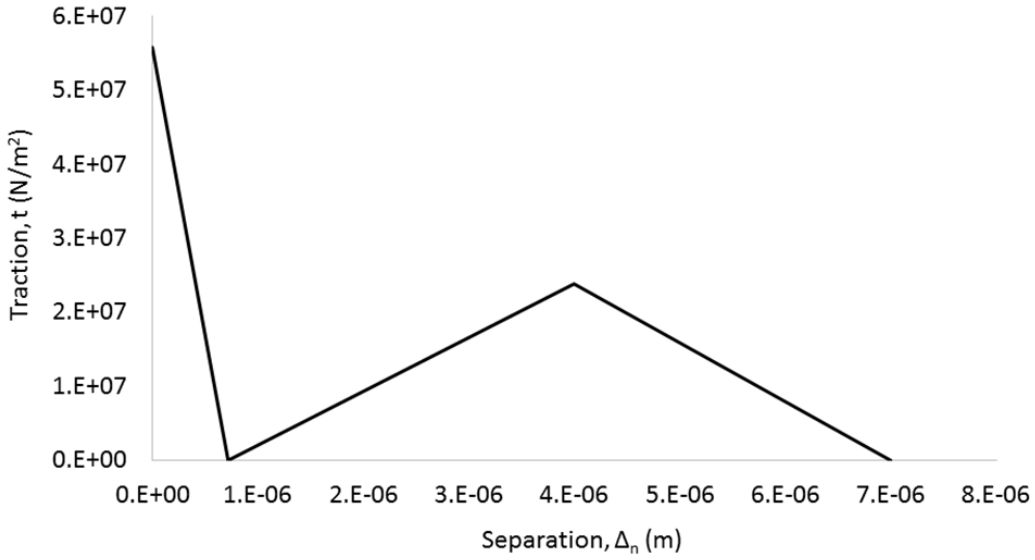

Figure IV.18. Residual for case 3

curves. The penalty stiffness still has bounds regarding to the solution accuracy, since the value of the penalty stiffness introduces artificial compliance into the interface before damage occurs, but the bounds developed in this section limit the numerical implementation of a penalty stiffness in cohesive elements.

IV.B.5. Convergence Summary

The Newton-Raphson method using the exact tangent matrix offers better convergence behavior than the other methods when the residual function has no local minimums that lead to an oscillatory convergence behavior. The direct method suffers from an asymptotic convergence behavior when the solution lies on the damage regime of the traction-separation curve, but when equilibrium requires full opening of the cohesive zone, the method offers a more reliable, faster convergence rate compared to the other methods considered. Mixing the tangent and secant can

be extremely effective if the mix ratio is carefully selected for the problem, but an appropriate ratio seems to depend on the problem, which poses some issues in a general framework. Also, there are physical lower bounds for the penalty stiffness as expressed in Equation (4.3).

IV.C. Comparison of Damage Models

In this section, a comparison of the damage models is presented. To begin, the boundary conditions and material properties used for the analyses are given. Next, the results for uniaxial load configuration are shown, followed by the results for the in-plane share load configuration.

IV.C.1. Boundary Conditions

A periodic section of the top half of the $[0/90]_s$ laminate is modeled, as illustrated in Figure IV.19. For the case of uniaxial load, the load is applied along the x_1-axis, and L is much larger than w. For the shear load case, the load is applied in the $x_1 - x_2$ plane, and L is equal to w. The domain is assumed to be periodic in the plane of the laminate, leading to the boundary conditions in Equation (4.4) and Equation (4.5), where u_i is the i^{th} component of the displacement vector and other dimensions are from Figure IV.19.

$$u_i\left(\frac{L}{2}, x_2, x_3\right) = u_i\left(-\frac{L}{2}, x_2, x_3\right) + \left\langle \frac{\partial u_i}{\partial x_1} \right\rangle \cdot L \tag{4.4}$$

$$u_i\left(x_1, \frac{w}{2}, x_3\right) = u_i\left(x_1, -\frac{w}{2}, x_3\right) + \left\langle \frac{\partial u_i}{\partial x_2} \right\rangle \cdot w \tag{4.5}$$

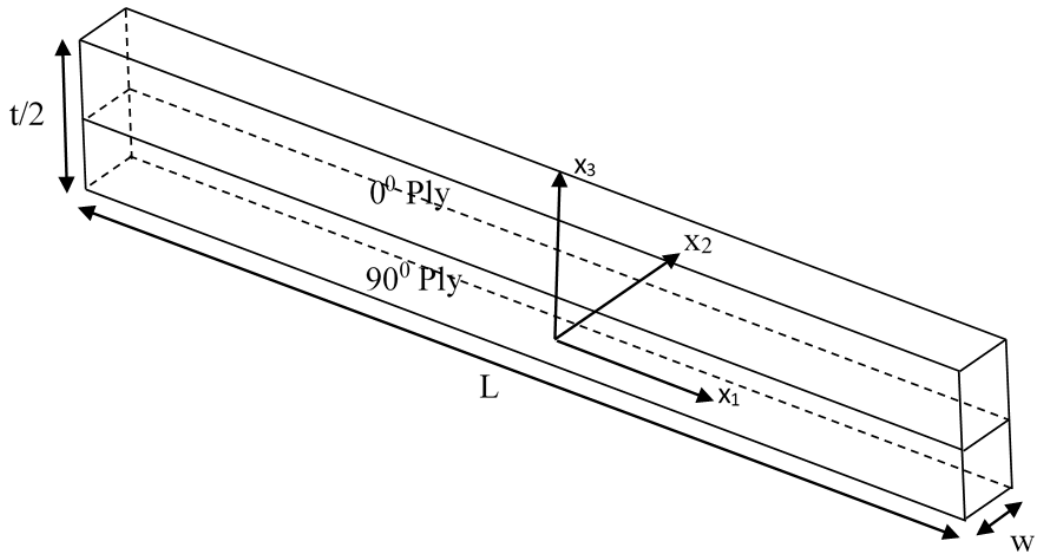

Figure IV.19. Illustration of computational domain and dimensions (Not to scale for the shear load case)

The symmetric boundary condition on the bottom of the domain and free boundary condition on the top of the domain are described by Equation (4.6). To prevent rigid body translation and rigid body rotation, the conditions expressed in Equation (4.7) are applied. A volume average uniaxial strain is applied by specifying $\left\langle \frac{\partial u_1}{\partial x_1} \right\rangle$.

$$\begin{aligned} &T_1\left(x_1, x_2, 0\right) = T_2\left(x_1, x_2, 0\right) = 0 \\ &u_3\left(x_1, x_2, 0\right) = 0 \\ &T_i\left(x_1, x_2, \tfrac{t}{2}\right) = 0 \end{aligned} \tag{4.6}$$

$$\begin{aligned} &u_i\left(0,0,0\right) = 0 \\ &\left\langle \frac{\partial u_1}{\partial x_2} \right\rangle = \left\langle \frac{\partial u_2}{\partial x_1} \right\rangle \end{aligned} \tag{4.7}$$

IV.C.2. Material Properties

The laminate consisted of IM7/8552 unidirectional carbon-epoxy. Table IV.8 shows the elastic properties of IM7/8552, where 1 indicates the fiber direction.

In order to encourage the damage to localize in the progressive damage analysis, a distribution of strength parameters will be used, with each quadrature point having its own random value from the distribution. A Weibull distribution, as defined in Equation (4.8), taken from Ref. [107], was used for each damage parameter, where the scale parameter, λ, will be the strength value and the shape parameter, k, will be chosen to result in the lowest amount of variability that provides localization. To determine the shape parameter, ten shape parameters ranging from 2 to 1000 were considered, and the highest value that provided localization was chosen, which was k=100. Figure IV.20 shows the probability density for the Weibull distribution using a shape parameter of 100 and a scale parameter of 1. Values outside the range of 0.92 to 1.02 had a probability density less than 0.1% of the probability density at 1. For the continuum damage models, the strength values were assigned using a distribution. However, for the cohesive zone models, only the critical tractions were assigned using a distribution, while no distribution was used for the penalty stiffness and strain energy release. The failure properties used for each ply were taken from Ref. [108], which is shown in Table IV.9. The assumed properties used for the cohesive zone elements are shown in Table IV.10.

$$f(x) = \frac{k}{\lambda}\left(\frac{x}{\lambda}\right)^{k-1} e^{-(x/\lambda)^k} \tag{4.8}$$

Table IV.8. Elastic properties for IM7/8552 carbon-epoxy

E_{11}	161.0 GPa
E_{22}	11.38 GPa
ν_{12}	0.32
ν_{23}	0.436
G_{12}	5.17 GPa
G_{23}	3.98 GPa

Table IV.9. Failure properties for IM7/8552 carbon-epoxy

Longitudinal tensile strength, σ_{11c}^{T}	2600 MPa
Longitudinal compressive strength, σ_{11c}^{C}	1500 MPa
Transverse tensile strength, σ_{22c}^{T}	60 MPa
Transverse compressive strength, σ_{22c}^{C}	290 MPa
Shear strength, $\sigma_{12c} = \sigma_{21c}$	90 MPa

Table IV.10. Cohesive zone properties for IM7/8552 carbon-epoxy

Penalty stiffness, $K_{penalty}$	1e6 GPa
Mode I strain energy release rate, G_{Ic}	200 J/m^2
Mode II strain energy release rate, G_{IIc}	1000 J/m^2
Critical normal traction, t_{nc}	60 MPa
Critical shear traction, $t_{t1c} = t_{t2c}$	90 MPa

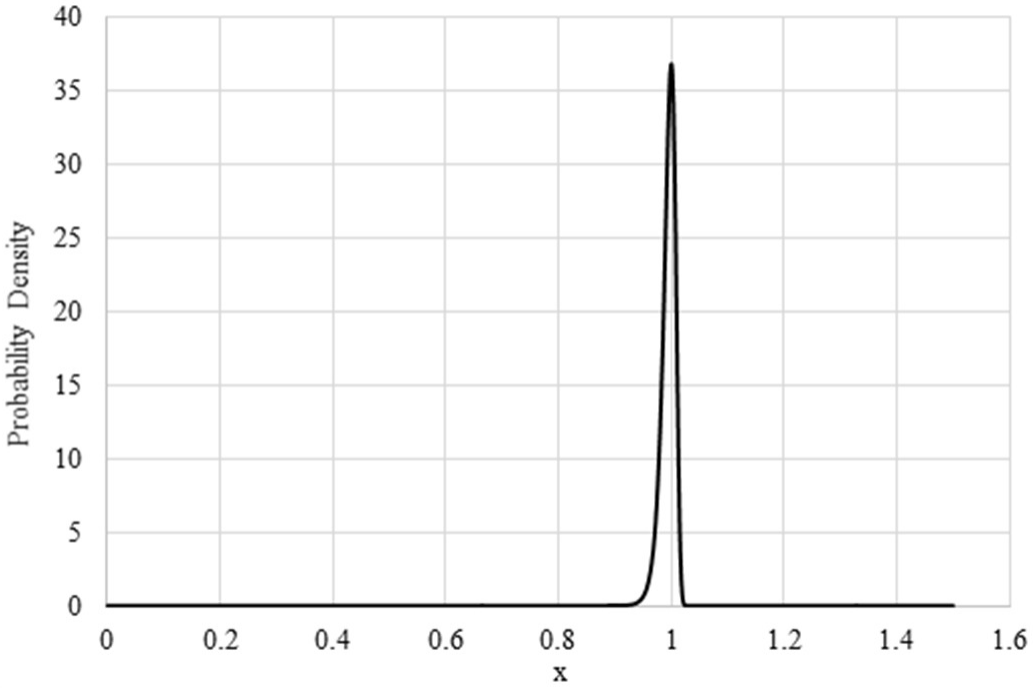

Figure IV.20. Probability density for Weibull distribution where $k = 100$ and $\lambda = 1$

IV.C.3. Uniaxial Loading

For uniaxial load, the volume average stress-strain response, crack density evolution, and two-point correlation functions are used to compare the damage models. This section begins with a description of the finite element meshes used for this load configuration, followed the results of each of the methods of comparison used to evaluate the similarities and differences of the considered damage models.

IV.C.3.a. Meshes

Using the coordinate system illustrated in Figure IV.19, Table IV.11 contains the number of elements along the x1 and x3 axes for the uniform structured meshes. No variation occurs in the x2 direction under the load considered in this work, so only a single element will be used in that direction. The reference mesh will be used to compare all the methods, while a refined mesh is only used for some of the damage models to study the effects of mesh refinement on the damage states. For the cohesive zone model, cohesive zone elements are placed parallel to the fiber direction in 90° ply and along the ply interface, which is illustrated in Figure IV.21. For the case of cohesive zones combined with the element degradation method, cohesive zone elements are only placed along the ply interface in order to model delamination, and the continuum damage elements model damage in the plies.

IV.C.3.b. Volume Average Comparison

The volume averaged stress-strain curves for the various models are presented in Figure IV.22 and Figure IV.23. Figure 9 shows that the quadrature point degradation

Table IV.11. Number of elements along each axis in meshes used for the uniaxial load progressive damage analyses

	# Elements along x_1	# Elements along x_3
Continuum Damage Reference Mesh	160	20
Continuum Damage Refined Mesh	320	40
Continuum Damage + Cohesive Zones Reference Mesh	160	20*
Cohesive Zone Reference Mesh	160	20*
Cohesive Zone Refined Mesh	320	40*

* Does not include cohesive zones elements

method and element degradation method did not differ much until $\langle \varepsilon_{11} \rangle$ exceeded 1.4%. The effective stiffness began to change for the different methods between an applied strain of 0.45% and 0.5%. The effective stiffness decreases once damage initiates, remains roughly constant for most of the progression of damage, and is drastically reduced once failure in the 00 ply occurs. At final failure, the quadrature point degradation method predicted an applied volume average strain of about 1.4%, and the other three methods predicted final failure at about 1.5% strain.

Figure IV.23 shows that the introduction of cohesive zones along the ply interface for the element degradation method did not have much effect on the volume average response. From the figures, the progression of damage can be divided into three sections: initiation, growth of damage, and final failure. For comparisons using crack density and two-point correlation functions in the next two sections, three strain values will be chosen, each representing one of these sections: near initiation (0.55%), during growth of damage (0.9%), and near final failure (1.4%).

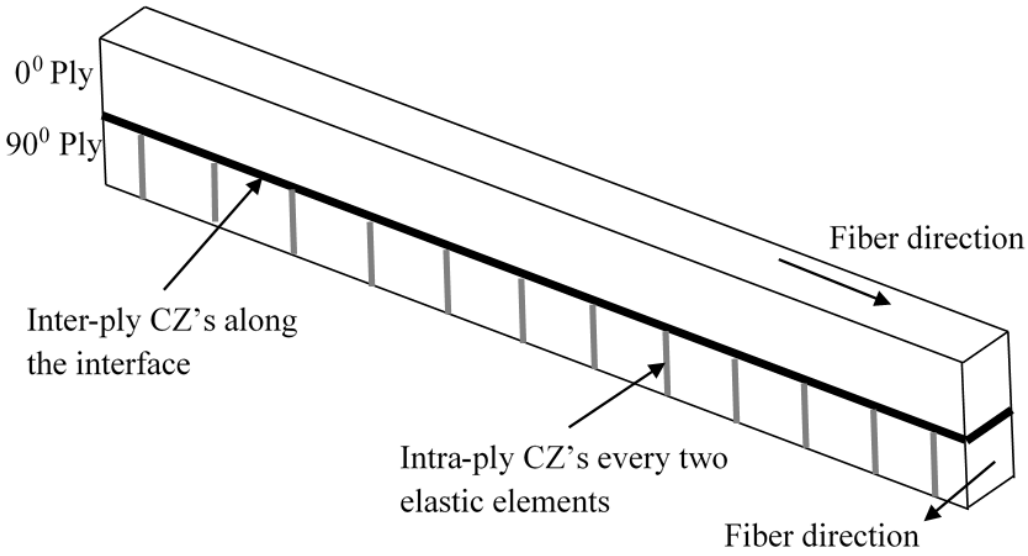

Figure IV.21. Illustration of the location of cohesive zones in the meshes used for the cohesive zone model under uniaxial load

IV.C.3.c. Crack Density Evolution Comparison

The crack density evolution using the different methods are shown in Figure IV.24. The onset of cracking occurs at about the same strain for all methods compared. After initiation, the quadrature point degradation method resulted in a significantly higher crack density. The addition of cohesive zone elements along the ply interface had little impact on the crack density evolution of the element degradation method. The crack density for the cohesive zone model was much slower to evolve than for the continuum damage models, but the final crack density was similar to the element degradation method.

Figure IV.25 shows the effect of mesh refinement for the element degradation method and cohesive zone model. The mesh refinement did not change the initiation of cracking for either method. For the cohesive zone model, the higher refinement

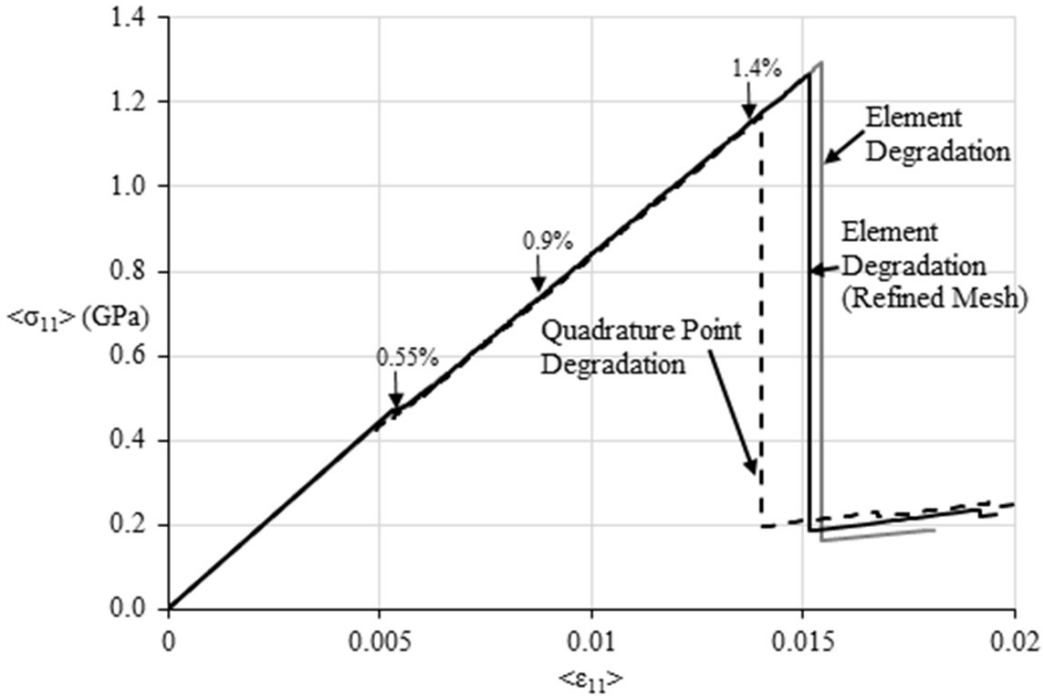

Figure IV.22. Volume average stress-strain curve under uniaxial load using the quadrature point degradation method, element degradation method, and element degradation method with a refined mesh

resulted in a slower progression of new cracks forming compared to the unrefined mesh, but the refined mesh showed a jump in crack density very close to final failure, which was higher than the value for the unrefined mesh. For the element degradation method, the crack density remained similar for both mesh refinements until about 1% stain, at which point the crack density for the refined mesh increased rapidly, while the crack density for the unrefined mesh increased at a much slower rate. The mesh refinement did not affect the strain at final failure significantly.

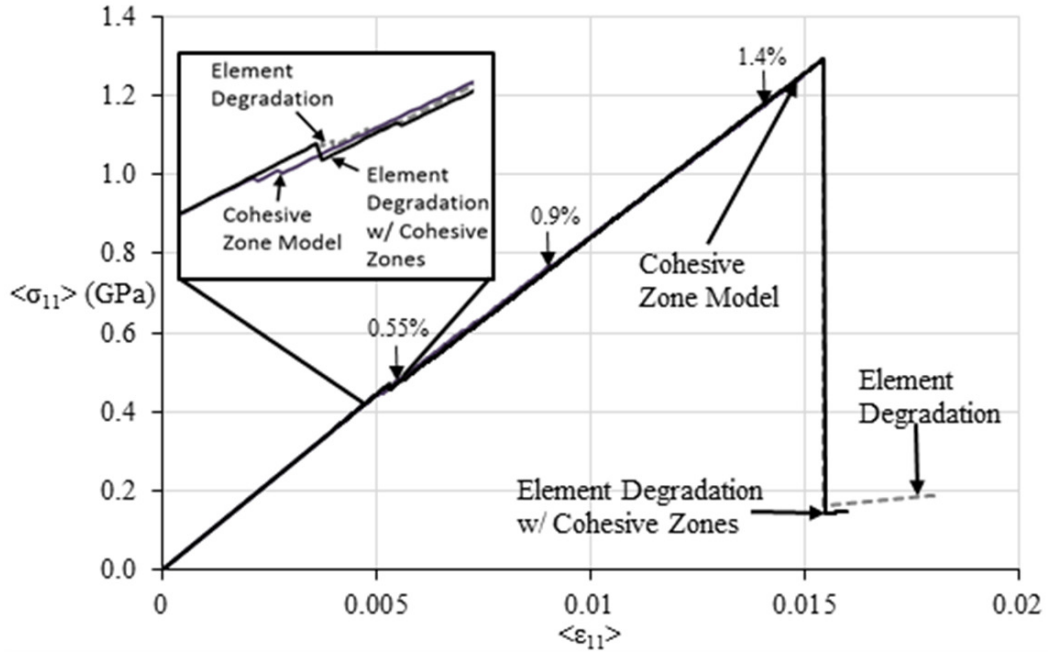

Figure IV.23. Volume average stress-strain curve under uniaxial load using the cohesive zone model, element degradation method, and combination of element degradation and cohesive zones

IV.C.3.d. Two-Point Correlation Comparison

Figure IV.26 shows the differences between damage states, κ as described in a previous section, for continuum damage methods. For the strain near initiation, it is shown that the addition of cohesive zones along the ply interface does not have an impact on the damage state when using the element degradation method. Also, the quadrature point degradation differed from the other methods by a larger amount than any other two methods. At the strain near damage initiation, the quadrature point degradation and element degradation with cohesive zones predicted the same crack density, while the element degradation method predicted a lower value. However, the locations of cracks predicted using the element degradation with

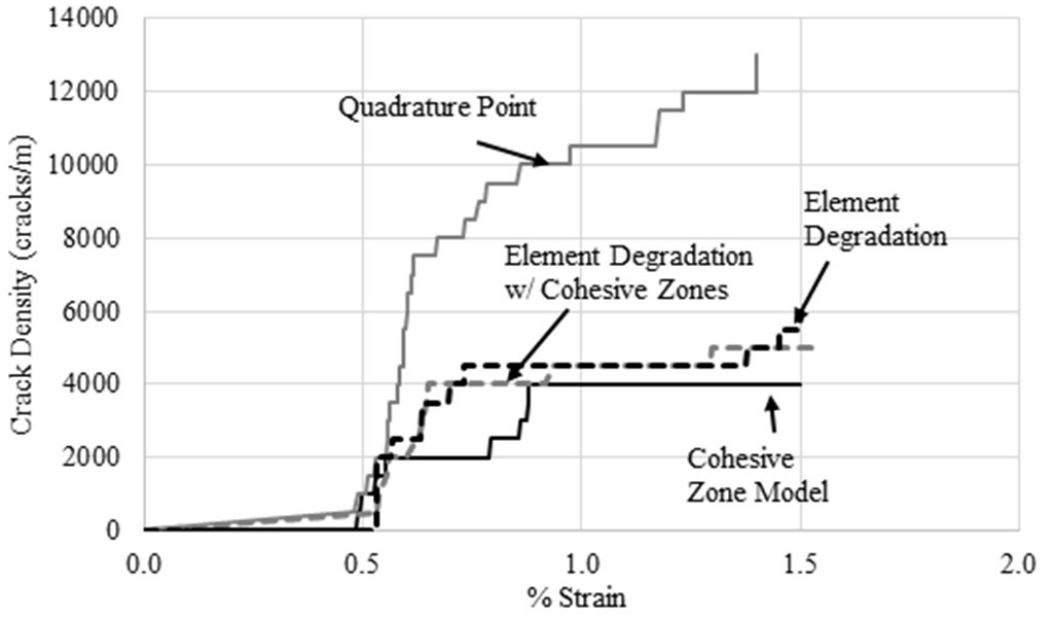

Figure IV.24. Crack density evolution up to final failure in the 0° ply using the different damage methods

cohesive zones and element degradation were clustered. Because of the locations of the cracks, the two methods predict a more similar damage state in terms of the two-point correlations than the quadrature point degradation, explaining the values of κ. The introduction of cohesive zones along the interface had a much lower effect on the damage state than the use of the quadrature degradation method. Mesh refinement had the smallest impact on the damage state. The same trends held for the other strain values considered.

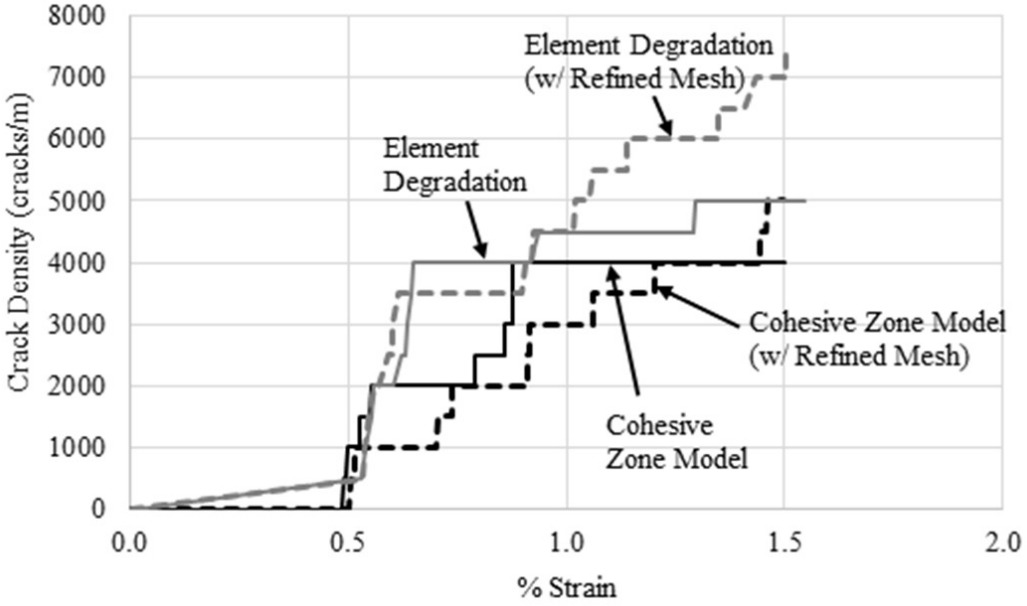

Figure IV.25. Crack density evolution up to final failure in the 0° ply showing the effects of mesh refinement

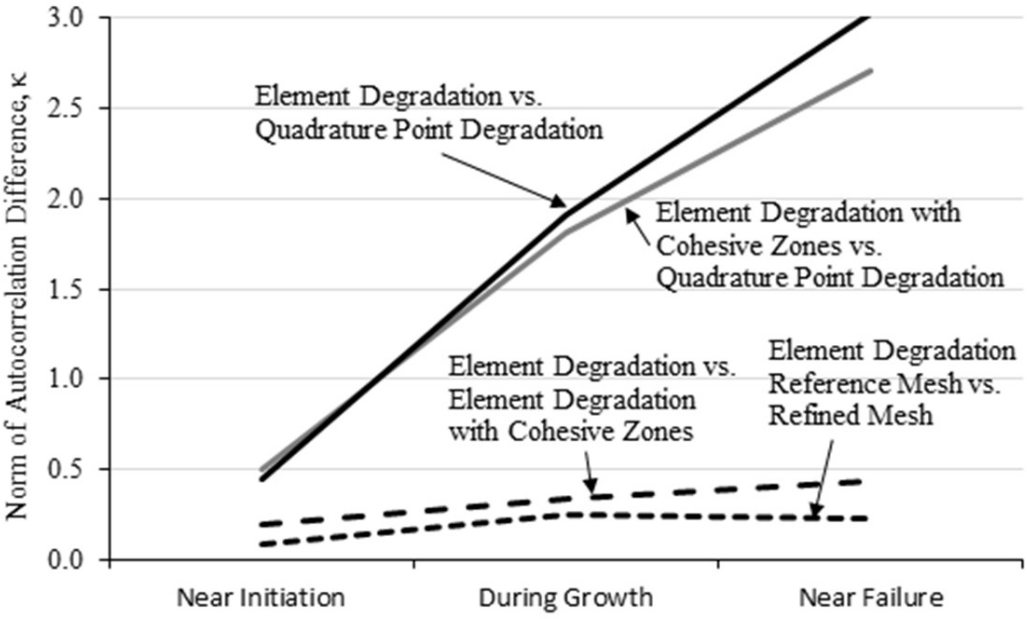

Figure IV.26. Difference, κ, between each of the different continuum methods

IV.C.4. In-Plane Shear Loading

For in-plane shear load, the images of the damage states and volume average stress-strain responses are compared for the damage models considered. This section begins with a description of the finite element meshes used for this load configuration, followed by a qualitative discussion of the damage states based on the visualization of damaged elements, and finished with a comparison of volume average responses.

IV.C.4.a. Meshes

Using the coordinate system illustrated in Figure IV.19, Table IV.12 contains the number of elements along each axis for the uniform, structured meshes. For the cohesive zone model, two configurations are considered. First, cohesive zone elements are placed parallel to the fiber direction in each laminae and along the ply interface, which is illustrated in Figure IV.27. Second, cohesive elements are placed along both in-plane directions (parallel and perpendicular to the fiber direction) and along the ply interface, which is illustrated in Figure IV.28.

IV.C.4.b. Qualitative Comparison of Damage States

Under in-plane shear, the continuum damage methods predict damage growth in both in-plane directions (parallel and perpendicular to fibers). In the continuum analyses, two lines of damage extended (one in each in-plane direction) through the entire laminate thickness. For this reason, comparing the crack density would be trivial, since only one crack in each direction forms, and is therefore excluded from this results section. Similarly, the two-point correlation functions do not provide any

Table IV.12. Number of elements along each axis in meshes used for the in-plane shear load progressive damage analyses

	# Elements along x_1 and x_2	# Elements along x_3
Continuum Damage Mesh	20	8
Cohesive Zone Mesh	20	8*

* Does not include cohesive zones elements

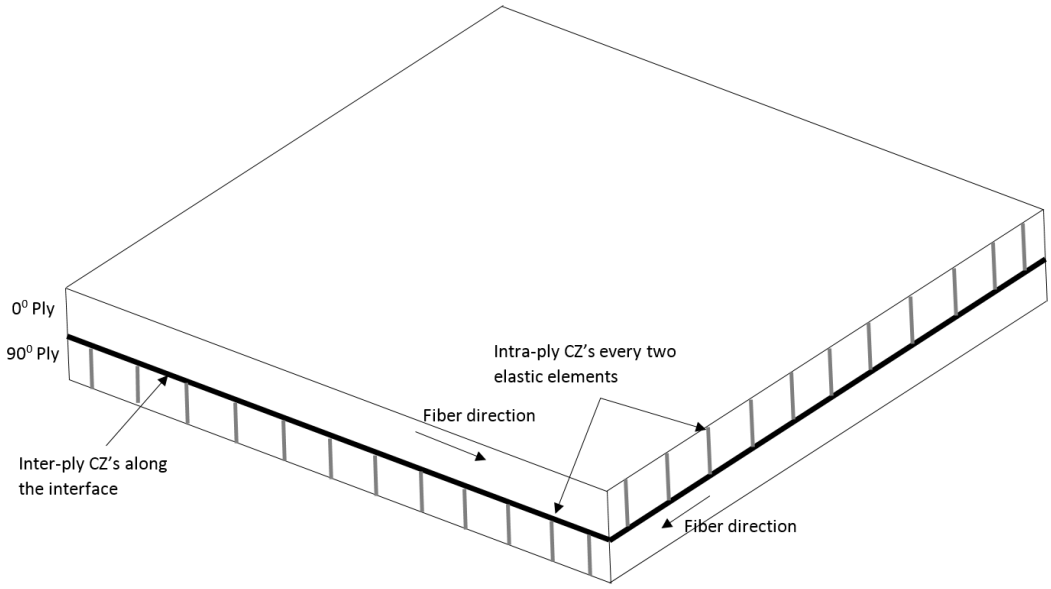

Figure IV.27. Illustration of cohesive zones only along fiber direction in the meshes used for the cohesive zone model under in-plane shear load

new insight since there is very little difference in the damage states between different analyses. Consequently, this section aims to state observations about the damage states.

The element degradation method predicts a linear response up until about 1.8% volume average shear strain, at which point a few elements fail creating stress concentrations, as shown in Figure IV.29.

Within the same load step, the stress concentrations quickly cause some neigh-

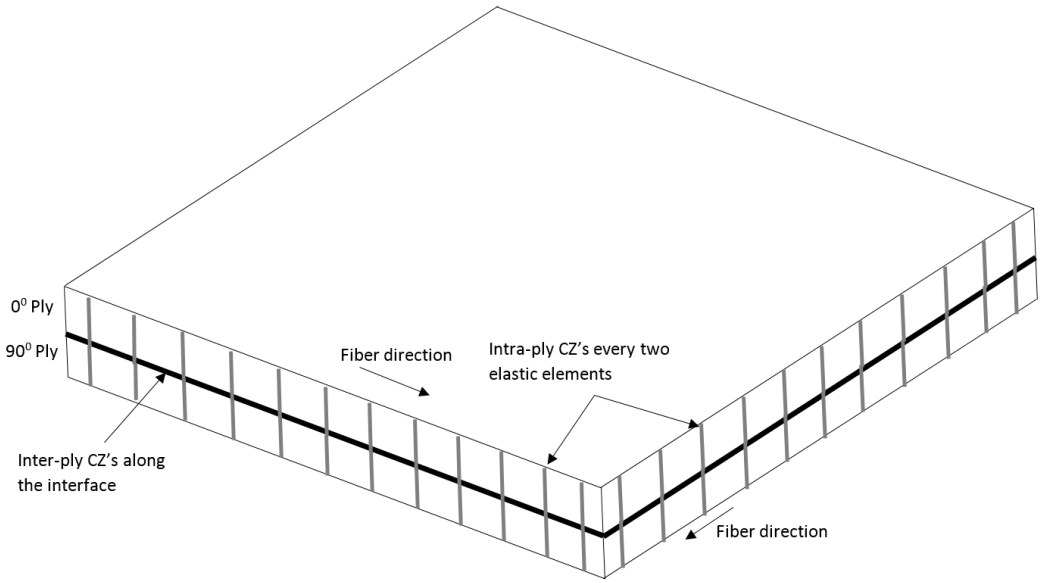

Figure IV.28. Illustration of cohesive zones along both in-plane directions in the meshes used for the cohesive zone model under in-plane shear load

boring elements to fail, see Figure IV.30, which continues until two lines of damage forms, as shown in Figure IV.31.

Ply cracks due to shear load have been observed to grow in both directions during experiments, but they were stated to be less likely than only growing along the fiber direction. When the damage was observed to cross fibers, the fibers remained intact. [109] However, in the case of the continuum damage models, the damage always grow in both directions and through the thickness of the laminate. In this aspect, the predicted damage growth under in-plane shear by the considered continuum damage models appears improbable, if not unrealistic.

At first, the cohesive zone model seemed to circumvent the issue, since cohesive elements were only placed along the fiber direction initially. An example of the opening of the cohesive zones in this configuration can be seen in Figure IV.32.

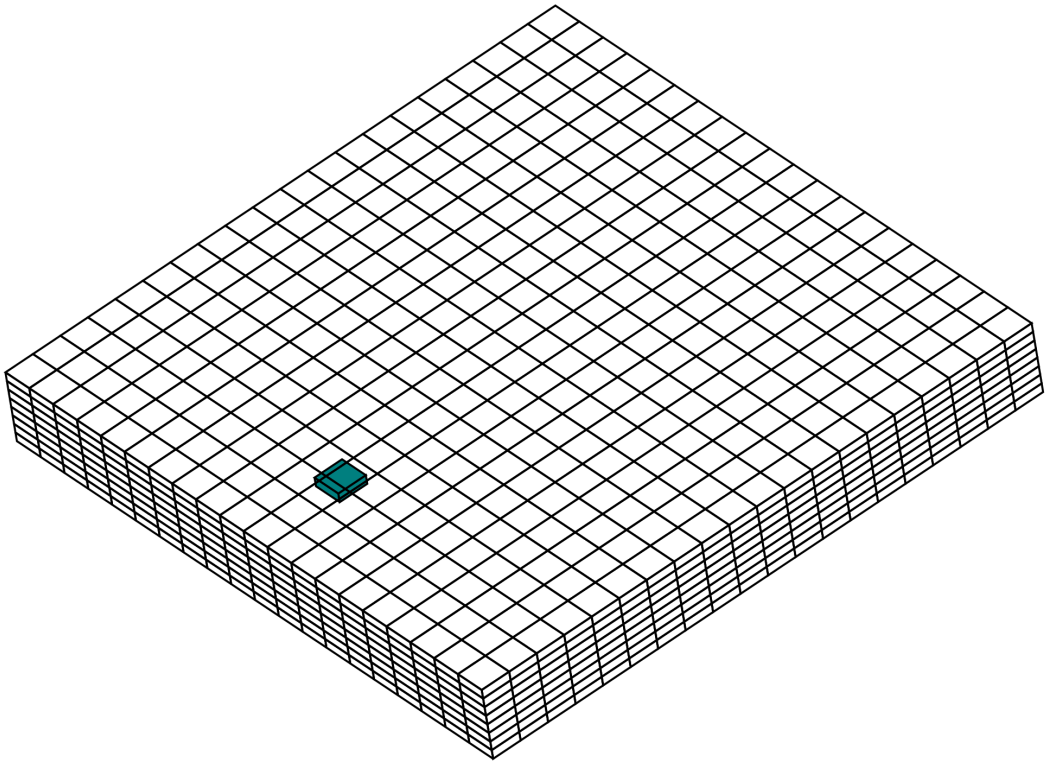

Figure IV.29. Visualization of damage elements under in-plane shear load using element degradation method at first element failure

Cracks form along the fiber directions where cohesive zones are placed, but every cohesive zone in the plies experiences mode II opening. The damage was expected to localize, but in this configuration, localization does not occur.

To more fairly compare the predictions of the damage models, cohesive zone elements should be placed along both in-plane directions. With cohesive zones running in both directions, the predicted final configuration closely matched the continuum damage models. A discrete crack spreading in both in-plane directions and through the laminate thickness was observed. An example of the this configuration at an applied 3% volume average in-plane shear strain is shown in Figure IV.33 using a

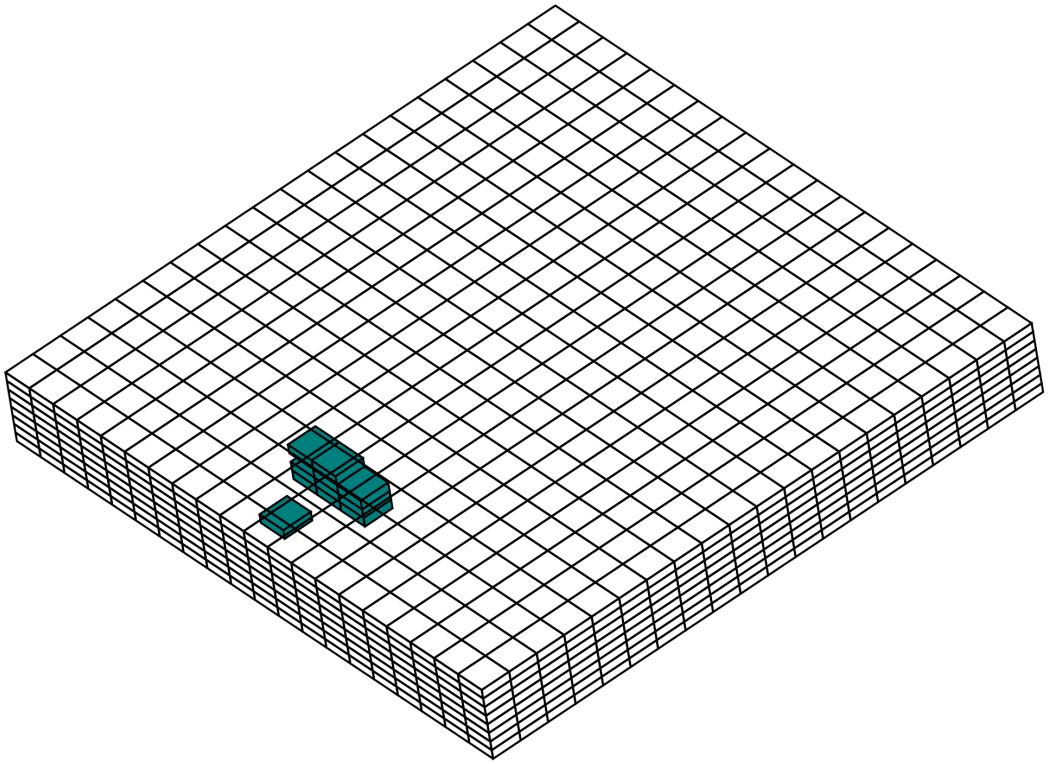

Figure IV.30. Visualization of damage elements under in-plane shear load using element degradation method at next iteration after first element failure

smaller mesh to allow better visualization of the through thickness damage. Unlike the previous cohesive zone case, localization occurs very well, similar to the behavior observed for the continuum damage models.

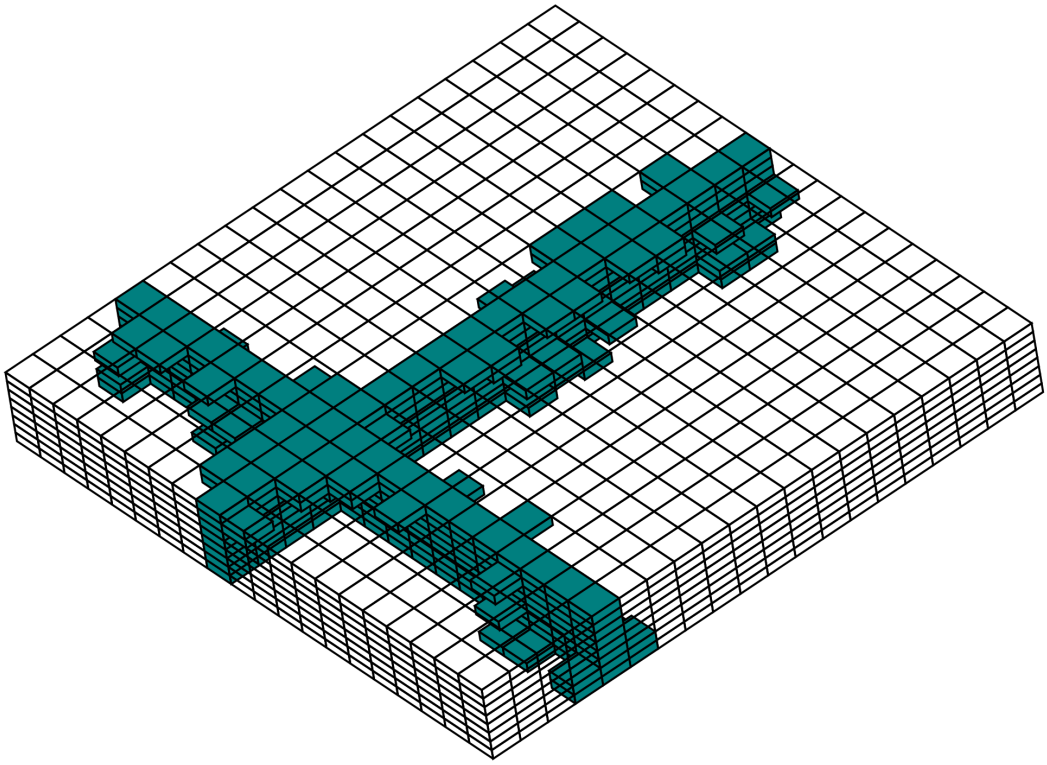

Figure IV.31. Visualization of damage elements under in-plane shear load using element degradation method after iterations are complete for load step at which failure occurs

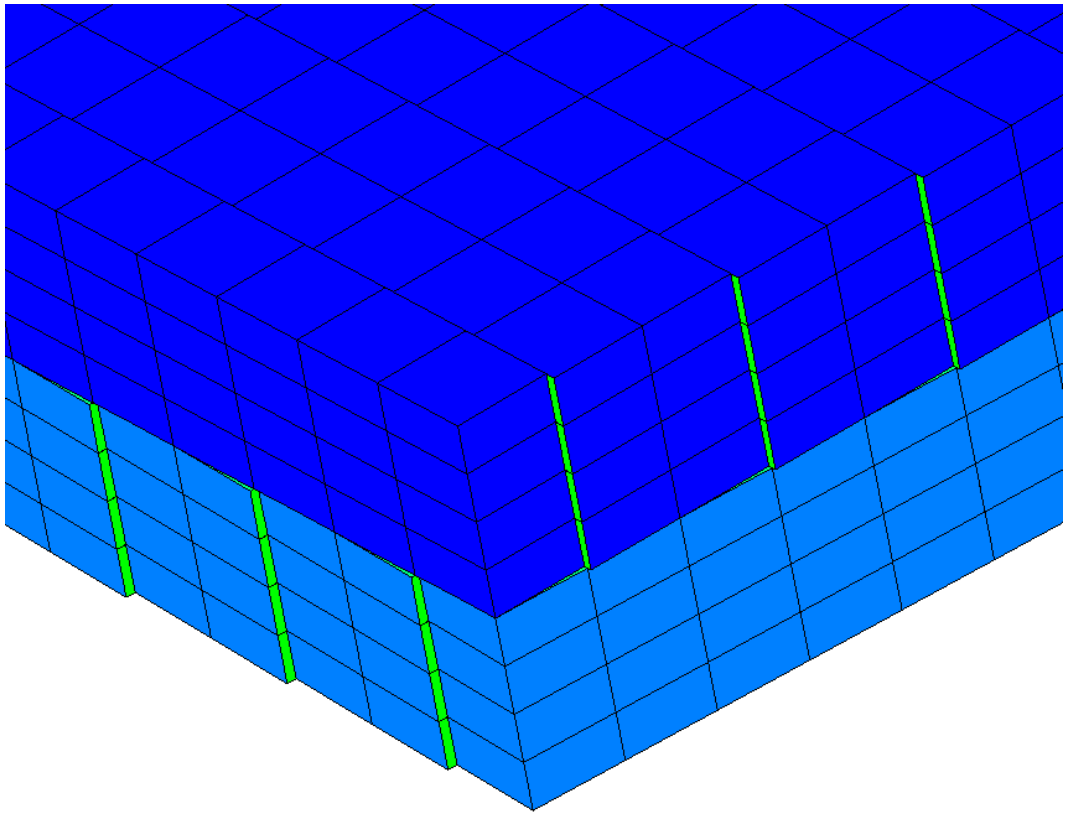

Figure IV.32. Visualization of cohesive zones opening under in-plane shear load with cohesive elements only placed parallel to the fiber direction

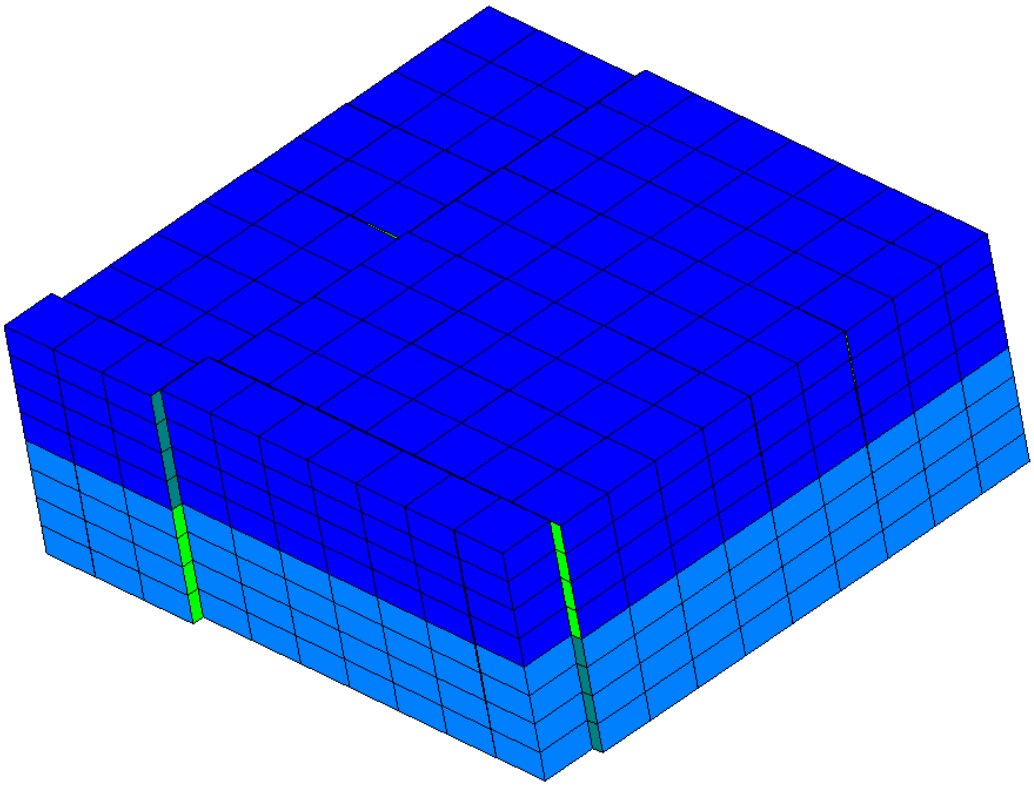

Figure IV.33. Visualization of cohesive zones opening under in-plane shear load with cohesive elements placed along both in-plane directions (a smaller mesh is shown to allow better visualization)

IV.C.4.c. Volume Average Comparison

Figure IV.34 shows the volume average stress-strain curve for the different progressive damage models. For all the methods, the volume average response started linear, then suddenly dropped at a volume average in-plane shear strain value. The softening observed in the uniaxial case was not observed for the shear load case. The volume average response of both cohesive zone configurations (only along fibers and in both directions) and the quadrature point degradation method agreed quite well.

The element degradation method predicted failure to occur at a stress very close to the nominal shear strength (90 MPa), while the other methods predicted a lower stress for failure to occur. Since the element degradation method requires all the quadrature points in an element to fail before degrading the material, it is less sensitive to the distribution of strengths.

Placing cohesive zones in both in-plane directions made little difference in the volume average response for the cohesive zone model.

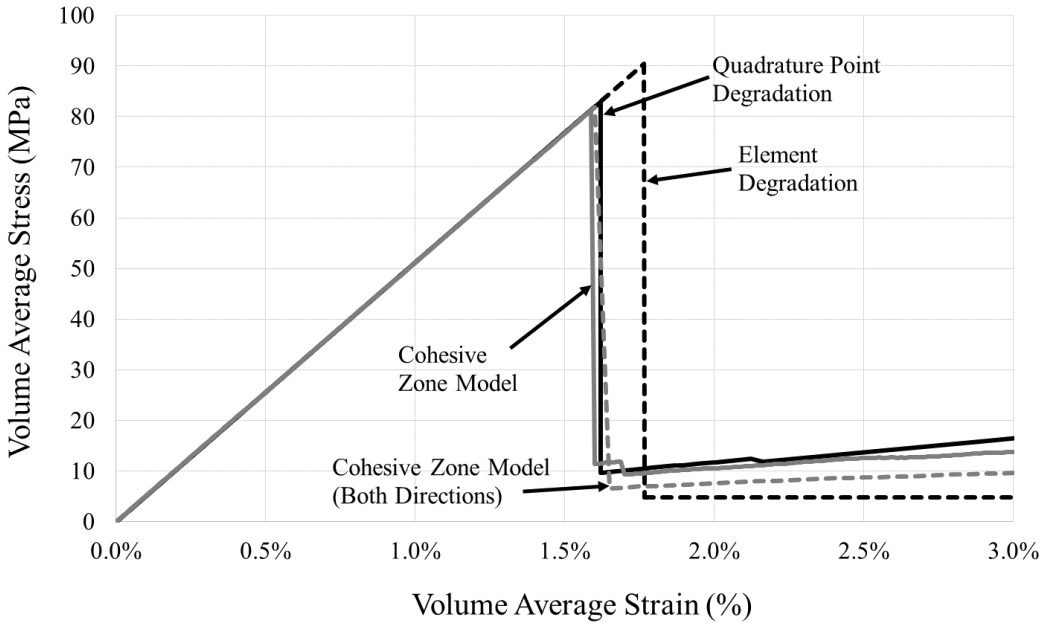

Figure IV.34. Volume average stress-strain curve under in-plane shear load using the cohesive zone model (both configurations), element degradation method, and quadrature point degradation method

CHAPTER V

CONCLUSIONS

The scope of this work is broad as it covers multiple scales, inverse methods, damage models, and numerical strategies, but it improves or offers insight into several aspects of a unified multiscale framework used to analyze fiber-reinforced composites.

In the determination of fiber properties, parametric studies were used to suggest an appropriate combination of RVE size and number of realizations. It was shown that the extent to which a set of random microstructures satisfies transverse isotropy depends on both the RVE size and the number of realizations. It was also shown that the average values of predicted lamina properties do not vary for the RVE sizes studied as long as a sufficient number of realizations are used, but the standard deviation of the properties (a measure of the distribution of properties within the set of realizations) decreases for larger RVE sizes. Based on these findings, several appropriate combinations of RVE size and number of realizations were identified to fully characterize both the average lamina properties as well as the standard deviation of lamina properties.

Comparing the predicted fiber properties using three methods, it was noted that the microstructure has a significant impact on the predicted longitudinal shear modulus of the fiber. By examining the relationship between the spacing of fibers and the predicted properties, the longitudinal shear modulus of the fiber was shown to increase approximately linearly with the minimum spacing fraction. This is because an increase in the minimum spacing fraction causes the random microstructure to be

more uniform and form fewer networks, causing the lamina to be more compliant for higher spacing fractions and requiring a stiffer fiber to match experimental results. The properties predicted for the IM7 and T650-35 fibers showed close similarity to those presented in the literature with the exception of the longitudinal shear modulus, which was much lower for the random microstructure. The properties for AS4 and T300 found in the literature differed significantly from the properties predicted in this work; however it was noted that the properties in the literature had inconsistencies.

For the glass material system, if isotropy of the fibers was not enforced, the resulting fiber properties were not isotropic. As a result, isotropy was enforced, and the fiber properties were determined using three different microstructural models. The predicted isotropic moduli matched the values reported in the literature quite well, although the Poisson's ratio was higher for the methods used in this work than the value reported. If the fibers are known to be close to isotropic and isotropic properties are desired, the algorithm must be modified to enforce the isotropy of the fibers.

At the mesoscale, a few continuum damage models were compared with a cohesive model. During the validation of the cohesive zone model, convergence issues were discovered. Different iterative techniques were investigated, which showed that the direct method performs very well when cohesive zones suddenly open, the Newton-Raphson method offers the fastest convergence rate if it can converge, and using a mix of the tangent and secant stiffness to approximate the tangent matrix can avoid non-convergence, but the optimal mix ratio depends on the problem. It appears that a modified Newton-Raphson method switching between the exact tangent stiffness

and using the secant stiffness to approximate the tangent stiffness depending on the convergence rate might offer the best convergence behavior and should be considered in future work.

The damage models were compared for a $[0/90]_s$ laminate under uniaxial and shear load. Under uniaxial tension, the volume average response matched well for the different methods, with quadrature point degradation predicting a lower final strain value. The crack density evolution showed that all methods predicted the initiation of ply cracks at about the same strain value. Quadrature point degradation predicted a much higher crack density than the other methods at strains higher than 0.55%. The introduction of cohesive zones to the element degradation method had little effect on the crack density. The crack density predicted by the cohesive zone model was much slower to evolve than the other methods. Mesh refinement had a significant impact on the crack density evolution, but the cohesive zone model was less sensitive to mesh refinement than the continuum damage model.

Two-point correlation functions offered a method of comparing damage states, while taking into account the amount and location of the damage. It showed that the damage states using quadrature point degradation significantly differed from the other methods. Mesh refinement showed a lower impact on the damage states than the introduction of cohesive zones along the ply interface, which is interesting since the crack density showed the opposite trend.

Under in-plane shear, the continuum damage models predicted damage growth in both in-plane directions and through the laminate thickness, but experimental data has shown that damage growth across fibers is less likely to occur than growth

only along fibers. [109] The cohesive zone model predicted the same behavior if cohesive elements were placed along both directions. If cohesive zones were placed only along fibers, the unrealistic behavior could be avoided, but then localization fails to occur.

In summary, this work set out to contribute to a multiscale framework at the microscale and mesoscale. At the microscale, improved elastic properties for graphite fibers were determined, with an algorithm delineated that can be used to determine other fiber properties, such as thermal conductivity. In addition, suggestions for the RVE size and number of realizations to use for inverse problems at the microscale were offered. At the mesoscale, two categories of progressive damage models were considered: continuum damage and cohesive zone models. A method of comparing damage states was developed using two-point correlation functions. Cohesive zones were shown to offer the ability to place the damage elements in the desired locations but can sometimes suffer numerical issues, which were investigated. The continuum damage models considered can predict ambiguous damage states, making it difficult to obtain quantitative properties, such as the crack density, but they were shown to offer similar predictions to the cohesive zone model by some measures, especially the volume average response, for less computational cost.

REFERENCES

[1] King, T., Blackketter, D., Walrath, D., and Adams, D., "Micromechanics Prediction of the Shear Strength of Carbon Fiber/Epoxy Matrix Composites: The Influence of the Matrix and Interface Strengths," *Journal of Composite Materials*, Vol. 26, No. 4, 1992, pp. 558–573.

[2] Rupnowski, P., Gentz, M., Sutter, J., and Kumosa, M., "An evaluation of the elastic properties and thermal expansion coefficients of medium and high modulus graphite fibers," *Composites Part A: Applied Science and Manufacturing*, Vol. 36, No. 3, March 2005, pp. 327–338.

[3] Pagano, N. and Tandon, G., "Thermo-elastic model for multidirectional coated-fiber composites: traction formulation," *Composites Science and Technology*, Vol. 38, 1990, pp. 247–269.

[4] Pagano, N., Schoeppner, G. A., Kim, R., and Abrams, F., "Steady-state cracking and edge effects in thermo-mechanical transverse cracking of cross-ply laminates," *Composites Science and Technology*, Vol. 58, No. 11, Nov. 1998, pp. 1811–1825.

[5] González, C. and LLorca, J., "Mechanical behavior of unidirectional fiber-reinforced polymers under transverse compression: Microscopic mechanisms and modeling," *Composites Science and Technology*, Vol. 67, No. 13, Oct. 2007, pp. 2795–2806.

[6] Brockenbrough, J., Suresh, S., and Wienecke, H., "Deformation of metal-matrix composites with continuous fibers: geometrical effects of fiber distribution and shape," *Acta Metallurgica*, Vol. 39, No. 5, 1991, pp. 735–752.

[7] Oh, J. H., Jin, K.-K., and Ha, S. K., "Interfacial Strain Distribution of a Unidirectional Composite with Randomly Distributed Fibers under Transverse Loading," *Journal of Composite Materials*, Vol. 40, No. 9, July 2005, pp. 759–778.

[8] Garnich, M. R., Fertig, R. S., Anderson, E. M., and Deng, S., "Micromechanics of Fatigue Damage in Unidirectional Polymer Composites," *53nd AIAA/ASME/ASCE/AHS/ASC Structures, Structural Dynamics, and Materials Conference*, No. April, Honolulu, HI, 2012, pp. 1–9.

[9] Anderson, E. M., *An Automated Finite Element Program for Micromechanics Modeling of Random-Wavy Fiber Composites*, Masters, University of Wyoming, Laramie, Wyoming, 2010.

[10] McLendon, W. R., *A Multiscale Framework for the Characterization of Damage in Textile Composites Under Thermomechanical Loads*, Ph.D. thesis, Texas A&M University, College Station, Texas, 2013.

[11] Turon, A., Camanho, P., Costa, J., and Dvila, C., "A damage model for the simulation of delamination in advanced composites under variable-mode loading," *Mechanics of Materials*, Vol. 38, No. 11, 2006, pp. 1072 – 1089.

[12] Needleman, A., "An analysis of tensile decohesion along an interface," *Journal of the Mechanics and Physics of Solids*, Vol. 38, No. 3, 1990, pp. 289 – 324.

[13] Park, K., Paulino, G. H., and Roesler, J. R., "A unified potential-based cohesive model of mixed-mode fracture," *Journal of the Mechanics and Physics of Solids*, Vol. 57, No. 6, 2009, pp. 891 – 908.

[14] Gao, Y. F. and Bower, A. F., "A simple technique for avoiding convergence problems in finite element simulations of crack nucleation and growth on cohesive interfaces," *Modelling and Simulation in Materials Science and Engineering*, Vol. 12, 2004, pp. 453 463.

[15] Voigt, W., "Theoretische Studien ber die Elasticittsverhltnisse der Krystalle," *Abh.Kgl.Ges.Wiss.Gttingen, Math.Kl.*, Vol. 34, 1887, pp. 3–51.

[16] Reuss, A., "Berechnung der Fliegrenze von Mischkristallen auf Grund der Plastizittsbedingung fr Einkristalle," *Journal of Applied Mathematics and Mechanics*, Vol. 9, 1929, pp. 49–54.

[17] Hashin, Z.and Shtrikman, S., "A variational approach to the theory of the elastic behavior of multiphase materials," *J. Mech. Phys. Solids*, Vol. 11, 1963, pp. 127–140.

[18] Hashin, Z. and Shtrikman, S., "Conductivity of Polycrystals," *Phys. Rev.*, Vol. 130, Apr 1963, pp. 129–133.

[19] Hashin, Z., "On elastic behaviour of fibre reinforced materials of arbitrary transverse phase geometry," *Journal of the Mechanics and Physics of Solids*, Vol. 13, No. 3, 1965, pp. 119 – 134.

[20] Dvorak, G. J. and Bahei-El-Din, Y. A., "Plasticity Analysis of Fibrous Composites," *Journal of Applied Mechanics*, Vol. 49, 1982, pp. 327.

[21] Eshelby, J. D., "The Determination of the Elastic Field of an Ellipsoidal Inclusion, and Related Problems," *Royal Society of London Proceedings Series A*, Vol. 241, Aug. 1957, pp. 376–396.

[22] Eshelby, J. D., "The Elastic Field Outside an Ellipsoidal Inclusion," *Proceedings of the Royal Society of London. Series A, Mathematical and Physical Sciences*, Vol. 252, No. 1271, 1959, pp. pp. 561–569.

[23] Mura, T., *Micromechanics of Defects in Solids*, Comparative Studies in Overseas History, Springer Netherlands, 1987.

[24] Gavazzi, A. C. and Lagoudas, D. C., "On the numerical evaluation of Eshelby's tensor and its application to elastoplastic fibrous composites," *Computational Mechanics*, Vol. 7, Jan. 1990, pp. 13–19.

[25] Mori, T. and Tanaka, K., "Average stress in matrix and average elastic energy of materials with misfitting inclusions," *Acta Metallurgica*, Vol. 21, No. 5, May 1973, pp. 571–574.

[26] Hill, R., "A self-consistent mechanics of composite materials," *Journal of the Mechanics and Physics of Solids*, Vol. 13, No. 4, 1965, pp. 213 – 222.

[27] Roscoe, R., "The viscosity of suspensions of rigid spheres," *British Journal of Applied Physics*, Vol. 3, No. 8, 1952, pp. 267.

[28] Boucher, S., "On the effective moduli of isotropic two-phase elastic composites," *Journal of Composite Materials*, Vol. 8, No. 4, 1979, pp. 82 – 89.

[29] Aboudi, J. and Pindera, M., *Micromechanics of metal matrix composites using the generalized method of cells model (GMC) user's guide [microform] / Jacob Aboudi and Mark-Jerzy Pindera*, National Aeronautics and Space Administration ; National Technical Information Service, distributor [Washington, DC : Springfield, Va, 1992.

[30] Torquato, S., *Random Heterogeneous Materials: Microstructure and Macroscopic Properties*, Interdisciplinary Applied Mathematics, Springer, 2002.

[31] Berveiller, M. and Zaoui, A., "An extension of the self-consistent scheme to plastically-flowing polycrystals," *Journal of Mechanics Physics of Solids*, Vol. 26, Dec. 1978, pp. 325–344.

[32] Tandon, G. and Weng, G., "A theory of particle-reinforced plasticity," *Journal of Applied Mechanics*, Vol. 55, 1988, pp. 126.

[33] Suquet, P., "Overall Properties of Nonlinear Composites," *IUTAM Symposium on Micromechanics of Plasticity and Damage of Multiphase Materials*, edited by A. Pineau and A. Zaoui, Vol. 46 of *Solid Mechanics and its Applications*, Springer Netherlands, 1996, pp. 149–156.

[34] Castaneda, P., "The effective mechanical properties of nonlinear isotropic composites," *Journal of the Mechanics and Physics of Solids*, Vol. 39, No. 1, 1991, pp. 45 – 71.

[35] Castañeda, P. P., "Exact second-order estimates for the effective mechanical properties of nonlinear composite materials," *Journal of the Mechanics and Physics of Solids*, Vol. 44, No. 6, 1996, pp. 827–862.

[36] Ponte Castañeda, P., "Second-order homogenization estimates for nonlinear composites incorporating field fluctuations: Itheory," *Journal of the Mechanics and Physics of Solids*, Vol. 50, No. 4, 2002, pp. 737–757.

[37] Ponte Castañeda, P., "Second-order homogenization estimates for nonlinear composites incorporating field fluctuations: IIapplications," *Journal of the Mechanics and Physics of Solids*, Vol. 50, No. 4, 2002, pp. 759–782.

[38] Castaneda, P., "Linear Comparison Methods for Nonlinear Composites," *Nonlinear Homogenization and its Applications to Composites, Polycrystals and Smart Materials*, edited by P. Castaeda, J. Telega, and B. Gambin, Vol. 170 of *NATO Science Series II: Mathematics, Physics and Chemistry*, Springer Netherlands, 2005, pp. 247–268.

[39] Delannay, L., Doghri, I., and Pierard, O., "Prediction of tensioncompression cycles in multiphase steel using a modified incremental mean-field model," *International Journal of Solids and Structures*, Vol. 44, No. 2223, 2007, pp. 7291 – 7306.

[40] Pierard, O. and Doghri, I., "Study of Various Estimates of the Macroscopic Tangent Operator in the Incremental Homogenization of Elastoplastic Composites," *International Journal for Multiscale Computational Engineering*, Vol. 4, No. 4, 2006, pp. 521–543.

[41] Brassart, L., Doghri, I., and Delannay, L., "Homogenization of elasto-plastic composites coupled with a nonlinear finite element analysis of the equivalent inclusion problem," *International Journal of Solids and Structures*, Vol. 47, No. 5, 2010, pp. 716 – 729.

[42] Kriz, R. and Stinchcomb, W., "Elastic moduli of transversely isotropic graphite fibers and their composites," *Experimental Mechanics*, Vol. 19, No. 2, 1979, pp. 41–49.

[43] Murzewski, J., "Une theorie statistique du corps fargile quasi-homogene," *Proc. IUTAM 9th Congress, Bruxells, V*, 1957, pp. 313–320.

[44] Kachanov, L. M., "Time of the rupture process under creep conditions," *Izv. Akad. Nauk. S.S.R. Otd. Tech. Nauk.*, Vol. 8, 1958, pp. 26–31.

[45] Kachanov, L., *Introduction to continuum damage mechanics*, Mechanics of Elastic Stability, M. Nijhoff, 1986.

[46] Kachanov, L. M., "On a mechanism of delayed fracture," *Vopr. Prochn. Mat. Konstr., Izd. AN SSSR 5*, 1959.

[47] Rabotnov, I., *Creep problems in structural members*, North-Holland series in applied mathematics and mechanics, North-Holland Pub. Co., 1969.

[48] Chaboche, J., "Continuum damage mechanics: Present state and future trends," *Nuclear Engineering and Design*, Vol. 105, No. 1, 1987, pp. 19 – 33.

[49] AMBROZIAK, A. and KŁOSOWSKI, P., "Survey of modern trends in analysis of continuum damage mechanics," *Task Quarterly*, Vol. 10, No. 4, 2006, pp. 437–454.

[50] Fatemi, A. and Yang, L., "Cumulative fatigue damage and life prediction theories: a survey of the state of the art for homogeneous materials," *International Journal of Fatigue*, Vol. 20, No. 1, 1998, pp. 9 – 34.

[51] Zaoui, A., "Continuum Micromechanics: Survey," *Journal of Engineering Mechanics*, Vol. 128, No. 8, 2002, pp. 808–816.

[52] Varna, J., Joffe, R., and Talreja, R., "Mixed Micromechanics and Continuum Damage Mechanics Approach to Transverse Cracking in [S, 90n]s Laminates," *Mechanics of Composite Materials*, Vol. 37, No. 2, 2001, pp. 115–126.

[53] Allen, D. H., "Homogenization principles and their application to continuum damage mechanics," *Composites Science and Technology*, Vol. 61, No. 15, 2001, pp. 2223 – 2230.

[54] Williams, K. V., Vaziri, R., and Poursartip, A., "A physically based continuum damage mechanics model for thin laminated composite structures," *International Journal of Solids and Structures*, Vol. 40, No. 9, 2003, pp. 2267 – 2300.

[55] Zou, Z., Reid, S., and Li, S., "A continuum damage model for delaminations in laminated composites," *Journal of the Mechanics and Physics of Solids*, Vol. 51, No. 2, 2003, pp. 333 – 356.

[56] Nguyen, B. N. and Khaleel, M. A., "A mechanistic approach to damage in short-fiber composites based on micromechanical and continuum damage mechanics descriptions," *Composites Science and Technology*, Vol. 64, No. 5, 2004, pp. 607 – 617.

[57] Raghavan, P. and Ghosh, S., "A continuum damage mechanics model for unidirectional composites undergoing interfacial debonding," *Mechanics of Materials*, Vol. 37, No. 9, 2005, pp. 955 – 979.

[58] Kumar, R. S. and Talreja, R., "A continuum damage model for linear viscoelastic composite materials," *Mechanics of Materials*, Vol. 35, No. 36, 2003, pp. 463 – 480.

[59] Hinton, M., Kaddour, A., and Soden, P., "Chapter 1.1 - The world-wide failure exercise: Its origin, concept and content," *Failure Criteria in Fibre-Reinforced-Polymer Composites*, edited by M. Hinton, A. Kaddour, and P. Soden, Elsevier, Oxford, 2004, pp. 2 – 28.

[60] Greenwood, J. H., "German work on GRP design," *Composites*, 1977, pp. 175 – 184.

[61] Owen, M. and Rice, D., "Biaxial strength behaviour of glass fabric-reinforced polyester resins," *Composites*, Vol. 12, No. 1, 1981, pp. 13 – 25.

[62] Swanson, S. and Christoforou, A., "Progressive failure in carbon/epoxy laminates under biaxial stress," *Journal of engineering materials and technology*, Vol. 109, No. 1, 1987, pp. 12–16.

[63] Soden, P., Hinton, M., and Kaddour, A., "Chapter 2.1 - Lamina properties, lay-up configurations and loading conditions for a range of fibre reinforced composite laminates," *Failure Criteria in Fibre-Reinforced-Polymer Composites*, edited by M. Hinton, A. Kaddour, and P. Soden, Elsevier, Oxford, 2004, pp. 30 – 51.

[64] Soden, P., Hinton, M., and Kaddour, A., "Chapter 2.2 - Biaxial test results for strength and deformation of a range of E-glass and carbon fibre reinforced composite laminates: Failure exercise benchmark data," *Failure Criteria in Fibre-Reinforced-Polymer Composites*, edited by M. Hinton, A. Kaddour, and P. Soden, Elsevier, Oxford, 2004, pp. 52 – 96.

[65] Kaddour, A., Hinton, M., and Soden, P., "Chapter 6.1 - Predictive capabilities of nineteen failure theories and design methodologies for polymer composite laminates. Part B: Comparison with experiments," *Failure Criteria in Fibre-Reinforced-Polymer Composites*, edited by M. Hinton, A. Kaddour, and P. Soden, Elsevier, Oxford, 2004, pp. 1073 – 1221.

[66] Soden, P., Kaddour, A., and Hinton, M., "Chapter 7.1 - Recommendations for designers and researchers resulting from the world-wide failure exercise," *Failure Criteria in Fibre-Reinforced-Polymer Composites*, edited by M. Hinton, A. Kaddour, and P. Soden, Elsevier, Oxford, 2004, pp. 1223 – 1251.

[67] Kaddour, A., Hinton, M., Smith, P., and Li, S., "The background to the third world-wide failure exercise," *Journal of Composite Materials*, Vol. 47, No. 20-21, 2013, pp. 2417–2426.

[68] Elliott, H. A., "An analysis of the conditions for rupture due to griffith cracks," *Proceedings of the Physical Society*, Vol. 59, No. 2, 1947, pp. 208.

[69] Barenblatt, G., "The formation of equilibrium cracks during brittle fracture. General ideas and hypotheses. Axially-symmetric cracks," *Journal of Applied Mathematics and Mechanics*, Vol. 23, No. 3, 1959, pp. 622 – 636.

[70] Barenblatt, G. I., "The mathematical theory of equilibrium cracks in brittle fracture," *Advances in applied mechanics*, Vol. 7, No. 1, 1962, pp. 55–129.

[71] Dugdale, D., "Yielding of steel sheets containing slits," *Journal of the Mechanics and Physics of Solids*, Vol. 8, No. 2, 1960, pp. 100 – 104.

[72] Willis, J., "A comparison of the fracture criteria of griffith and barenblatt," *Journal of the Mechanics and Physics of Solids*, Vol. 15, No. 3, 1967, pp. 151 – 162.

[73] Rice, J. R., "A path independent integral and the approximate analysis of strain concentration by notches and cracks," *Journal of applied mechanics*, Vol. 35, No. 2, 1968, pp. 379–386.

[74] Cribb, J. and Tomkins, B., "On the nature of the stress at the tip of a perfectly brittle crack," *Journal of the Mechanics and Physics of Solids*, Vol. 15, No. 2, 1967, pp. 135 – 140.

[75] Hillerborg, A., Moder, M., and Petersson, P.-E., "Analysis of crack formation and crack growth in concrete by means of fracture mechanics and finite elements," *Cement and Concrete Research*, Vol. 6, No. 6, 1976, pp. 773 – 781.

[76] Zhang, Z. J. and Paulino, G. H., "Cohesive zone modeling of dynamic failure in homogeneous and functionally graded materials," *International Journal of Plasticity*, Vol. 21, No. 6, 2005, pp. 1195–1254.

[77] Hui, C. Y., Ruina, A., Long, R., and Jagota, A., "Cohesive Zone Models and Fracture," *The Journal of Adhesion*, Vol. 87, No. 1, 2011, pp. 1–52.

[78] Paulino, G., Jin, Z., and Dodds Jr, R., "Failure of functionally graded materials," *Comprehensive structural integrity*, Vol. 2, No. 13, 2003, pp. 607–644.

[79] Park, K. and Paulino, G. H., "Cohesive Zone Models: A Critical Review of Traction-Separation Relationships Across Fracture Surfaces," *Applied Mechanics Reviews*, Vol. 64, No. 6, 2011, pp. 061002.

[80] Kulkarni, M. G., Geubelle, P. H., and Matou, K., "Multi-scale modeling of heterogeneous adhesives: Effect of particle decohesion," *Mechanics of Materials*, Vol. 41, No. 5, 2009, pp. 573 – 583.

[81] Scheider, I., "Derivation of separation laws for cohesive models in the course of ductile fracture," *Engineering Fracture Mechanics*, Vol. 76, No. 10, 2009, pp. 1450 – 1459, MatModels 2007.

[82] Kulkarni, M. G., Matou, K., and Geubelle, P. H., "Coupled multi-scale cohesive modeling of failure in heterogeneous adhesives," *International Journal for Numerical Methods in Engineering*, Vol. 84, No. 8, 2010, pp. 916–946.

[83] Zeng, X. and Li, S., "A multiscale cohesive zone model and simulations of fractures," *Computer Methods in Applied Mechanics and Engineering*, Vol. 199, No. 912, 2010, pp. 547 – 556.

[84] Xu, X. P. and Needleman, A., "Void nucleation by inclusion debonding in a crystal matrix," *Modelling and Simulation in Materials Science and Engineering*, Vol. 1, No. 2, 1993, pp. 111.

[85] Needleman, A., "A continuum model for void nucleation by inclusion debonding," *Journal of applied mechanics*, Vol. 54, No. 3, 1987, pp. 525–531.

[86] Rice, J. R., "Dislocation nucleation from a crack tip: an analysis based on the Peierls concept," *Journal of the Mechanics and Physics of Solids*, Vol. 40, No. 2, 1992, pp. 239–271.

[87] Freed, Y. and Banks-Sills, L., "A new cohesive zone model for mixed mode interface fracture in bimaterials," *Engineering Fracture Mechanics*, Vol. 75, 2008, pp. 4583–4593.

[88] Schellekens, J. C. J. and De Borst, R., "On the numerical integration of interface elements," *International Journal for Numerical Methods in Engineering*, Vol. 36, No. 1, 1993, pp. 43–66.

[89] Tomar, V., Zhai, J., and Zhou, M., "Bounds for element size in a variable stiffness cohesive finite element model," *International Journal for Numerical Methods in Engineering*, Vol. 61, No. 11, 2004, pp. 1894–1920.

[90] Turon, A., Dvila, C., Camanho, P., and Costa, J., "An engineering solution for mesh size effects in the simulation of delamination using cohesive zone models," *Engineering Fracture Mechanics*, Vol. 74, No. 10, 2007, pp. 1665 – 1682.

[91] Roy, Y. and Dodds, RobertH., J., "Simulation of ductile crack growth in thin aluminum panels using 3-D surface cohesive elements," *International Journal of Fracture*, Vol. 110, No. 1, 2001, pp. 21–45.

[92] Han, T.-S., Ural, A., Chen, C.-S., Zehnder, A., Ingraffea, A., and Billington, S., "Delamination buckling and propagation analysis of honeycomb panels using a cohesive element approach," *International Journal of Fracture*, Vol. 115, No. 2, 2002, pp. 101–123.

[93] Rots, J. G. and Borst, R. D., "Analysis of concrete fracture in direct tension," *International Journal of Solids and Structures*, Vol. 25, No. 12, 1989, pp. 1381 – 1394.

[94] Crisfield, M., "A fast incremental iterative solution procedure that handles snap through," *Computers and Structures*, Vol. 13, 1981, pp. 55 – 62.

[95] Powell, G. and Simons, J., "Improved iteration strategy for nonlinear structures," *International Journal for Numerical Methods in Engineering*, Vol. 17, No. 10, 1981, pp. 1455–1467.

[96] Song, S. H., Paulino, G. H., and Buttlar, W. G., "A bilinear cohesive zone model tailored for fracture of asphalt concrete considering viscoelastic bulk material," *Engineering Fracture Mechanics*, Vol. 73, No. 18, 2006, pp. 2829 – 2848.

[97] Pipes, R. B. and Pagano, N., "Interlaminar Stresses in Composite Laminates Under Uniform Axial Extension," *Journal of Composite Materials*, Vol. 4, No. 4, 1970, pp. 538–548.

[98] Whitcomb, J. D., Chapman, C. D., and Tang, X., "Derivation of Boundary Conditions for Micromechanics Analyses of Plain and Satin Weave Composites," *Journal of Composite Materials*, Vol. 34, No. 9, Jan. 2000, pp. 724–747.

[99] McLendon, W. R. and Whitcomb, J. D., "Micro-scale Analysis for the Prediction of Strength under Biaxial Thermomechanical Load," *Proceedings of the American Society for Composites*, Arlington, TX, 2012.

[100] Qu, J. and Cherkaoui, M., *Fundamentals of Micromechanics of Solids*, Wiley, Hoboken, New Jersey, 1st ed., 2006.

[101] Huang, C.-Y., Trask, R. S., and Bond, I. P., "Characterization and analysis of carbon fibre-reinforced polymer composite laminates with embedded circular vasculature," *Journal of The Royal Society Interface*, 2010.

[102] Soden, P., Hinton, M., and Kaddour, A., "Lamina properties, lay-up configurations and loading conditions for a range of fibre-reinforced composite laminates," *Composites Science and Technology*, Vol. 58, 1998.

[103] Blackketter, D. M., Walrath, D. E., and Hansen, A. C., "Modeling damage in a plain weave fabric-reinforced composite material," *Journal of composites technology & research*, Vol. 15, No. 2, 1993, pp. 136–142.

[104] Fullwood, D. T., Niezgoda, S. R., and Kalidindi, S. R., "Microstructure reconstructions from 2-point statistics using phase-recovery algorithms," *Acta Materialia*, Vol. 56, No. 5, 2008, pp. 942 – 948.

[105] Tewari, A., Gokhale, A., Spowart, J., and Miracle, D., "Quantitative characterization of spatial clustering in three-dimensional microstructures using two-point correlation functions," *Acta Materialia*, Vol. 52, No. 2, 2004, pp. 307 – 319.

[106] Niezgoda, S., Fullwood, D., and Kalidindi, S., "Delineation of the space of 2-point correlations in a composite material system," *Acta Materialia*, Vol. 56, No. 18, 2008, pp. 5285 – 5292.

[107] Papoulis, A., *Probability, Random Variables, and Stochastic Processes*, McGraw Hill, 1984.

[108] Jumbo, F., Ruiz, P. D., Yu, Y., Swallowe, G. M., Ashcroft, I. A., and Huntley, J. M., "Experimental and Numerical Investigation of Mechanical and Thermal Residual Strains in Adhesively Bonded Joints," *Strain*, Vol. 43, No. 4, 2007, pp. 319–331.

[109] Wu, E. M.-C. and Reuter, Robert Carl, j. a., "Crack extension in fiberglass reinforced plastics / by Edward M. Wu and R. C. Reuter, Jr," 1965, Sponsored by U.S. Bureau of Naval Weapons contract NOw 64-0178-d.

APPENDIX A

PERIODIC BOUNDARY CONDITIONS

This appendix gives details about the periodic boundary conditions used in this study. Because an entire unit cell is being analyzed for both the hexagonal and random fiber arrangements, the explicit periodic boundary conditions for the finite element models are expressed in terms of the displacements on the boundaries. It should be noted that when there are multi-point constraints, if a zero force is assigned to the master degree of freedom, there is an automatic imposition that forces acting on the unit cell being modeled are equilibrated by the forces on adjacent unit cells.

For the hexagonal unit cell, the boundary conditions are

$$\begin{aligned} u_i^{\overline{a}}\left(x_1, x_2+\tfrac{m}{2}, x_3+\tfrac{n}{2}\right) &= u_i^{a}\left(x_1, x_2-\tfrac{m}{2}, x_3-\tfrac{n}{2}\right) + \left\langle \tfrac{\partial u_i}{\partial x_2} \right\rangle m + \left\langle \tfrac{\partial u_i}{\partial x_3} \right\rangle n \\ u_i^{\overline{b}}\left(x_1, x_2+\tfrac{m}{2}, x_3-\tfrac{n}{2}\right) &= u_i^{b}\left(x_1, x_2-\tfrac{m}{2}, x_3+\tfrac{n}{2}\right) + \left\langle \tfrac{\partial u_i}{\partial x_2} \right\rangle m - \left\langle \tfrac{\partial u_i}{\partial x_3} \right\rangle n \\ u_i\left(x_1, \tfrac{d}{2}, x_3\right) &= u_i\left(x_1, -\tfrac{d}{2}, x_3\right) + \left\langle \tfrac{\partial u_i}{\partial x_2} \right\rangle d \\ u_i\left(\tfrac{e}{2}, x_2, x_3\right) &= u_i\left(-\tfrac{e}{2}, x_2, x_3\right) + \left\langle \tfrac{\partial u_i}{\partial x_1} \right\rangle e \end{aligned} \tag{A.1}$$

$$\left\langle \frac{\partial u_i}{\partial x_j} \right\rangle = \left\langle \frac{\partial u_j}{\partial x_i} \right\rangle \tag{A.2}$$

$$u_i^{origin} = 0 \tag{A.3}$$

The coordinate system and the parameters are defined in Figure A.1. Equation (A.1) gives the conditions for periodicity and Equations (A.2) and (A.3) are used to prevent rigid body motion. The loads consist of specified volume average displacement gradients, denoted by $\left\langle \frac{\partial u_i}{\partial x_j} \right\rangle$.

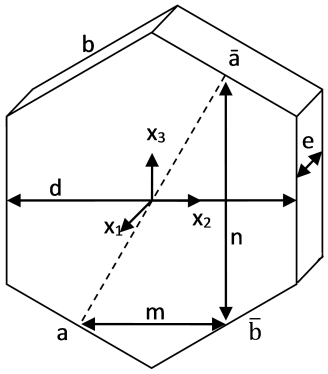

Figure A.1. Unit cell for hexagonal array of fibers

The boundary conditions for the unit cell containing a random array of fibers are quite similar. Since a quasi-3D finite element model was used, the analysis region consists of just a plane, but there are still three displacement fields. Throughout the model the normal strain in the x1 direction is constant, so $\epsilon_{xx} = \left\langle \frac{\partial u_1}{\partial x_1} \right\rangle$. The boundary conditions are

$$\begin{aligned} u_i\left(x_1, \tfrac{d}{2}, x_3\right) &= u_i\left(x_1, -\tfrac{d}{2}, x_3\right) + \left\langle \tfrac{\partial u_i}{\partial x_2} \right\rangle d \\ u_i\left(x_1, x_2, \tfrac{d}{2}\right) &= u_i\left(x_1, x_2, -\tfrac{d}{2}\right) + \left\langle \tfrac{\partial u_i}{\partial x_3} \right\rangle d \end{aligned} \tag{A.4}$$

As before, the loads consist of specified volume average displacement gradients, denoted by $\left\langle \frac{\partial u_i}{\partial x_j} \right\rangle$. Also, Equations (A.2) and (A.3) are used to prevent rigid body motion. Figure A2 defines the parameters in Equation (A.4).

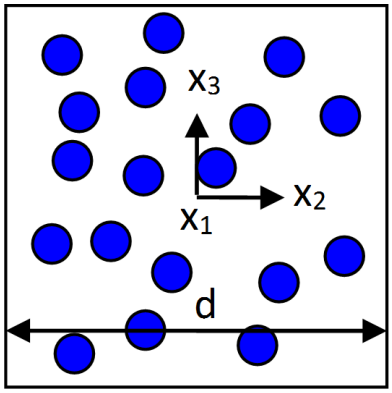

Figure A.2. Square unit cell for random array of fibers